Development of a multimodal nonlinear imaging system for biophotonic applications

by

George Okyere Dwapanyin

Dissertation presented for the degree of Doctorate of Philosophy in the Faculty of Sciences at Stellenbosch University

Supervisors:

Prof. Erich G. Rohwer
Dr. Pieter H. Neethling
Dr. Gurthwin W. Bosman

March 2020

Declaration

By submitting this dissertation electronically, I declare that the entirety of the work contained therein is my own, original work, that I am the sole author thereof (save to the extent explicitly otherwise stated), that reproduction and publication thereof by Stellenbosch University will not infringe any third party rights and that I have not previously in its entirety or in part submitted it for obtaining any qualification.

Date: .....

Abstract

Development of a multimodal nonlinear imaging system for biophotonic applications

G.O. Dwapanyin

Department of Physics,
Stellenbosch University,
Private Bag X1, Matieland 7602,
South Africa.

Dissertation: PhD

March 2020

Multiphoton microscopy techniques have gained wide prominence in biophotonics imaging applications since their inventions. Compared to conventional optical imaging, these nonlinear optical microscopy (NLOM) techniques are intrinsically confocal, and thus enables three-dimensional imaging with submicron spatial resolution. Additional advantages include decreased photodamage to tissue, increased depth of penetration as well as the ability to perform label-free imaging. Signal response in NLOM techniques depend nonlinearly on the peak intensity, therefore requiring a high peak intensity laser as source. Control of ultrashort pulses enables the generation of high peak intensity pulses with lower excitation pulse energies. This dissertation focuses on the development of a nonlinear microscopy system for biological applications based on the control of the spectral phase of broadband supercontinuum pulses generated in a polarization maintaining all normal dispersion photonic crystal fibre. We further demonstrate, for the first time, the real world application of a time domain ptychographic phase measurement technique known as i^{2}PIE which allows for phase correction at the object plane, in microscopy, and how this phase control contributes to image enhancement in two photon excitation fluorescence (TPEF) and second harmonic generation (SHG) imaging of biological tissue. By comparing this new technique to the commonly used multiphoton intrapulse interference phase scan (MIIPS) measurement technique, we show that i^{2}PIE offers an improved spectral phase measurement which can be used to generate shorter temporal pulses and ultimately produce higher peak intensities, even at lower pulse energies. Our results also show that for the same input pulse energies, i^{2}PIE provides a higher contrast image and an improved signal to noise ratio compared to MIIPS. The results ob-

tained from this work projects i^{2}PIE as a promising phase measurement technique for the coherent control of ultrashort pulses used in nonlinear microscopy.

Uittreksel

Ontwikkeling van 'n multimodale nielineêre afbeelding stelsel vir bio-fotoniese toepassings

G.O. Dwapanyin

Fisika Departement,
Stellenbosch Universiteit,
Privaatsak X1, Matieland 7602,
Suid Afrika.

Proefskrif: PhD

Maart 2020

Multi-foton mikroskopie tegnieke het wye aanklank in biofotonika afbeelding toepassings gevind sedert hulle ontwikkeling. Vergeleke met konvensionele optiese afbeelding, is hierdie nielineêre optiese mikroskopie (NLOM) tegnieke intrinsiek konfokaal, en dus laat dit drie dimensionele afbeelding met 'n sub-mikron ruimtelike resolusie toe. Verdere voordele sluit in 'n afname in lig-skade aan weefsel, dieper penetrasie en die moontlikheid om merker vrye afbeelding uit te voer. Die sein sterkte in NLOM tegnieke hang nielineêr af van die piek intensiteit, en gevolglik benodig dit 'n hoë piek intensiteit laser as bron. Beheer oor ultra-kort pulse laat die vorming van hoë intensiteit pulse met laer opwekkings puls energieë toe. Hierdie proefskrif fokus op die ontwikkeling van 'n nielineêre mikroskopie sisteem vir biologiese toepassings gebaseer op die beheer van die spektrale fase van breëband super-kontinuum pulse gegenereer in 'n volkome-normale-dispersie-fotoniese-kristal-vesel wat polarisasie behou. Ons demonstreer verder, vir die eerste keer, die werklike toepassing van 'n tyd-gebiedstigografie fase meet tegniek genaamd i^{2}PIE, wat dit moontlik maak om die fase te korrigeer by die objek vlak in 'n mikroskoop, asook hoe hierdie fase beheer bydrae tot 'n verbetering van die gevormde beeld tydens twee-foton-opwekkings fluoressensie en tweede harmoniek opwekking afbeelding van biologiese weefsel. Deur hierdie tegnieke te vergelyk moet die algemeen gebruikte multi-foton intra-puls interferensie fase skandering (MIIPS) meet tegniek, wys ons dat die i^{2}PIE 'n verbeterde spektrale fase meeting lewer wat gebruik kan word om korter pulse te genereer en gevolglik hoër piek intensiteite, selfs by laer pulse energieë. Ons resultate wys ook dat vir dieselfde inset puls energieë lewer i^{2}PIE 'n hoër kontras beeld en 'n verbeterde sein tot geraas verhouding as MIIPS. Die resultate verkry uit hierdie werk toon i^{2}PIE as

'n belowende fase meet tegniek vir die koherente beheer van ultra-kort pulse wat in nielineêre mikroskopie gebruik word.

Acknowledgements

"I will give thanks to you, Lord, with all my heart; I will tell of all your wonderful deeds."—Psalms 9:1

I would like to express my sincerest gratitude to my excellent team of supervisors: Prof Erich Rohwer, Dr Pieter Neethling and Dr Gurthwin Bosman for the incredible guidance, support and wealth of knowledge imparted to me throughout this period. Without your patience, encouragement and words of motivation, this dissertation would not have seen the light of day.

I again would like to thank Dr Dirk Spangenberg, Dr Wilfrid Ndebeka and Mr Ruan Viljoen for all the assistance in the lab and knowledge shared. I would also like to thank Prof Ben Loos the Department of Physiology for providing the labelled mouse cell lines used in this work. I would not have been able to get here without the assistance of the entire technical and administrative staff of the department. You people made this place feel like home, so I say a big thank you.

I owe a debt of gratitude to my wife, Abigail Afriyie Owusu, for sacrificing family life and allowing me to pursue this study. Honey, I can never quantify my debt of gratitude to you. I say God bless you. To my parents: Dr Alexander Oppong Dwapanyin and madam Regina Nkansah, thank you for supporting me to achieve my academic goals. I hope to continue to make you proud. To madam Doris Konadu, Mr Francis Adjei and Rev. Justice Teye, I say God bless you for all the support and encouragement.

I would also like to express my deepest appreciation to the Stellenbosch Institute for Advanced Study (STIAS) for the financial support provided throughout this study. Finally to all other family and friends who supported, prayed for and wished me well throughout this journey, I am most grateful.

Dedications

This dissertation is dedicated to:

My dearest wife Abigail Afriyie Owusu in appreciation of all the love, sacrifices, motivations and countless prayerful nights she has supported me with throughout this period. She is a true description of Proverbs 31:10-31.

It is also dedicated to my parents: Dr Alexander Oppong Dwapanyin and Madam Regina Nkansah for supporting me throughout my academic journey. Finally to my brother Dickson Dwapanyin, the promise has been fulfilled with years to spare...thank you for everything man.

Contents

List of Figures

List of Tables

Chapter 1

Introduction

Over the last few decades, there has been an upsurge in the number of imaging techniques resulting in the development of better diagnostic tools which probe specimen on a micrometer to nanometer scales. Imaging techniques can be classified into two main categories: radiation and optical. Radiation based methods applied to imaging generally include X-ray [1, 2], magnetic resonance imaging[3] and computed tomography [4]. These methods however emit ionising radiations that offer added health risks and are mostly costly. Optical methods have been proven to provide accurate molecular, cellular and sub-cellular details in real time through non-invasive means while still being relatively economically cost effective. Advances in optical imaging techniques have varied applications in areas such as medicine [5, 6], pharmacy [7, 8] and even in arts and archaeology [9].

This chapter presents a general overview of the concepts of optical microscopy with emphasis on nonlinear optical microscopy relevant to the work presented in this dissertation. It presents and discusses the different imaging modalities and the merits of each technique.

1.1 Single and multiphoton microscopy

Since the invention of the laser by Maiman [10], its applications in microscopy and spectroscopy has seen tremendous improvements over the years. The basic principle of laser based technique involves the excitation of molecules from the ground state to some excited state through the absorption or scattering of photons of energy $\hbar\omega$ where $\hbar$ is the Planck's constant$/2\pi$ and ω is the angular frequency of the incident photon. Depending on the number of photons involved in the excitation, the process is either a linear (single photon) or nonlinear (multiphoton). The common procedures under each process will now be considered in brief details.

1.2 Linear microscopy

This is the conventional microscopy where excitation involves the absorption of a single photon. It consists of traditional widefield imaging [11, 12] where image contrast is based on linear processes such as absorption, scattering, reflection and fluorescence.

For example, in conventional fluorescence microscopy, it is found that there exists a linear relationship between the emitted fluorescence intensity and the incident intensity. Furthermore, its excitation requires high energy photons and as such employs excitation with short wavelength lasers (or mercury and deuterium lamps as well as tungsten halogen lamps) mostly operating in the visible or ultraviolet (UV) region of the electromagnetic spectrum [13]. Figure 1.1 shows a typical Jablonski diagram for a linear process. The absorption of the incident photon of energy $\hbar\omega_i$ by molecules in

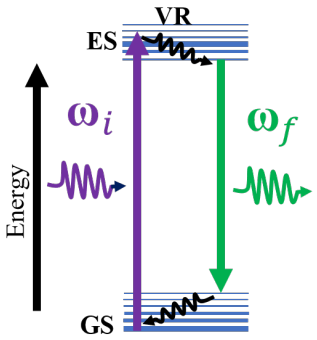

Figure 1.1: Jablonski energy level diagram for linear (1-photon) optical process showing excitation by absorption of the photon of energy $\hbar\omega_i$ and radiative emission of energy $\hbar\omega_f$ after non-radiative vibrational relaxation (VR). GS and ES represent the electronic ground and excited states respectively. Excitation starts from the ground state (GS) with the absorption of photons of angular frequency ω_i. Non radiative decay resulting from vibrational relaxation (VR) of energy is represented by black wavy arrows. Radiative emissions by way of fluorescence is represented by ω_f.

the lowest vibrational state of the electronic ground state (GS) causes an excitation to vibrational states in a higher electronic state (ES). Due to Kasha's rule [14], which states that radiative decay can only occur from the lowest excited state for a given multiplicity, the excited molecules undergo non-radiative decay through vibrational relaxation (VR) and internal conversion to the lowest level of the first excited state (ES_1) before undergoing radiative fluorescence to the ground state typically on a nanosecond time scale [15] with the emission of a photon of energy $\hbar\omega_f$. Due to the energy lost in the non-radiative decay, the emitted photon has less energy than the absorbed photon (i.e. $\omega_f < \omega_i$). This implies the emitted photon undergoes a Stokes shift (wavelength shifted towards the red end of the visible spectrum). The fluorescence response depends on the intensity (I) at the focus of the laser beam such that for a continuous wave laser,

$$I = \frac{P}{A} \tag{1.2.1}$$

where P is the average power, A is the area of the focus spot.

Linear microscopy is however prone to poor contrast and image degradation due to unwanted scattering light reaching the detector which also limits its application to shallow depths [12]. To circumvent this drawback, confocal microscopy [16, 17]

was developed by Minsky [18] which introduced the concept of point-by-point illumination as well as the use of excitation and detection pinholes. These adjustments ensured rejection of unwanted scattering as well as out of focus rays leaving only relevant light to reach the detector.

Compared to standard light microscopes, confocal microscopy offers enhanced lateral and axial resolutions thus allowing for observation of fine details [16]. The rejection of light from out of focus regions is as a result of axial resolution enhancement. The main advantage of confocal microscopy, however, is its ability to optically section thick samples [17]. However, despite the increased resolution that confocal geometry presents into single-photon fluorescence microscopy, the use of high energy excitation pulse present the risk of non-negligible photodamage and photobleaching which occurs within the entire illumination cone of the light as well as within the focal volume [17, 19, 20].

1.3 Multiphoton microscopy

This is the microscopy technique based on the excitation of a molecule to an excited state by the simultaneous absorption of two or more photons. Two photon absorption was predicted in 1931 by Maria Göppert-Mayer [21] (translated into English in [22]) but it was not observed until Franken demonstrated it in his work in 1961 with his paper on generation of optical harmonics [23]. In comparison to single-photon microscopy, multiphoton microscopy (MPM) offers a higher degree of sensitivity, deeper penetration into scattering tissue as a result of the near infrared (NIR) excitation wavelength used [24]. It also offers less photodamage and photobleaching due to the smaller excitation volume [25], 3 dimensional imaging as a result of optical sectioning, excitation of UV-absorbing dyes, better signal-to-noise ratio, decreased out-of-focus background [19, 26, 27]. The multiple excitation photons involved are lower in energy (typically in the near infrared) compared to that of single-photon excitation and the excitation is through intermediate states.

The most common multiphoton microscopy techniques involve excitation by simultaneous absorption of either two or three photons as ionization optical breakdown is known to occur when four or more photons are involved [28]. Let us briefly look at the features of these common multiphoton processes.

1.3.1 Two-photon microscopy

In two-photon microscopy (TPM), the excitation rate is proportional to the average squared photon density [17] as a result of the need for simultaneous absorption of two photons per excitation in order to produce a response in the medium. It is therefore a three wave mixing process. In TPM, continuous wave lasers are replaced with high intensity pulsed lasers. For pulsed lasers, the energy per pulse (E) is given by the ratio of the average power (P) to the pulse repetition rate (f) (i.e. $E = \frac{P}{f}$).

For two-photon absorption, the intensity of the material response (I_{TPM}) is proportional to the square of the applied laser intensity (I_i) ie $I_{TPM} \propto I_i^2$. This quadratic dependence of the response on the applied field provides a nonlinear relationship

between incident and emitted field which is why multiphoton microscopy is often referred to as nonlinear microscopy. Thus subsequent reference to nonlinear microscopy implies reference to a multiphoton microscopy and may be used interchangeably.

1.3.1.1 Two-photon excitation fluorescence

The most common TPM technique is the two photon excitation fluorescence (TPEF) microscopy. Figure 1.2 shows the energy level diagram involved in a TPEF process where two NIR pulses excite fluorescence molecules to generate a fluorescence response. Absorption involves real transitions to an excited electronic state with relaxation process governed by the same principles as in one photon absorption.

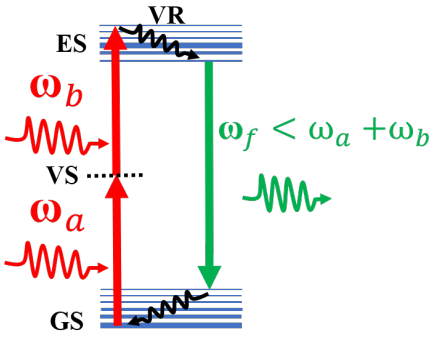

Figure 1.2: Jablonski energy level diagram for two photon excitation fluorescence. The electronic excited state (ES) and surrounding vibrational states are represented by the thick and thin solid lines while virtual state (VS) is depicted with a dash line. All processes start from the ground state (GS) with the absorption of photons of frequencies ω_a and ω_b. Non radiative decay resulting from vibrational relaxation (VR) of energy is represented by black wavy arrows. Radiative emission by way of fluorescence is represented by ω_f.

Though two photons with angular frequencies ω_a and ω_b are simultaneously absorbed, the energy of the fluorescence is less than the total absorption energy i.e. $\omega_f < \omega_a + \omega_b$ and is thus Stokes shifted. TPEF has been applied in many fields of research such a cancer studies, biomedical, cell biology etc [15, 29–31] and has been used to image intrinsic fluorescent biomolecules such as nicotinamide adenine dinucleotide (NADH), flavin adenine dinucleotide (FAD), elastin, Keratin, deoxyribonucleic acid (DNA) [29, 30, 32].

1.3.1.2 Second harmonic generation

Another two photon microscopy process that is often used is second harmonic generation (SHG) whose energy diagram is shown in figure 1.3. Excitation occurs to a quasi-electronic state often referred to as a virtual state (VS). A virtual state is one in which the molecule possesses a very short mean life time and hence there is a large uncertainty in energy. For SHG, $\omega_a = \omega_b = \omega_i$ and there is no dependence on absorption of photons but rather involves a scattering process with SHG occurring on a femtosecond (10^{-15} s) time scale [15]. Second harmonic generation only occurs

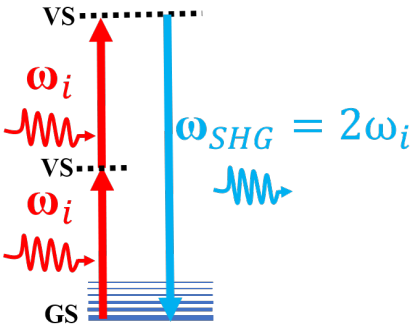

Figure 1.3: Jablonski energy level diagram for second harmonic generation. For second harmonic generation, $\omega_a = \omega_b = \omega_i$. Virtual states (VS) are depicted with dash lines. Second harmonic generation emission is represented by $\omega_{SHG} = 2\omega_i$.

in materials that lack inversion centre (non centrosymmetric materials) and highly ordered media [31] such as collagen fibrils [33], muscles tissue [34] and other biological applications [35]. The energy of the SHG emission is exactly twice the excitation energy ie $2\omega_i = \omega_{SHG}$ and thus the energy of the system is conserved. The emitted response is therefore at exactly half the excitation wavelength and therefore anti-Stokes shifted. Aside from the fact that there should be lack of inversion symmetry for SHG to occur, there is the need for phase matching conditions between the input optical field and the induced dipoles in the material.

Table 1.1: Characteristic features of two photon microscopy techniques

Feature	TPEF	SHG	Ref
Transition involved	Real	Virtual	[15]
Energy of process	Not conserved	Conserved	[15]
Response time	Nanosecond	Femtosecond	[15]
Fluorescence λ	$\lambda_{fluo} > \lambda_i/2$	$\lambda_{SHG} = \lambda_i/2$	
Advantage	Deeper imaging with less phototoxicity; Spatial localization for fluorescence excitation	Coherent process, symmetry selection; No absorption of light; Probing well ordered structure functions of membranes, non-fluorescing tissues	[27]
Contrast mechanics	Electronic levels of the molecules	Nonlinear properties of the medium	[27]
Information	Autofluorescence of some biological substance (Keratin, Myosin etc)	Noncentrocymmetric molecules with spatial organization (collagen, cellulose, elastin etc)	[27, 35]

Table 1.1 summarizes some of the characteristic features of SHG in comparison to TPEF. Due to difference in contrast mechanism and the information that TPEF and SHG provide, they can be integrated into a single setup for simultaneous detection [15, 27, 34, 35]. The system developed as part of this dissertation will focus on applications of two photon excitation fluorescence and second harmonic generation microscopy.

The next section provides a brief overview of three photon microscopy processes although these techniques were not the focus of this work and will neither be applied nor discussed any further in any other section of this work.

1.3.2 Three photon microscopy

This is microscopy based on the four wave mixing process where three photons are simultaneously involved in the excitation process to produce a signal response. The intensity, I_{3PM}, of the response has a cubic dependency on the incident average power i.e $I_{3PM} \propto I_i^3$.

1.3.2.1 Three-photon excitation fluorescence

Three photon fluorescence (3PF) (shown in figure 1.4) occurs in the same manner as TPEF but with three photons absorbed. In practice, excitations are carried out in the short-wavelength infrared (1300 -1700 nm) [36].

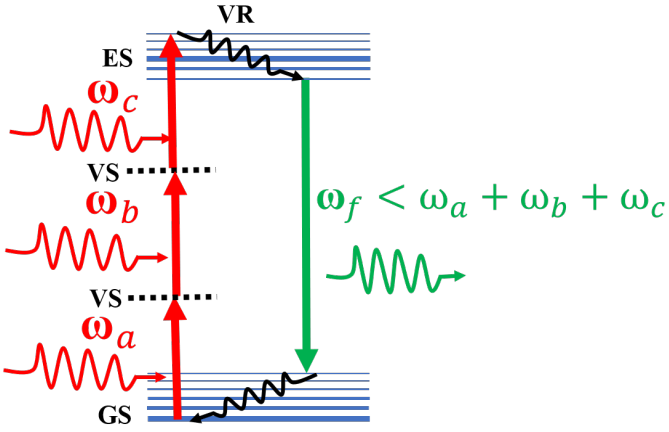

Figure 1.4: Energy level diagrams for three photon fluorescence with absorption of photons with angular frequencies ω_a, ω_b and ω_c to produce a fluorescence response with angular frequency ω_f.

Absorption is to a real state energy level through two transient virtual states. The emitted fluorescence energy is less than the sum of the three excitation photon energies i.e. $\omega_f < \omega_a + \omega_b + \omega_c$. The longer excitation wavelength used results in less tissue scattering thus enabling deeper penetration and the cubic response causes a reduction of out-of-focus excitations. Compared to TPEF, 3PF has a smaller excitation volume which results in lesser photodamage than in TPEF.

3PF is however accompanied with increased absorption at longer wavelengths and higher peak power optical pulses than is required in TPM in order to achieve deep tissue imaging [36, 37]. There is a smaller production of fluorescence flux and hence lower signal and slower imaging in the use of 3PF as a result of its reliance on a lower excitation repetition rate and hence sometimes viewed as complementary to TPM [36].

1.3.2.2 Third harmonic generation

The instantaneous emission of a single photon of angular frequency ω_{THG} after conversion of three incident photons of identical angular frequency ω_i results in third harmonic generation such that $\omega_{THG} = 3\omega_i$ as shown in figure 1.5. It is more ver-

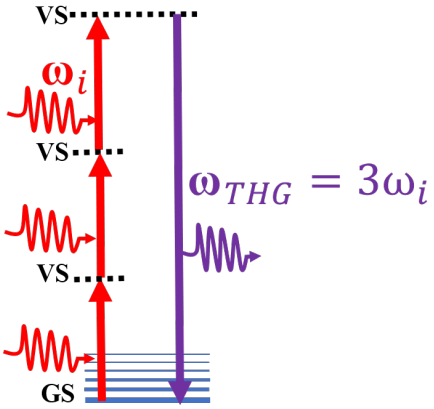

Figure 1.5: Energy level diagram for third harmonic generation with all incident photons having an angular frequency of ω_i and signal response at $3\omega_i$.

satile in comparison with SHG as it is not dependent on specific asymmetry of the structure to be imaged [38]. It is interface-sensitive as the magnitude of the signal scales with the differences between the third order nonlinear susceptibility between the two surfaces [39] and can therefore be used as a general purpose imaging technique to map exact location of cellular membranes. It acts as a non-invasive tool due to the prevention of the release of any excess energy in bio-tissues as a result of the virtual-transition characteristics [40]. However, in homogeneous media, there is a destructive interference in the THG before and after the focal plane due to Gouy phase hence the absence of THG in homogeneous media [39].

Tissue structures commonly imaged with THG are well tabulated by Weigelin et al [38]. Saytashev et al applied THG in the study of red blood cells [41] while Chu et al [40] applied it in the imaging of nuclear plasma membranes.

1.3.2.3 Coherent anti-Stokes Raman scattering

Coherent anti-Stokes Raman scattering (CARS) microscopy is a four-wave mixing imaging technique in which two pump fields with angular frequency ω_p and a Stokes field with angular frequency ω_s interact to generate an anti-Stokes signal with an

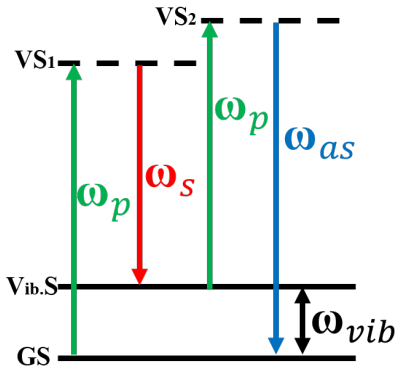

Figure 1.6: Energy level diagram representing coherent anti-Stokes Raman scattering (CARS) process with pump frequency ω_p and Stokes frequency ω_s generating an anti-Stokes signal with frequency $\omega_{as} = 2\omega_p - \omega_s$. ω_{vib} represents the resonance vibrational frequency.

angular frequency ω_{as}. From figure 1.6, the first pump field is responsible for creating oscillations in the medium and corresponds to Rayleigh scattering in the linear regime [42]. The pump and Stokes fields interact in a medium to polarize the medium. A second pump photon scatters off this polarized medium to generate an anti-Stokes field. The interactions between the pump and Stokes fields is coherent and the generated anti-Stokes field has an angular frequency, $\omega_{as} = 2\omega_p - \omega_s$. Vibrational contrast is produced when $\omega_p - \omega_s$ is tuned to be in resonance with a molecular vibration ω_{vib} [43].

CARS mostly requires the alignment of two laser beams in order to generate the pump and Stokes fields. Single beam CARS is now possible thus simplifying the setup conditions [44–46]. The anti-Stokes field generated is highly directional and of higher energy than single-photon fluorescence therefore detection in the presence of strong fluorescence background is possible. Furthermore, deep tissue penetration is possible due to reduced scattering of the NIR excitation beams. The low absorption of the NIR beams leads to a significant reduction in photodamage in biological tissue. 3D resolution is also possible and there is no need for labelling as chemical selectively is provided by the Raman resonance enhancements [42, 43, 47]. However, a strong, non-resonant background from the electronic response of the molecules often dominates the resonant anti-Stokes signal which limits the sensitivity of CARS in detecting weak Raman bands [47, 48].

Other common multiphoton imaging techniques include stimulated Raman scattering (SRS) which is mostly used in imaging contrasts in chemical bonds with high speed, specificity, resolution and sensitivity [49] and four wave mixing (FWM) microscopy which is a branch of CARS which depends on the non-resonant contributions rather than the resonant part in the case of CARS [50].

One can observe that irrespective of the technique used, there are common advantages in the use of nonlinear imaging over conventional imaging techniques. These include: reduced photodamage and photobleaching due to the small focal volume; higher excitation efficiency, possibility for selective imaging with deeper penetration

depths; higher contrast and signal-to-noise ratios (SNR) as well as label free imaging thus eliminating the need for exogenous fluorophores which have the tendency to alter the physiology of living organisms. The next section briefly discusses contrast and signal-to-noise ratio (SNR).

1.4 Signal enhancement techniques

The efficiency of an imaging system is primarily governed by two factors: the spatial resolution and contrast of the system.

1.4.1 Spatial resolution

Spatial resolution in microscopy is the ability of the system to distinguish between the finest details of the sample under investigation. It can be viewed in terms of the system's ability to distinctively separate between two point objects or how the image of a point object spreads in the detection/image plane. Resolution in microscopy was introduced by Abbe [51] although its application in spectroscopy by Rayleigh [52] is commonly mentioned due to the so called Rayleigh criterion which suggests that two components with equal intensity are considered resolved if the highest intensity of one coincides with the first minimum of the other. For any optical imaging system, there are two forms of resolution. The lateral resolution provides an estimation of the quality of the 2D image of the sample in the (x,y) image plane. For a 3D image, the resolution along the optical axis is what is referred to as the axial resolution. For a high numerical aperture (NA) objective, the coordinates in the focal field is given by [53]:

$$v = \frac{2\pi r n}{\lambda}\sin(\theta) \tag{1.4.1a}$$

$$u = \frac{2\pi z n}{\lambda}\sin^2(\theta) \tag{1.4.1b}$$

with θ being the half-angle of the cone of light collected by the lens, n being the refractive index and r and z being the radial and axial coordinates respectively. At the focal point, the intensity distribution orthogonal to the optical axis is given by:

$$I(0, v) \propto \left|\frac{2J_1(v)}{v}\right|^2 \tag{1.4.2}$$

where $J_1(v)$ is the first-order Bessel function of the first kind. Along the optical axis, the intensity distribution is also given by:

$$I(u, 0) \propto (\mathrm{sinc}(u/4))^2 \tag{1.4.3}$$

Taking the first nodes in the lateral and axial distributions to be $v_0 = 1.22\pi$ and $u_0 = 4\pi$ [53], the lateral resolution (r) and axial resolution (z) can be written as:

$$r = \frac{0.61\lambda}{\mathrm{NA}} \tag{1.4.4a}$$

$$z = \frac{2n\lambda}{(\mathrm{NA})^2} \tag{1.4.4b}$$

with NA=$n$sin(θ). For high NA objectives, the diffraction limit and optical resolution based on the Rayleigh criterion is estimated by the FWHM of the focal spot of the laser beam, as calculated by the expressions in equation 1.4.4.

In nonlinear imaging involving nonlinear processes of n^{th} order, the interaction volume has been shown to decrease by a factor of $\sqrt{n}$ compared to the linear interaction volume [53–55]. For example, for second order nonlinear microscopy, possible expressions for calculating the lateral resolution include [55]:

$$r = \frac{0.61\lambda}{1.31\text{NA}} \tag{1.4.5}$$

based on considering resolution of 2-point separations and

$$r = \frac{0.5\lambda}{\sqrt{2}\text{NA}} \tag{1.4.6}$$

based on the estimation of the FWHM of the intensity distribution profile.

Therefore in nonlinear imaging, the three dimensional interaction volume at the focus of the microscope objective depends on the excitation wavelength (λ), numerical aperture (NA) as well as the order of the nonlinear process under implementation. In confocal microscopy, this effective interaction volume is decreased by the use of pinholes in order to collect light only from the small focal volume. In nonlinear microscopy however, the size of the effective excitation area where absorption occurs eliminates the need for pinholes.

1.4.2 Contrast enhancement

Differences in colour and/or intensity generates contrast in imaging and defines the boundary between the invisible and visible features of an image. Contrast can therefore be defined as a measure of the relative luminous difference between the features of interest and the adjacent background. Contrast mechanism in label-free imaging depends on the molecular response to the intensity of the incident electric field. A higher contrast therefore signifies a higher response relative to the background. There are many expressions for determining contrast based on the information required. Common contrast expressions include [56]:

$$\text{Weber Contrast} \qquad \frac{\text{L}_{\text{max}}\text{-L}_{\text{min}}}{\text{L}_{\text{background}}} \tag{1.4.7a}$$

$$\text{Michelson contrast} \qquad \frac{\text{L}_{\text{max}}\text{-L}_{\text{min}}}{\text{L}_{\text{max}}+\text{L}_{\text{min}}} \tag{1.4.7b}$$

$$\text{Root mean square contrast} \qquad \frac{\text{L}_{\sigma}}{\text{L}_{\mu}} \tag{1.4.7c}$$

where L_{max}, L_{min}, $\text{L}_{\text{background}}$, L_{σ} and L_{μ} are the luminance maximum, minimum, background, mean and standard deviations respectively.

For any multiphoton process, the n-photon signal response is proportional to the rate of absorption. This n-photon absorption rate is given by [57]

$$R_{ab}^{(n)} = \frac{\sigma_n}{E^n} f \int_0^{\frac{1}{f}} I^n(t)dt \tag{1.4.8}$$

with $R_{ab}^{(n)}$ being the n-photon absorption rate, σ_n being the n$^{\text{th}}$ absorption cross-section, E is the pulse energy, f is the pulse repetition rate and $I(t)$ is the time dependent intensity of the excitation laser. For a Gaussian shaped pulse, equation 1.4.8 reduces to:

$$R_{ab}^{(n)} = R_o \times I_p^{(n)} \times \tau_p = R_o \times \frac{E_p^n}{\tau_p^n} \times \tau_p = R_o \times \frac{E_p^n}{\tau_p^{n-1}} \tag{1.4.9}$$

where R_o represent the constant term and I_p represents pulse peak intensity for a pulse of energy E_p having a full width half maximum duration of τ_p. The signal response is therefore given by:

$$\begin{aligned} S_p^{(n)} &\propto \frac{E_p^n}{\tau_p^{n-1}} \\ &\propto \frac{P^n}{\tau_p^{n-1} f^n} (\text{for pulsed lasers.}) \end{aligned} \tag{1.4.10}$$

The signal response for n-photon absorption process is therefore proportional to the n$^{\text{th}}$ order of the average power of the excitation light and inversely proportional to the (n-1) order of the pulse duration. For example, for two photon absorption processes,

$$S_p^{(2)} \propto \frac{P^2}{\tau_p \times f^2} \tag{1.4.11}$$

From equation 1.4.10, an increase in nonlinear signal response is observed at either high excitation average powers or shorter pulse durations. Higher average powers and its associated higher pulse energies however increases the risk of photodamage thus making the reduction of pulse durations the best option for generating higher contrast signals. This has led to an increase in the use of ultrashort lasers which typically have a temporal width ranging from picoseconds to femtoseconds. Ultrashort pulses will be discussed later on in section 2.2 of the next chapter.

1.4.2.1 Control of pulse lasers

Ultrashort pulsed lasers with pulse duration below 100 fs are now commercially available. However, pulses with durations much shorter than 50 fs can be generated via control of the pulse. Control of ultrashort pulses provides a means of engineering light-matter interactions in order to enhance the contrast as well as provide selective information extraction and detection. Nonlinear responses are affected by the "shape" of the pulses which is a representation of the spectral amplitude and phase of the electric field in the frequency domain. The pulse profile can also be represented in the time domain through a Fourier transformation. Control of ultrashort pulses in the frequency domain can produce a corresponding control in the temporal domain. Control in the frequency domain is more feasible due to limitations in ultrafast devices to control directly in the temporal domain. Spectral control of optical pulses is achievable through the use of dispersive optics and spatial light modulators in order to generate transform limited pulses.

The nonlinear response generated in multiphoton microscopy is as a result of the high peak powers in the focus of the microscope objective. It is the purpose of

every multiphoton microscopy system to provide as much information as possible. This may require the use of multiple excitation wavelengths and spectral selections. Considering the cost and complexities in the use of multiple mode-locked lasers, the use of a single broadband tunable light source known as a supercontinuum source [58] provides a cheaper and simpler alternative to generate multiphoton excitation wavelengths. Supercontinuum (SC) sources are generated by pumping special types of fibres known as photonic crystal fibres (PCF) with ultrashort laser pulses and have been applied extensively in microscopy and other biophotonic applications [47, 59–61]. Supercontinuum generation and PCFs will be discussed into further details in sections 2.3 and 2.4 of the next chapter. Apart from providing a broad spectral range, SC also provides spatially coherent radiation of which the profile can be controlled to provide ultrashort pulses with pico- and femto-second durations.

The most commonly used pulse control method applied in nonlinear microscopy is the pulse shaper assisted multiphoton intrapulse interference phase scan (MIIPS) technique [62–64] which has been used extensively in multiphoton microscopy [41, 59, 65, 66]. MIIPS will be discussed later in section 2.5.1.3 of the next chapter. It simply measures the spectral phase of the ultrashort pulse and generates a potentially transform limited pulse by applying a negative value of the measured phase to the pulse.

The major limitations of MIIPS include its consideration for only the second-order correction to the phase and neglect of higher order dispersions although it introduces phase distortions of any order [67, 68]. Again, self phase modulation gives rise to fast oscillations in the group delay dispersion (GDD) which are difficult to compensate. The accuracy of MIIPS in compensating such fast oscillating GDD is limited because MIIPS is performed using a slow modulation and can therefore not account for such fast oscillations [68]. One of the goals of this dissertation is to present an alternate and novel technique to overcome these challenges in MIIPS. This novel technique, which will be discussed in detail in section 2.5.1.4 of the next chapter, is based on time domain ptychography [69, 70] which was recently developed in our laboratory.

1.5 Scope of the dissertation

The aim of this dissertation is to design and construct a versatile nonlinear microscopy setup that will be based on the use of broadband supercontinuum pulses. The constructed system will be used to investigate the application of the novel time domain ptychographic phase measurement technique that can be used for pulse compression and its applicability in SHG and TPEF microscopy. Comparative analyses of the features will be investigated alongside the use of pulses compressed with other phase measurement techniques especially the commonly used MIIPS compression technique.

The organisation of the dissertation is as follows: This chapter has briefly introduced the concept of multiphoton optical microscopy and the key features of common two- and three- photon absorption processes applied to optical microscopy and spectroscopy. Signal enhancement techniques have also been presented and brief

concept of coherent control of ultrashort pulses have also been given.

Chapter 2 presents the theoretical framework of the concepts governing the various aspects of the project. The concepts of nonlinear optics, supercontinuum generation as well as the phase measurement techniques which will be used in pulse compression in this dissertation will be discussed. The system design, setup, calibration and characterization procedures will be presented and discussed in chapter 3.

Chapter 4 presents and discusses the characteristic features of the experimental polarization maintaining fibre and the novel time domain ptychographic phase measurement technique. Comparative studies of the results obtained from i^2PIE phase measurement technique will be made with phase distortions measured with MIIPS. Results generated after applying these measured phases to compress the pulse will be analysed alongside supercontinuum pulses compressed with only chirped mirrors and non-SC pulses.

Applications of the different technique-based compressed pulses to contrast and signal-to-noise ratio enhancement in biophotonic applications will be presented and discussed in chapter 5. The applications will be restricted to two-photon absorption processes only specifically to two photon excitation fluorescence and second harmonic generation microscopy. Endogenous and exogenous fluorescence as well as SHG in both plant and mammalian tissues will be investigated.

The last and final 6th chapter will conclude the dissertation and provide future outlooks for the project.

Chapter 2

Theoretical background

In this chapter, the theories governing various sections of the imaging system will be introduced. An introductory concept of nonlinear optics and nonlinear processes specifically second harmonic generation (SHG) and two photon excitation fluorescence (TPEF), ultrashort pulse generation and characteristics will be considered. The concept of supercontinuum generation, the principles governing the different phase measurement techniques as well as temporal pulse compression will also be discussed.

2.1 Introduction to nonlinear optics

Nonlinear optics can be described as the study of the interaction of intense laser light with matter. It involves phenomena (SHG, TPEF etc.) that makes an appearance in the presence of high intensity light interacting with matter. The nonlinear interaction of high intensity light in a medium is understood to be as a result of the dielectric polarization responding nonlinearly with the incident electric field of the light. To demonstrate the appearance of the nonlinear phenomena, consider the Maxwell's equations:

$$\text{Ampere's Law} \qquad \nabla \times \vec{H} = \vec{J} + \frac{\partial \vec{D}}{\partial t} \tag{2.1.1a}$$

$$\text{Faraday's Law} \qquad \nabla \times \vec{E} = -\frac{\partial \vec{B}}{\partial t} \tag{2.1.1b}$$

$$\text{Gauss' Law for magnetic field} \qquad \nabla \cdot \vec{B} = 0 \tag{2.1.1c}$$

$$\text{Gauss' Law for electric field} \qquad \nabla \cdot \vec{D} = \rho \tag{2.1.1d}$$

where $\vec{E}$ is the electric field in space and time $(\vec{r}, t)$, $\vec{H}$ is the magnetic field, $\vec{B}$, $\vec{D}$ and $\vec{J}$ being the magnetic flux, electric displacement field and current density respectively and ρ is the charge density. The electric displacement, $\vec{D}$ is related to the induced polarization $\vec{P}$ by

$$\vec{D} = \varepsilon \vec{E} + \vec{P} \tag{2.1.2}$$

where the polarization is the sum of all dipole moments in a volume given by $\vec{P} = \mathrm{N}\vec{p}$ with N being the number of dipoles per unit volume and $\vec{p}$ being the average dipole

moment of the individual dipoles in the medium. In linear optics, the induced polarization depends linearly on the electric field (applying Einstein's summation principle),

$$P_i = \varepsilon_0 \chi_{ij}^{(1)} E_j \tag{2.1.3}$$

where i (or j) = x,y,z coordinates with $\chi^{(1)}$ being the proportionality constant known as the linear susceptibility of the medium and ε_0 is the permittivity of free space. The susceptibility, χ is a property of the material and mediates the response to the electric field and manifests in the polarization. Generally, the induced polarization is expanded as a power series of the electric field $\vec{E}$ (again applying Einstein's summation principle).

$$P_i = \varepsilon_0[\chi_{ij}^{(1)} E_j + \chi_{ijk}^{(2)} E_j E_k + \chi_{ijkl}^{(3)} E_j E_k E_l + ...] \tag{2.1.4}$$

where i (or j) = x,y,z coordinates with $\chi^{(2)}$ and $\chi^{(3)}$ denoting the second and third order nonlinear optical susceptibility tensors respectively. Equation 2.1.4 can be decomposed into linear and nonlinear polarization component as $\vec{P} = \vec{P}_L + \vec{P}_{NL}$. Combining equations 2.1.1 and 2.1.2 and the relation $\vec{B} = \mu_0 \vec{H}$ gives the general wave equation

$$\nabla \times \nabla \times \vec{E} + \frac{1}{c^2}\frac{\partial^2 \vec{E}}{\partial t^2} = -\frac{1}{\varepsilon_0 c^2}\frac{\partial^2 \vec{P}}{\partial t^2} \tag{2.1.5}$$

For a dielectric medium, the approximation $\nabla \times \nabla \times \vec{E} = \nabla(\nabla \cdot \vec{E}) - \nabla^2 \vec{E} \approx -\nabla^2 \vec{E}$ since $\nabla \cdot \vec{E} = 0$ as a result of the absence of free charges in the medium. This reduces equation 2.1.5 to:

$$\nabla^2 \vec{E} - \frac{1}{c^2}\frac{\partial^2 \vec{E}}{\partial t^2} = \frac{1}{\varepsilon_0 c^2}\frac{\partial^2 \vec{P}}{\partial t^2} \tag{2.1.6}$$

Equation 2.1.6 can be converted into the frequency domain through Fourier transform as $\partial t \rightarrow -i\omega$ giving:

$$\nabla^2 \tilde{E} + \frac{\omega^2}{c^2}\tilde{E} = -\frac{\omega^2}{\varepsilon_0 c^2}\tilde{P} \tag{2.1.7}$$

where $\tilde{E}$ and $\tilde{P}$ represent the electric field and polarization in frequency domain respectively. This implies

$$\nabla^2 \tilde{E} + \frac{\omega^2}{c^2}\tilde{E} = -\frac{\omega^2}{\varepsilon_0 c^2}(\tilde{P}_L + \tilde{P}_{NL}) \tag{2.1.8}$$

Given that $\chi^{(1)} = n^2 - 1$ and $n = \sqrt{\varepsilon}$, where ε is the permittivity of the medium, equation 2.1.8 can be simplified into the wave equation in nonlinear optical medium as

$$\nabla^2 \tilde{E} + k^2(\omega)\tilde{E} = -\frac{\omega^2}{\varepsilon_0 c^2}\tilde{P}_{NL} \tag{2.1.9}$$

where k is the wavenumber.

We will now briefly discuss a few of the orders of nonlinear processes contributing to the polarization.

2.1.1 Linear processes

This is the conventional optics where the induced polarization responds linearly on the electric field as shown in equation 2.1.3. Linear processes dominate at low intensities and account for common effects such as reflection, refraction and diffraction. It accounts for optical processes such as linear (one photon) absorption (1PA) for excitation wavelengths within the absorption range of a target sample. The photoenergy deposited into the target sample as a results of 1PA, can be dissipated through radiative (fluorescence and phosphorescence) and non-radiative processes [71, 72]. Repeated 1PA and energy dissipation can eventually cause irrevocable damage to a sample [20].

2.1.2 Second order nonlinear processes

Second order processes involve the polarization responding quadratically to the applied electric field such that $\tilde{P}_i^{(2)} = \varepsilon_0 \chi_{ijk}^{(2)} \tilde{E}_j \tilde{E}_k$ where $\chi_{ijk}^{(2)}$ is the second order susceptibility tensor. For non-centrosymmetric materials this second order nonlinear polarization provides a mechanism for three wave mixing processes [73, 74]. Considering an electric field

$$E_i(z,t) = A_i(z) e^{\mathrm{i}(k_i z - \omega_i t)} + cc \tag{2.1.10}$$

where $A_\mathrm{i}(z)$ and ω_i are the amplitude and angular frequency respectively for each polarization direction $i\epsilon\{x,y,z\}$, the second order NL polarization is given by

$$\begin{aligned} P_i^{(2)} =& \varepsilon_0 \chi_{ijk}^{(2)} E_j(z,t) E_k(z,t) \\ =& \varepsilon_0 \chi_{ijk}^{(2)} (A_\mathrm{j}(z) e^{\mathrm{i}(k_j z - \omega_j t)} + cc)(A_\mathrm{k}(z) e^{\mathrm{i}(k_k z - \omega_k t)} + cc) \\ =& \varepsilon_0 \chi_{ijk}^{(2)} (A_j(z) A_k(z) e^{\mathrm{i}(k_j + k_k) z - \mathrm{i}(\omega_j + \omega_k) t} + \\ & A_j(z) A_k^*(z) e^{\mathrm{i}(k_j - k_k) z - \mathrm{i}(\omega_j - \omega_k) t}) + cc \end{aligned} \tag{2.1.11}$$

with $A_k^*(z)$ being the complex conjugate of $A_k(z)$. From equation 2.1.11, the first exponential term of the polarization oscillates with the sum of two frequencies. This is referred to as sum frequency generation (SFG). If $\omega_j = \omega_k = \omega$, then this process results in second harmonic generation (SHG) where $\omega + \omega = 2\omega$. The second exponential term demonstrates the origin of difference frequency generation (DFG) and can be exploited in other processes such as optical parametric amplification (OPA) which is used routinely in the generation of high-energy few-cycle pulses [75, 76].

2.1.3 Third order nonlinear processes

Cubic response of the polarization to the electric field strength results in the third order nonlinear process i.e. $\tilde{P}_i^{(3)} = \varepsilon_0 \chi_{ijkl}^{(3)} \tilde{E}_j \tilde{E}_k \tilde{E}_l$ with $\chi_{ijkl}^{(3)}$ being the third order susceptibility and a sum implied according to Einstein's summation principle. Third-order nonlinear processes always involve the interaction of three waves to produce a fourth wave and hence are referred to as four-wave mixing processes. $\chi^{(3)}$ processes are responsible for various wave mixing processes such as self-phase modulation (SPM), cross-phase modulation (XPM), third harmonic generation (THG), stimulated Raman scattering (SRS) and other degenerate and non-degenerate four

wave mixing (FWM) processes. A general overview of these processes are provided in [77]. Generally in third order polarization, three incident waves with frequencies ω_1, ω_2, ω_3 interact in a medium to generate a fourth frequency ω_4

$$E(t) = E_1 + E_2 + E_3 = \frac{1}{2}\{E(\omega_1)e^{\mathrm{i}(\omega_1 t)} + E(\omega_2)e^{\mathrm{i}(\omega_2 t)} + E(\omega_3)e^{\mathrm{i}(\omega_3 t)} + cc\}$$

Assuming a linearly polarized electric fields along the y-axis propagating in the z-direction,

$$E_y(\vec{r},t) = A_y(\vec{r},t)\cos(\omega t) = \frac{A_y(\vec{r},t)}{2}(e^{-\mathrm{i}\omega t} + c.c.) \tag{2.1.12}$$

with $\vec{r} = (x, y, z)$ being the coordinates and again assuming that $\omega_1 = \omega_2 = \omega_3 = \omega$ and that the amplitude A_y is real. This implies the third order nonlinear polarization along the same axis is given by [76]:

$$\begin{aligned}
P_y^{(3)} =& \varepsilon_0 \chi^{(3)}_{yyyy} E_y^3(\vec{r},t) \\
=& \frac{\varepsilon_0}{8}\chi^{(3)}_{yyyy}\left[A_y^3(\vec{r},t)\left(e^{-\mathrm{i}(\omega+\omega+\omega)t} + c.c.\right) + 3A_y^3(\vec{r},t)\left(e^{-\mathrm{i}(\omega+\omega-\omega)t} + c.c.\right)\right] \\
=& \frac{\varepsilon_0}{8}\chi^{(3)}_{yyyy}[A_y^3(\vec{r},t)(e^{-\mathrm{i}3\omega t} + c.c.) + 3A_y^3(\vec{r},t)(e^{-\mathrm{i}\omega t} + c.c.)] \\
P_y^{(3)} =& \frac{\varepsilon_0}{4}\chi^{(3)}_{yyyy}[A_y^3(\vec{r},t)\cos(3\omega t) + 3A_y^2(\vec{r},t)E_y(\vec{r},t)]
\end{aligned} \tag{2.1.13}$$

The first term in the bracket shows third harmonic generation (THG) which depicts the NL polarization oscillating with 3ω. The second bracket term shows the original field $E_y(\vec{r},t)$ modulated by the intensity $I_y(\vec{r},t) \sim A_y^2(\vec{r},t)$ depicting a self modification of the fundamental pulse. If the intensity varies over time, the resulting nonlinear phase will also be time dependent. This leads to self phase modulation (SPM) described in section 2.1.3.1 below.

From equation 2.1.4, it is evident that the response of any dielectric material thus depends on two main variables ie the strength of the electric field $\vec{E}$ and the susceptibility of the material to respond to the electric field. Typical system responses to the variables are shown in figure 2.1 based on first, second and third order χ values of 1, 1.94×10^{-12} m/V and 3.78×10^{-24} $\mathrm{m}^2/\mathrm{V}^2$ respectively[78]. It can be seen that the higher the intensity of the applied field, the more noticeable the higher order nonlinearities become.

2.1.3.1 Self Phase Modulation

Self phase modulation (SPM) is a transient phenomenon in which a pulse travelling through a nonlinear (NL) medium encounters a time-dependent index of refraction. It arises as a result of the intensity dependence of the refractive index [79] and is the dominant nonlinear process in the generation of new frequencies in a material of normal dispersion [80].

Due to the NL refractive index dependency on intensity, the time dependence relation of the refractive index $n(t)$ and intensity $I(t)$ can be written (to a first order) by the optical Kerr effect as [78]

$$n(t) = n_0 + n_2 I(t) \tag{2.1.14}$$

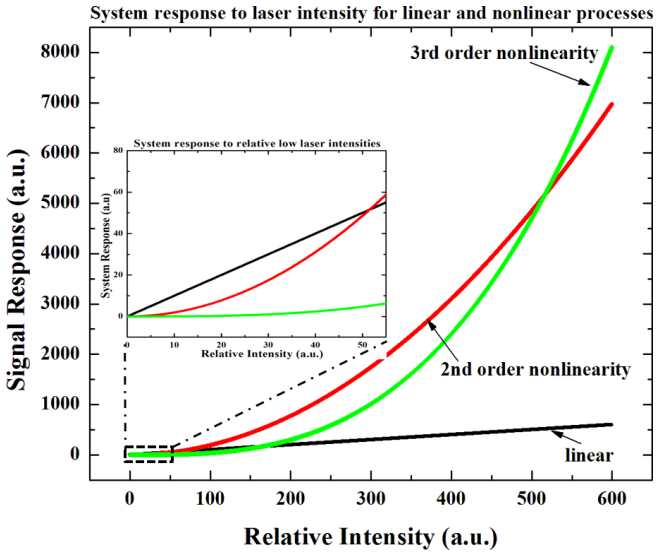

Figure 2.1: Relationship between applied laser intensity and generated system responses for linear and nonlinear processes (not drawn to scale). The inset shows the relationship at lower field intensities. Linear responses are shown in black, second and third order nonlinear responses are shown in red and green respectively. One can observe that at low intensities, the linear processes dominate but as the intensity increases, the higher order processes become noticeable.

where $I(t) = 2n_0\varepsilon_0 c|\tilde{A}(z,t)|^2$ and n_0 and n_2 are the linear and nonlinear refractive indices respectively. Assuming an instantaneous medium response to the pulse intensity and a small propagation length (z) so as to eliminate optical pulse reshaping in the medium, the phase of the pulse changes by

$$\phi_{NL} = -n_2 I(t)\omega_0 z/c \tag{2.1.15}$$

For a propagating pulse, this time-varying phase results in the spectral broadening of the incident pulse and the generation of a continuum of frequencies. The instantaneous angular frequency $\omega(t)$ of the pulse is given by

$$\omega(t) = \omega_0 + \frac{d\left(\phi_{NL}(t)\right)}{dt} \tag{2.1.16}$$

The separation of the new spectral components from the carrier angular frequency ω_0 increases with nonlinearity, peak power and propagation distance [81]. Although self-phase modulation produces symmetrical spectrally broadened pulse thus suggesting a pure phase shift which maintains the pulse envelope in time, material dispersion causes the pulse to also spread in time. Simulations into the effects of SPM in conventional optical fibre and ANDi-PCFs have been previously discussed by Heidt [81].

The propagation of ultrafast laser pulses in Photonic crystal fibres (PCF) can induce a large SPM to produce a white-light supercontinuum. This process is known as supercontinuum (SC) generation. In order to generate SC pulses, there is the need for pumping with high intensity pulses and thus the need for ultrashort laser pulses.

2.2 Ultrashort pulses

Optical pulses generated by mode-locked lasers can have very short pulse durations. Such pulses are commonly referred to as ultrashort pulses and typically occur on time scales ranging from picoseconds (10^{-12} s) to femtoseconds (10^{-15} s) although the use of attosecond (10^{-18} s) time scale pulses have reported [82–84]. Ultrashort pulses can produce high peak powers with very low pulse energies. For example, consider a pulsed laser with pulse energy of 12.5 nJ having a pulse duration of 80 fs. Then from the relation: Peak power = Pulse energy/pulse duration, a peak power of 156 kW is generated. High peak power (or intensity) ultrashort pulses have been applied in the study of many processes such as laser machining and ablation and multiphoton imaging and spectroscopy among others [85–87]. In microscopy for instance, femtosecond time scales have paved the way for the study of many processes such as DNA damage and repairs [30].

Due to the nature of ultrashort optical pulses, they inherently support a large frequency bandwidth ($\Delta\omega$). This can be illustrated using the time-bandwidth product derived from the uncertainty principle for the energy-time,

$$\Delta E \Delta t \geq \hbar \tag{2.2.1}$$

with ΔE and Δt being the standard deviation in energy and time for one standard deviation change respectively and $\hbar$ = Planck's constant$(h)/2\pi$. Given that $E = \hbar\omega$, it can be written as

$$\Delta\omega\Delta t \approx constant \tag{2.2.2}$$

which shows the inverse relationship between the frequency bandwidth ($\Delta\omega$) and pulse duration (Δt) for transform limited pulses. Thus, ultrashort pulse generation generally requires the use of lasers with large gain bandwidth. This makes titanium-doped sapphire (Ti:Al_2O_3) (Ti-Sapp) lasers ideal due to their large gain bandwidth (about 300 nm around a central wavelength of 800 nm resulting in over 10^6 longitudinal modes) and broad tuning range. Ti:Sapp lasers are mode-locked through the optical Kerr effect where an intensity dependent refractive index $n = n_0 + n_2 I$ is induced in the Ti:Sapp crystal by the third order nonlinear susceptibility tensor $\chi^{(3)}$.

2.2.1 Pulse representation

Descriptions of the electric field can be given in frequency or time domain. For a monochromatic wave of frequency ω and position $\vec{r}$,

$$\vec{E}(\vec{r},t) = \vec{E}_0 e^{\mathrm{i}(\vec{k}\cdot\vec{r}-\omega t)} \tag{2.2.3}$$

and for a frequency continuum field

$$\vec{E}(\vec{r},t) = \frac{1}{2\pi}\int_0^\infty \tilde{E}(\omega) e^{\mathrm{i}(\vec{k}\cdot\vec{r}-\omega t)} d\omega \tag{2.2.4}$$

where $\tilde{E}(\omega)$ is the pulse envelope in angular frequency domain. Considering only the electric field variation as a function of time, pulses can thus be represented as

Fourier transform pairs such that

$$E(t) = \frac{1}{2\pi}\int_0^\infty \tilde{E}(\omega)e^{-\mathrm{i}\omega t}d\omega \tag{2.2.5}$$

and

$$\tilde{E}(\omega) = \int_0^\infty E(t)e^{\mathrm{i}\omega t}dt \tag{2.2.6}$$

Taking the time dependent phase $\phi(t)$ into account,

$$\tilde{E}(\omega) = \int_0^\infty E(t)e^{\mathrm{i}\phi(t)}e^{\mathrm{i}\omega_0 t}dt \tag{2.2.7}$$

where ω_0 is a carrier frequency of the pulse envelope with $E(t)$ being the field envelope. From equation 2.2.7, the total phase of the pulse can be written as

$$\phi_{Total}(t) = \phi(t) + \omega_0 t \tag{2.2.8}$$

which gives an instantaneous frequency of

$$\omega_{inst}(t) = \frac{d}{dt}(\phi_{Total}(t)) = \frac{d}{dt}(\phi(t)) + \omega_0 \tag{2.2.9}$$

where ω_0 is now the carrier frequency at the peak of the pulse. A pulse is chirped (frequency modulated) if there is a temporal change in the instantaneous frequency such that $d\phi/dt = f(t)$. Pulses can either be positively/negatively chirped in time when

$$\frac{d^2\phi}{dt^2} > /< 0. \tag{2.2.10}$$

For a pulse traversing a medium, this chirp is as a result of material dispersion in the medium.

2.2.2 Dispersion

The propagation of a broadband ultrashort laser pulse through a dielectric medium results in the dispersion of the spectral components of the pulse due to the frequency dependence of the refractive index $n(\omega)$ of the medium.

The spectral components therefore travel with different speeds which results in the modification of the temporal pulse. More precisely, each of the spectral components of the pulse, propagating through a dispersive medium of length L will acquire a phase shift given by,

$$\phi(\omega) = k(\omega)L \tag{2.2.11}$$

where $k(\omega) = n(\omega)\omega/c$ is the frequency dependant propagation constant, $n(\omega)$ the refractive index and c the speed of light. The functional dependence of phase shift, or rather the relative phase shift between the spectral components contained in the pulse, determines how the pulse profile changes as it propagates through the medium. For the propagation of an ultrashort pulse through a dispersive medium, the velocity at which the pulse envelope propagates is of key importance. This velocity, known as

the group velocity v_g, is defined as the inverse derivative of the propagation constant with respect to the angular frequency:

$$\frac{1}{v_g(\omega)} = \frac{dk}{d\omega} = \frac{n(\omega)}{c} + \frac{\partial n}{\partial \omega}\frac{\omega}{c} \tag{2.2.12}$$

For a dispersive medium where $\frac{\partial n}{\partial \omega} \neq 0$, the v_g varies as the pulse propagates through the medium. To illustrate the influence this has on pulse propagation, it is customary to compute the Taylor expansion of $k(\omega)$ about a central frequency ω_0 of the pulse

$$k = k_0 + k'(\omega - \omega_0) + \frac{k''}{2!}(\omega - \omega_0)^2 + \frac{k'''}{3!}(\omega - \omega_0)^3 + ... \tag{2.2.13}$$

where (...) corresponds to higher order expansion terms. Substituting eqn.2.2.13 into eqn.2.2.11 gives a polynomial function of the order $\phi = \phi_0 + \phi' + \phi'' + ...$ where it can be shown that $\phi_0 = k(\omega_0)L$ is related to the phase velocity of the pulse, $\phi' = k'(\omega - \omega_0)L$ relates to the group velocity of the pulse, $\phi'' = k''(\omega - \omega_0)^2 L$ is the phase dispersion term where its coefficient, $k'' = \partial^2 k/\partial\omega^2$, is the group velocity dispersion (GVD),

$$\text{GVD} = \frac{d^2k}{d\omega^2} = \frac{1}{c}\left[2\frac{dn}{d\omega} + \omega\frac{d^2n}{d\omega^2}\right] \tag{2.2.14}$$

The GVD per unit length is the group delay dispersion (GDD). Note that the GVD is a purely medium dependent parameter and is responsible for the temporal pulse broadening and compression.

For dispersed pulses, the uncertainty principle in 2.2.2 also holds. This uncertainty can be rewritten as $\Delta\nu \cdot \Delta t \approx constant$ since $\omega = 2\pi\nu$ with ν being frequency. This implies that as the spectral width ($\Delta\nu$) increases, the temporal width (Δt) decreases and vice versa. Please refer to [88] for detailed derivation with a summary given in appendix A. For a Gaussian pulse, $\Delta\nu \cdot \Delta t \approx 0.441$.

We have discussed ultrashort pulses and seen how dispersion occurs in dispersive materials. Prominent dispersive materials such as plastic [89, 90] and glass [91, 92] have for a long time been used in fibre optics fabrication. The next section discusses a specific process that occurs in certain types of fibres. This process, which has gained prominence in multiphoton microscope in the last few decades, is supercontinuum generation.

2.3 Supercontinuum generation

The propagation of light through any dispersive material results in the spectral dispersion of the light. In a medium of high self phase modulation, a spectral continuum can be generated. This spectral continuum is what is generally referred to as a supercontinuum (SC) [58, 93]. Although the term SC is currently in use, the name has evolved since its discovery in the 1970s from superbroadening through anomalous frequency broadening to a more recent white-light continuum [58]. Figure 2.2 illustrates spectral dispersion of a transform limited pulse propagating through a photonic crystal fibre to produce a chirped supercontinuum pulse.

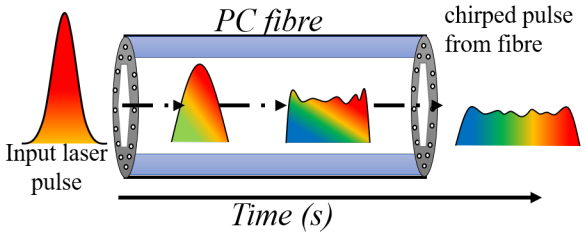

Figure 2.2: Schematic representation of spectral broadening in a PCF showing a chirp-free input pulse and the broadening and evolution of different spectral components in time as the pulse propagates within the fibre. New frequencies are generated as a result of SPM and the chirp as result of material dispersion within the fibre.

Alfano and Shiparo are credited as the first to report of SC generation in a bulk BK7 glass medium by propagating 5 mJ picosecond pulse with bandwidth of 50 nm to span a spectral width of 400 - 700 nm [94]. However, SC generation in bulk materials was found to be complex due to coupling between spatial and temporal effects. This led to the study of SC in conventional optical fibres which involve purely temporal dynamics.

SC generation in conventional fibres can be attributed to different nonlinear processes depending on the dispersion profile of the fibre material and the wavelength of the incident pulse. From expression 2.2.10, this dispersion can either be positive (anomalous) or negative (normal). Anomalous GVD fibres have their zero dispersion wavelength (ZDW) closely matched to the central wavelength of the pump pulse. Normal GVD fibres have their dispersion modified to provide a minimum dispersion wavelength (MDW) close to the central pump wavelength in order to maximize spectral broadening and as close to zero dispersion as possible without exhibiting ZDW as the region of interest [80, 95].

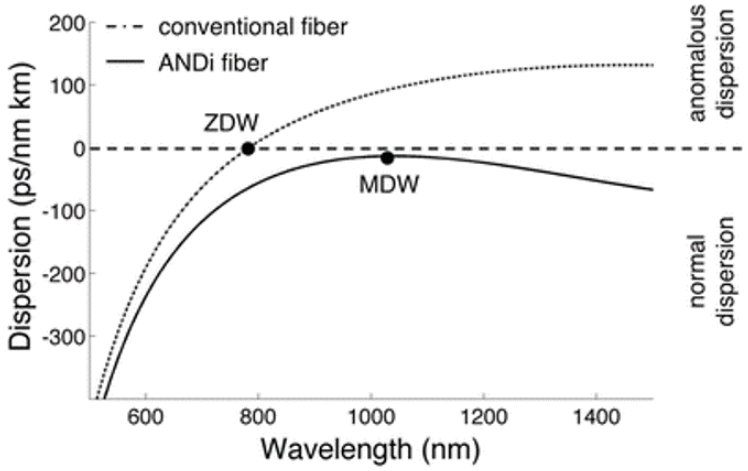

Figure 2.3: Dispersion profiles for the two SC generation concepts showing the regions of anomalous and normal dispersion regions. The ZDW for the conventional fibre is around 780 nm for pump wavelength of 800 nm while the MDW for the normal dispersion is centred around 1050 nm. Profile taken from [80].

Figure 2.3 shows a conventional fibre with a ZDW of 780 nm for a pump wavelength of 800 nm and another fibre with a modified dispersion wavelength of 1050 nm. It will be noticed that for the conventional fibre, the dispersion mechanism is dependent on the pump wavelength. Pumping below the ZDW results in a negatively chirped pulse and vice versa for pump wavelengths above the ZDW. Fibres that have their entire dispersion profile in the normal region are known as All Normal Dispersion (ANDi) fibres and have a negative dispersion irrespective of the pump wavelength. The chirp introduced in the different dispersion regions and a spectrogram of the supercontinuum process are shown in figure 2.4.

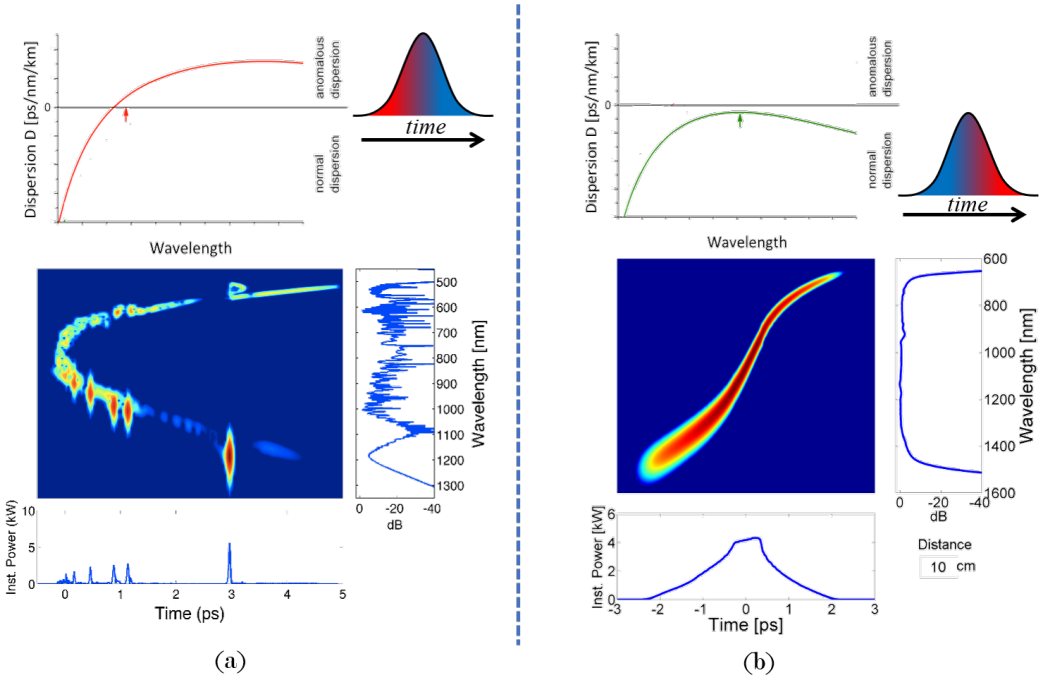

Figure 2.4: Dispersion profiles and simulated spectrograms of supercontinuum generation (SCG) in fibres with (a) a single ZDW with anomalous GVD and (b) SCG in all normal GVD optical fibre. Pump wavelengths are shown with the arrows for each behaviour profile with corresponding spectral dispersion profiles shown. (Profiles and spectrograms taken from [95]).

Spectral broadening in fibres is attributed to cascaded Raman scattering and SPM [58, 81] although the role of cross-phase modulation (XPM) and other four-wave mixing processes in contributing to the production of spectrally smooth output have been reported [80, 96]. Spectral broadening in the anomalous GVD regime (+ve dispersion) is predominantly dominated by optical soliton-related dynamics and was first determined after theoretical analysis of the general nonlinear Schrödinger equation (GNLSE)[58]. Figure 2.4(a) shows the simulated profile and spectrograms for conventional supercontinuum generation (SCG) pumped at the ZDW which is the lowest limit for anomalous dispersion. The high intensities generated in the fibre result in higher order dispersions and Raman scattering which hinder the evolution of the solitons resulting in the breakdown of the pulses through soliton fission giving

rise to extremely complex temporal and spectral profiles with substantial shot-to-shot intensity and phase fluctuations (refer to figure 2.4(a)) thereby making them unsuitable for noise-sensitive applications as well as ultrafast application requiring temporal stability [80, 97, 98].

In the normal GVD region, self-suppression eliminates soliton effects. From 2.4(b), the suppression results in the propagation of a single pulse which broadens in time from its original duration. Supercontinuum generation in the all normal region begins with the symmetric broadening of the pulse by self phase modulation (SPM) to form spectral side lobes which are red and blue shifted on the leading and trailing pulses edges respectively as explained by Heidt et al [99]. Due to the normal dispersion at all wavelengths in this region, the blue shifted tail is overtaken by the faster red shifted edge resulting in optical wave breaking (OWB) which is a degenerate four wave mixing (FWM) process that adds additional spectral components to both ends of the spectrum thus generating new wavelengths [97, 99]. There is therefore no interference in temporal or spectral profiles as OWB assigns each wavelength to a unique temporal position within the pulse [81, 99, 100].

Working in the normal dispersion thus provides the following advantages: minimum temporal broadening and ultrabroad bandwidth due to low and flat dispersion, uniform and smooth temporal and spectral profiles, absence of spectral fine structure, low noise-sensitivity and better temporal coherence properties since there is no temporal breakup of the seed pulse which is the case of anomalous dispersion. In view of these merits over anomalous GVD fibres, it is essential to work with fibres having all normal dispersion (i.e. ANDi-fibres).

2.4 All Normal Dispersion Photonic Crystal Fibre

This section seeks to give a brief insight into the recently designed dispersion-flattened dispersion decreased all-normal dispersion (DFDD-ANDi) photonic crystal fibres. Consideration will be given to features that make them ideal for supercontinuum generation for biophotonic applications. We shall consider the effects of birefringence in them and how to control these effects if any. We shall not focus on the simulations and models as that has been extensively covered by previous research works at the Laser Research Institute of the Stellenbosch University [81, 95, 98, 99, 101–103].

2.4.1 Structure of ANDi-PCF

Photonic crystal fibres are fibres consisting of a uniform refractive index material with a microstructure lattice of air holes embedded and running along the fibre length unlike the conventional fibres that posses a uniform solid core and cladding having different refractive indices. These air holes have a defined diameter, d and are arranged with a hole-hole separation distance known as the fibre pitch Λ. The size of d and Λ in conjunction with the dispersion profile of the material helps to tailor the dispersion profile of the fibre [104]. There are different types of PCFs such as index guiding (IG) PCF (illustrated in figure 2.5) and photonic bandgap (hollow)

fibres [105, 106]. SC generation are best carried out with IG-PCF and types of these fibres and applications have been described by Jin et al [107].

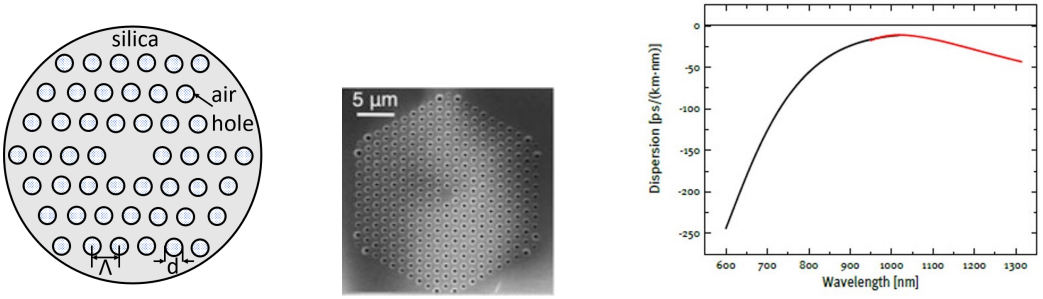

(a) Cross section of hexagonal core PCF

(b) SEM of core structure

(c) Dispersion profile of hexagonal solid core (NL-1050-NEG-1, NKT Photonics)

Figure 2.5: Structure and dispersion profile of hexagonal core ANDi-PCF. SEM image taken from [80] and dispersion profile of NL-1050-NEG-1 with $\Lambda = 1.55$ μm and $d/\Lambda = 0.37$ (taken from [108]).

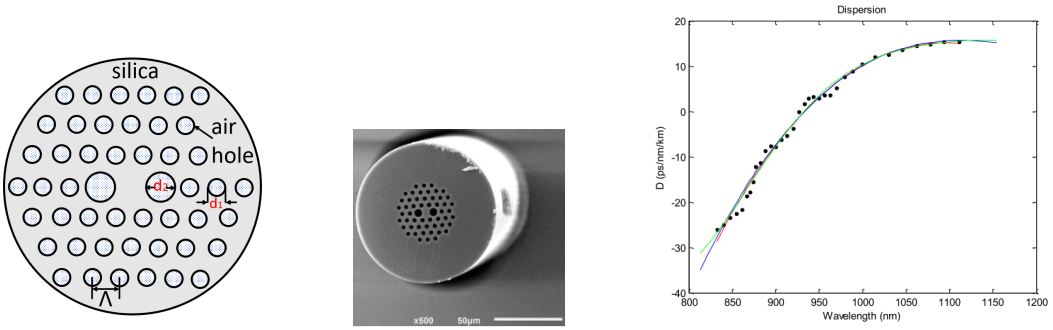

(a) Cross section of PM-PCF

(b) SEM of PM-PCF

(c) Dispersion profile of PM-PCF (NL-1050-PM-NEG, NKT Photonics)

Figure 2.6: Structure and dispersion profile of PM-PCF. SEM image taken from [109] is for illustrative purposes only and does not represent the exact fibre used. The dispersion profile of NL-1050-PM-NEG provided by NKT Photonics. The red and green lines represent the fit for the orthogonal axes and the blue fit line represents the average fit.

In this work, the novel fibres used have been tailored in order to have the entire GVD profile in the normal dispersion region with the minimum dispersion wavelength (MDW) at 1050 nm. Such fibres are referred to as dispersion-flattened dispersion decreased all-normal dispersion (DFDD-ANDi) PCFs and in-depth behaviours of these fibres have been investigated by Heidt [80, 81]. In this work, pumping was carried out at 800 nm meaning there is significant normal dispersion encountered

during SC generation. It is important to note that subsequent reference to PCF or simply fibres implies reference to DFDD-ANDi PCF.

In general, PCFs with d/Λ <0.43 exhibit single mode behaviour with no observed propagation in higher order modes [107]. SC generation require highly nonlinear PCFs which have a high air-fill fraction thus leading to strong confinement and high nonlinear responses and widely tunable and controllable dispersion properties in comparison to that of conventional fibres [107]. PCF structures with perfect rotational symmetry have isotropic refractive index. However, the fibre fabrication and drawing processes introduce some level of asymmetries which can yield some residual birefringence. For this reason, it is important to either find a way of suppressing the effects of induced birefringence by ensuing propagation along a confined one polarization eigen axis or by inducing strong birefringence which is well defined within the PCF during the manufacturing process. The latter approach has led to the development of polarization-maintaining PCF (PM-PCF) which possess an elliptical core structure due to the enlargement of two holes of diameter d_2 (figure 2.6a). This elliptical core creates a fast (minor) axis (crossing the two larger holes) and a slow (major) axis perpendicular to the fast axis. Predictions of the polarization effects and the studies of the optical properties of these fibres have been reported showing that in the PM-PCF, polarization is known to be better confined in the slow axis [110, 111].

As a recap, it has been established that high peak powered pulses injected into PCFs induce higher order nonlinearities within the fibre. Self phase modulation is the dominant nonlinear process for supercontinuum generation as it results in the generation of new frequency components. Material dispersion within the PCF causes the SC pulse to broaden in time thereby introducing a phase difference between the spectral components. In order to regenerate transform limited pulses, it is essential to determine the phase added as a result of the dispersion and compensate for it accordingly. The next section discusses the phase measurements techniques which can be used for pulse compression.

2.5 Phase measurement and pulse compression

Measurement of ultrafast pulses have evolved over the last few decades with different techniques and variations being implemented due to the inability of fast detectors to directly measure pulse features. There are many techniques to measure the pulse duration and characterise the electric fields of ultrafast laser pulses in terms of phase and amplitude [112–115]. Depending on the signal detection system, these measurements can be carried out in either the spectral or temporal domain. Temporal domain techniques involve measuring pulse characteristics directly in the time domain using appropriate photo detectors. Measuring an event in time requires comparison with an event on a shorter time scale. However with ultrashort time scale being the shortest time scale, it is not possible to compare them on any other shorter time scale. Therefore temporal pulse characterisation often require an intensity autocorrelation with the pulse measured relative to itself or some form of spectral interferometric technique such as Frequency Resolved Optical Gating (FROG) [116] and Spectral

phase interferometry for direct electric-field reconstruction (SPIDER) [117].

In this section we discuss the concepts, process and some spectral domain techniques that were employed in our phase measurements. We will however not touch on the characterization of the exact laser used in this work as it has been discussed by Bosman [118].

2.5.1 Spectral domain phase measurement techniques

Spectral domain pulse characterization techniques are measurements carried out in the frequency domain and require the use of spectrometers for signal detection. It involves measuring spectrograms of the pulse.

2.5.1.1 Frequency Resolved Optical Gating

Pulses can be characterised both in time and frequency domain by the implementation of a frequency resolved optical gating (FROG) technique [115]. Frequency resolved optical gating (FROG) is an ultrashort pulse characterization technique that permits the measurement of key pulse features such as pulse duration, time-dependent electric field and/or frequency-dependent spectral phase [116]. It requires the splitting of the pulse to be measured into two replicas and crossing them in a nonlinear-optical medium [119]. Spectrograms of the nonlinear signal responses are recorded as a function of the delay between the two pulses to produce a FROG trace from which pulse information can be retrieved using FROG algorithms. There are different versions of FROG depending on the gating mechanism with the most popular variant being the second-harmonic FROG (SHG-FROG) which is based on measurements from a pulse interacting with a copy of itself in a second order (χ^2) nonlinear crystals and can therefore provide much higher sensitivity although phase-matching has to be carefully treated to eliminate pulse distortions [119]. Cross-correlation FROG (XFROG) permits the use of an additional fully characterised (known) intense reference pulse over the unknown pulse to be characterised. It is more versatile and easier to perform as it does not require spectral overlap of the known and unknown pulses and it does not require spectral interferometric alignment accuracy [115]. It is mostly used in situations where the use of normal FROG is limited such as when the signal pulses are so weak to the extent that SHG-FROG cannot retrieve them [114]. Other nonlinear geometries such as polarization-gated FROG, self-diffraction FROG, transient-gating FROG have been discussed in detail by Trebino [115, 116]. Avoiding losses in temporal resolution as a result of finite beam angles when characterizing few-cycle pulses led to the creation of the collinear geometry which include interferometric FROG (IFROG).

2.5.1.2 Collinear Interferometric Frequency Resolved Optical Gating

Standard SH-FROG, being a non-collinear technique, can be affected by geometrical smearing of the pulse structure as a result of the finite crossing beam angles which affects the quality of response especially when working with few-cycle pulses [120]. To circumvent this, SH-FROG can be extracted using interferometric FROG (IFROG).

IFROG works by spectrally resolving an interferometric autocorrelation. It employs collinearly propagating beams and is the simplest FROG variation that can be implemented in a pulse shaper [121]. IFROG in collinear geometry allows for tight focusing which makes it more ideal for measuring pulses with low peak powers or when extremely thin nonlinear crystals are used. Furthermore, apart from algorithmic pulse reconstruction, the conventional non-collinear FROG trace can be extracted from IFROG [122].

Considering a complex electric field

$$\xi(t) = E(t)e^{\mathrm{i}\omega_0 t} \tag{2.5.1}$$

where $E(t)$ and ω_0 represent the complex amplitude and carrier frequency respectively. Gating with a copy of the pulse itself with a relative delay of τ, the second complex electric field is given by

$$\xi(t-\tau) = E(t-\tau)e^{\mathrm{i}\omega_0 t} \tag{2.5.2}$$

The corresponding measured SHG IFROG intensity is given by

$$I^{SHG}_{IFROG}(\omega,\tau) = \left|\int_{-\infty}^{+\infty}(\xi(t)+\xi(t-\tau))^2 e^{-\mathrm{i}\omega t}dt\right|^2 \tag{2.5.3}$$

For the two pulses, the second harmonic (SH)-FROG field is given by

$$E_{FROG}(\Delta\omega,\tau) = \int_{-\infty}^{+\infty}(E(t)E(t-\tau))^2 e^{-\mathrm{i}\Delta\omega t}dt \tag{2.5.4}$$

where $\Delta\omega = \omega - 2\omega_0$ and for a single pulse, the second harmonic field is given by

$$E_{SH}(\Delta\omega) = \int_{-\infty}^{+\infty} E^2(t)e^{-\mathrm{i}\Delta\omega t}dt|_{\tau=0} = E_{FROG}(\Delta\omega,\tau=0) \tag{2.5.5}$$

A Fourier transform of equation 2.5.3 with respect to τ results in

$$I^{SHG}_{IFROG}(\omega,\tau) = \left|E_{(SH)}(1+e^{-\mathrm{i}(2\omega_0+\Delta\omega)\tau}) + 2E_{FROG}(\Delta\omega,\tau)e^{-\mathrm{i}\omega_0\tau}\right|^2 \tag{2.5.6}$$

which upon expansion reduces to

$$\begin{aligned} I^{SHG}_{IFROG}(\omega,\tau) &= 2|E_{(SH)}(\Delta\omega)|^2 + 4|E_{FROG}(\Delta\omega,\tau)|^2 \\ &+ 8cos[(\omega_0+\frac{\Delta\omega}{2})]Re[E_{FROG}(\Delta\omega,\tau)E^*_{SH}(\Delta\omega)exp(\mathrm{i}\frac{\Delta\omega}{2}\tau)] \\ &+ 2cos[(2\omega_0+\Delta\omega)\tau]|E_{SH}(\Delta\omega)|^2 \end{aligned} \tag{2.5.7}$$

Equation 2.5.7 consists of the SH-FROG trace and the delay-independent background as the first two terms. The interferometric contribution and the SH background are given as the third and fourth terms respectively. The interferometric technique thus provides the opportunity to filter out the background from the trace.

2.5.1.3 Multiphoton Intrapulse Interference Phase Scan

Multiphoton Intrapulse Interference Phase Scan (herein referred to as MIIPS) is a collinear non-interferometric phase recovery technique that permits the iterative spectral phase characterization and compensation of femtosecond laser pulses. MIIPS is primarily used to measure and compensate for spectral dispersion in order to produce a transform limited pulse after a dispersive medium unlike conventional cross correlation pulse measurement techniques such as FROG [116], SPIDER [117] and background-free autocorrelation which measure only pulse characteristics and require an autocorrelation or a cross correlation of two pulses to generate a signal. MIIPS entails the modulation of the spectral phase of the pulse while simultaneously recording the SHG spectra. Phase information is therefore measured directly from the SHG spectrum of the pulse under investigation. It entails the use of a pulse shaper such as a 4f shaper combined with a spatial light modulator (SLM) along with an iterative algorithm to measure the group delay dispersion (GDD) and to compensate for this measured phase distortion [67]. Unlike other techniques, the use of beam splitters, autocorrelation or interferometry is not required. These are some of the fundamental advantages of MIIPS over FROG and SPIDER [123].

The working principles of MIIPS are discussed in the works of Dantus [62, 63, 124]. It basically works by adding a periodic guess phase as a reference phase function to the phase of the input pulse and determining the influence of this phase change on the SHG spectrum of the pulse.

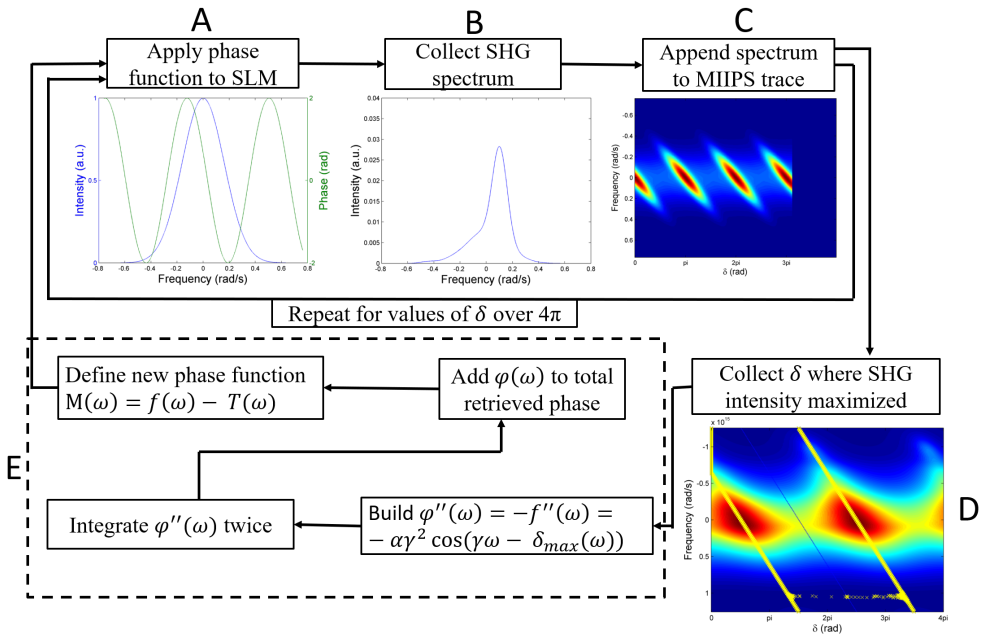

Figure 2.7: Schematic diagram of the MIIPS process. This includes the definition and application of reference phase function onto the SLM (A), scanning over the laser pulse to measure the SHG for each spectral phase (B). The SHG spectrum is recorded (C) and the region where the scanning parameter δ is maximised is recorded (D). The process of retrieving the phase is summarized in section E.

For every spectral component in the pulse, the accompanying second harmonic generated is proportional to the auto-convolution of the frequency domain electric field [64]

$$E(2\omega) = \int |E(\omega+\Omega)||E(\omega-\Omega)|e^{\mathrm{i}[\phi(\omega+\Omega)+\phi(\omega-\Omega)]}d\Omega \tag{2.5.8}$$

with SHG intensity given by $|E(2\omega)|^2$ and the total spectral phase written as $\phi(\omega) = \psi(\omega)+f(\omega)$, where $\psi(\omega)$ and $f(\omega)$ represent the unknown input laser phase and guess reference phase functions respectively. The aim of the technique is to determine the guess phase function parameters for which the second harmonic intensity is maximised for each component. The guess phase function is a sinusoidal function given by

$$f(\omega) = \alpha\cos(\gamma(\omega-\omega_0)-\delta) \tag{2.5.9}$$

where α is the amplitude, γ is the duration of the guess reference phase function and is inverse of the modulation frequency and δ is the scanning parameter ensuring that reference function samples all the frequencies in the bandwidth in order to determine the phase deviation across the entire spectrum [124]. A Taylor expansion of the phase term and neglecting third and higher order terms gives:

$$E(2\omega) \approx e^{2\mathrm{i}\phi(\omega)} \int |E(\omega+\Omega)||E(\omega-\Omega)|e^{\mathrm{i}[\frac{\partial^2\phi(\omega)}{\partial\omega^2}]}d\Omega \tag{2.5.10}$$

with the GDD $= \frac{\partial^2\phi(\omega)}{\partial\omega^2}$. The SHG is maximised when the GDD is zero such that

$$\frac{\partial^2\phi(\omega)}{\partial\omega^2} = \psi''(\omega)+f''(\omega) = 0 \tag{2.5.11}$$

$$\psi''(\omega) = -f''(\omega) = -\alpha\gamma^2\cos[\gamma(\omega-\omega_0)-\delta_{max}(\omega)] \tag{2.5.12}$$

From equation 2.5.12, the unknown phase can be determined from the maximum of the ψ''

$$|\psi''(\omega)| = \alpha\gamma^2 \tag{2.5.13}$$

A first estimate of the GDD is derived by substituting $f''(\omega)$ for each frequency ω from which a double integration results in the first estimated spectral phase which from equation 2.5.12 is the negative of the phase. Adding this phase to the SLM and repeating the process for a number of times until the phase converges ensures that a maximum phase retrieval is achieved. This process provides simultaneous phase measurement and compression which is a key merit of MIIPS. The MIIPS process is summarized in figure 2.7. Although MIIPS offers simultaneous phase measurement and temporal compression and is insensitive to phase matching in the nonlinear medium, it is limited in the dispersion orders it can compensate for. MIIPS only considers second order dispersions corrections and neglects higher order dispersions [67, 124]. It also requires repetitive measurements making it relatively time consuming.

2.5.1.4 Ptychography

This work involves the use of time domain ptychography. It is a modification of spatial ptychography which is known to be a robust lense-less imaging technique used to recover lost phase information of an object [125]. Spatial ptychography involves the iterative reconstruction of the real space image of an object from a series of far-field diffraction patterns. The diffraction patterns recorded between successive iterations are from overlapping regions as a result of transverse shifts in the illumination beam. This shift is achieved by either moving the object or the illumination source. The larger the overlapping regions, the better the phase exacted and the redundant information from this region helps to improve the convergence of the phase reconstruction algorithm [126]. In spatial ptychography, an object $o(x)$ is illuminated by a known probe beam at a known position $p(x - x_1)$ where x_1 is the position of the probe relative to the object positions (x) and the far field diffraction patterns $I_n(X)$ at positions (X) is given by

$$I_n(X) = |\mathscr{F}\{o(x)p(x - x_1)\}|^2 \tag{2.5.14}$$

with $\mathscr{F}$ and 'n' being a Fourier transform operator and iteration number respectively. The diffraction patterns produce a spectrogram and the real space amplitude and phase are retrieved by feeding the recorded spectrogram into a ptychographic iterative engine (PIE) [127].

Spangenberg et al. adapted this spatial technique into the temporal domain by recording the diffraction patterns in time instead of spatial coordinates. This is what is referred to as time domain ptychography [69, 126]. By analogy, beam position is a temporally delayed probe $P(t - \Delta t)$ and a recorded spectrum $I_n(\omega)$ serves as the far field diffraction measurement. The spectrum is achieved by the product of the probe with an object $O(t)$ such that

$$I_n(\omega) = |\mathscr{F}\{O(t)P(t - \Delta t)\}|^2 \tag{2.5.15}$$

Time domain ptychography starts by defining an arbitrary choice of object function which is multiplied by a defined time delayed probe function. The product of the object field in frequency $G_n(\omega, n\Delta t)$ can be determined from the Fourier transform of the product of the object field in time $G_n(t, n\Delta t)$ and replaced with the measured spectrum $S(\omega, n\Delta t)$ (with the phase preserved). A new exit field $G'_n(\omega, n\Delta t)$ can be calculated using the square root of the measured spectral amplitude while maintaining the spectral phase $(\angle)$ of the exit field such that $G'_n(\omega) = \sqrt{S_n(\omega)}\exp(\mathrm{i}\angle(G(\omega))$ upon which the corresponding exit field back in the time $G'_n(t) = (t, n\Delta t)$ can be determined by taking an inverse Fourier transform. The new object field in time, $O'_n(t)$, is obtained by feeding the temporal exit field into a time domain PIE algorithm for reconstruction. A schematic for this reconstruction algorithm is illustrated in [126]. For each exit field and its corresponding updated exit field, the difference is used to correct the object function

$$O_{n+1}(t) = O_n(t) + \beta U(t - n\Delta t) \times [G'_n(t, n\Delta t) - G_n(t, n\Delta t)] \tag{2.5.16}$$

where the weighting function $U(t)$ is defined as

$$U(t) = \frac{|P(t)|}{\max(|P(t)|)} \cdot \frac{|P(t)^*|}{|P(t)|^2+\alpha} \tag{2.5.17}$$

α <1 is determined by the noise level of the system and 0< β <1 is determined by the pulse duration. If the probe is to be updated, then an extended PIE (ePIE) algorithm [128] is required where the probe is updated by

$$U(p) = \frac{|E(t)|.E(t)^*}{E_n \times (|E_n|^2+\alpha)} \tag{2.5.18}$$

2.5.1.5 Collinear time domain ptychographic phase measurement

This is a modification of the time-domain ptychographic iterative engine in a single beam geometry and thus termed as collinear ptychographic phase measurement. It employs a single beam approach as opposed to having separate object and probe pulses. Similar to MIIPS, pulse characterisation occurs at the position of the sample, after the focus of the microscope objective and also requires an SLM in a pulse shaper to generate an object and probe pulse from the single beam. The reconstruction algorithm is as shown in fig.2.8.

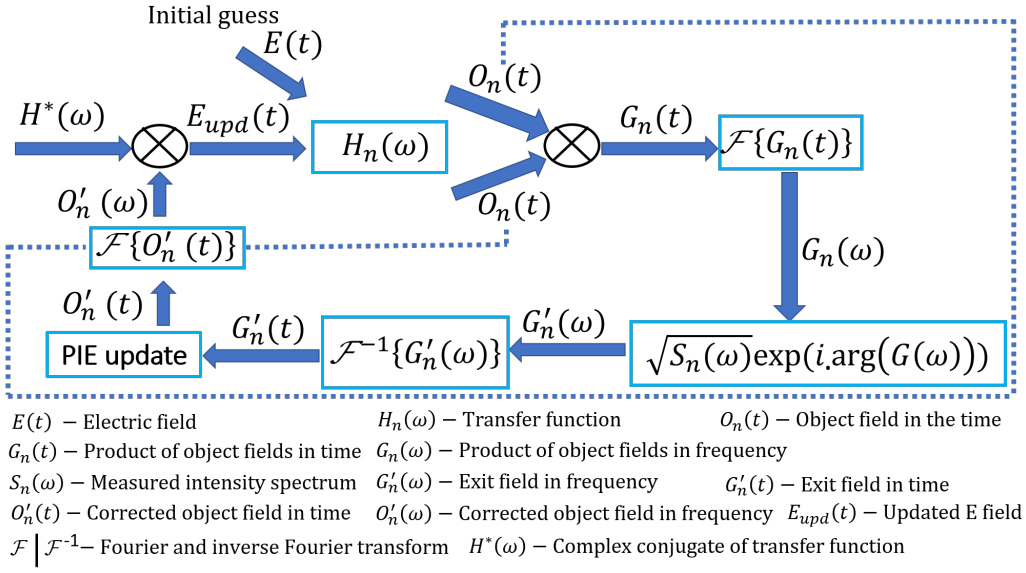

Figure 2.8: Schematic diagram of how the time-domain ptychographic phase measurement process works. The initial guess field is applied to a transfer function to generate an object function which is Fourier transformed to produce a spectrum. The amplitude of the spectrum is analysed with the PIE algorithm after an inverse Fourier transform in order to generate the corrected object function. The update steps is enclosed within the dotted lines.

It involves the use of a spectrogram $S_n(\omega)$ as an input where n denotes the acquired spectrogram number. This spectrogram is recorded by multiplying an electric field $E_0(t)$ to a known quadratic phase-only transfer function

$$H_n(\omega) = \exp(\mathrm{i}(\omega^2 q.s_n)) \tag{2.5.19}$$

where ω is the angular frequency for each nth measured spectrum and q is the quadratic phase on the SLM for each scan step s. The q parameter is scanned between a maximum and a minimum quadratic phase where $q_{min} = -q_{max}$. The spectrogram is then generated through a Fourier transform ($\mathscr{F}$) of the product of $O_n(t)$ with itself after focusing into a nonlinear crystal to generate a frequency doubled light.

$$S_n(\omega) = |\mathscr{F}\{O_n(t)\}^2|^2 \tag{2.5.20}$$

Due to the measurement of the square of an output object field after applying a known transfer function to the input electric field, this technique is known as i^{2}PIE [70] and will be referred to as such throughout this report. The recorded spectrum is Fourier transformed into the temporal domain and fed into the time domain PIE algorithm [129] to produce a new object function $O_n^{'}(t)$ which results in $O_n(\omega)$ upon an inverse Fourier transform. The final step unique to i^{2}PIE is the update of the current electric field estimate to generate a new electric field E_{upd}

$$E_{upd}(\omega) = O_n^{'}(\omega)H_n^*(\omega) \tag{2.5.21}$$

where $H_n^*(\omega)$ is the complex conjugate of the initial transfer function $H_n(\omega)$.

Collinear ptychographic phase measurement (i^{2}PIE) offers a number of advantages over MIIPS as a pulse characterization technique. In i^{2}PIE, only a single scan needs to be taken after which the measured spectrogram is passed to the PIE reconstruction algorithm whereas MIIPS requires multiple scans and a feedback system for characterization making i^{2}PIE a faster technique. Furthermore, i^{2}PIE enables the reconstruction of not only the phase information but the amplitude information as well. The lack of amplitude reconstruction is a limitation of the standard MIIPS which is a phase-only characterization technique [64]. Furthermore, this collinear i^{2}PIE technique is not limited to second order dispersions only as in the case for MIIPS but can characterize higher order dispersions as well.

2.5.2 Pulse compression

Pulse compression is a method of reducing the pulse duration of ultrashort pulses. The process is used to compensate for chirp resulting from dispersion. It can be achieved using different dispersive optical elements and in specific geometric configurations. Common optical elements used include chirped mirrors, prism pairs and diffraction gratings.

As previously stated, MIIPS measures the spectral phase. Using a pulse shaper, a negative value of the measured phase can be added to the SLM in order to compensate for any phase difference and produce a transform limited pulse (refer to equation 2.5.12). Likewise, time domain ptychography can be used to determine the unknown spectral phase of a temporally stretched pulse, and therefore the pulse shaper can again be used to apply the appropriate phase retardation values in order to compensate for the dispersion and compress the pulse. Therefore, aside the optical elements, pulse shapers can be used for pulse compression as have been demonstrated by [63, 70, 129]. A combination of static optical elements and pulse shaper provides better compression as they compliment each other with the chirped mirrors reducing

the amount of phase that the 4f-shaper has to compensate for thus making it more efficient. The 4f-shaper also compensates for phases distortions that the chirped mirrors were not able to correct. In this work, a combination of two chirped mirrors and a pulse shaper was used in the pulse compression.

As stated earlier, the spectral domain phase measurement techniques discussed above have been applied in the nonlinear imaging system developed. The next chapter discusses the specific sections for which these phase measurement techniques applied in pulse compression were employed as well as other materials and methods used in this work.

Chapter 3

Experimental procedures

In this chapter, detailed descriptions of the experimental setup and procedures are provided. The setup for the generation of a broadband supercontinuum (SC) pulse is presented. The system features, procedures for phase measurement and the application of these measured phases to generate near transform limited pulses from the broadband SC pulse are also be presented. The integration of these near transform limited pulses into the custom-built nonlinear microscope are discussed. Calibration of the system and optimization procedures carried out will also be considered.

3.1 Experimental setup

In order to perform multiphoton microscopy, very high peak intensity pulses need to be generated at low average powers. With peak intensity being inversely proportional to the pulse duration, optical pulses with very short durations (ultrashort pulses) are required. In our setup, a femtosecond titanium-doped sapphire (Ti:Sapp) laser was used to pump a photonic crystal fibre whose output was then compressed to generate ultrashort pulses. To create femtosecond pulses, a pulsed Ti:Sapp solid state laser (Spectra-Physics Tsunami) was used. Laser configurations are found in [130]. Its Ti:Sapp rod is pumped with a Nd:YVO_4 pump laser (Spectra Physics Millenia V) and mode-locked with an acousto-optics modulator to generate a spectral output spanning a broad wavelength range (760 -840 nm) in the near infrared (NIR). The spectral output used in this work has an average output power of 1 W and is centred at 800 nm with a spectral width of 13 nm and 80 MHz repetition rate. This output beam is what was used in our microscopy setup. It should be noted that all measurements in this work were carried out with a horizontally polarized beam.

The microscopy imaging system is made up of three distinct sections; supercontinuum generation, phase measurement and pulse compression, and the imaging configuration. These sections will be discussed separately.

3.1.1 Supercontinuum generation: setup and procedure

The supercontinuum generation features tightly coupling a high peak power laser pulse into a highly nonlinear dispersion-flattened dispersion-decreased all normal dis-

persion photonic crystal fibre (DFDD ANDi-PCF). Two types of PCFs were studied, a non polarization maintaining (NL-1050-NEG-1, NKT Photonics) and polarization maintaining (PM-) PCF (NL-1050-PM-NEG, NKT Photonics). It should be noted that the PM-PCF used in this work is an experimental version and therefore the exact details on this fibre is purely dependant information provided by NKT photonics. (The dispersion profiles of the fibres used are shown in figures 2.5 and 2.6 in the previous chapter).

Due to the fabrication method, these fibres are slightly birefringent. For each PCF, light couples into both the fast and slow axes producing two temporally decoupled polarization components. In view of this, and taking into account that polarization is better confined to a particular axis (e.g. better confined in the slow axis for PM-PCF), it is essential to analyse the polarization of the fibre input and output beams for optimal transmission.

As shown in figure 3.1, transmission studies were carried out by placing the PCFs between two half wave plate polarizers (HWP)($\lambda/2$); an 808 nm zero order $\lambda/2$ (Thorlabs) to vary the input wave polarization into the fibre and a broadband achromatic HWP ($\lambda/2$ 690 - 1200 nm (Thorlabs)) to vary the polarization of the SC beam for optimal transmission relative to the horizontal broadband polarizer (Thorlabs LPVIS100, 550 nm - 1.5 μm).

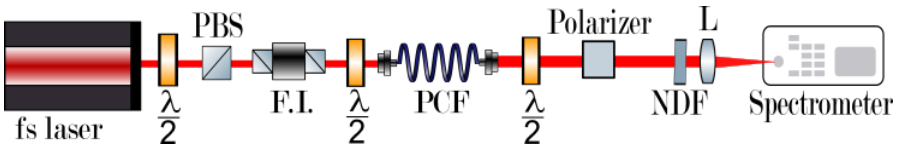

Figure 3.1: Schematic diagram of the supercontinuum generation setup consisting of the the femtosecond (fs) laser; half wave plate ($\frac{\lambda}{2}$); polarization beam splitter (PBS); Faraday isolator (F.I.); photonic crystal fibre (PCF); focusing lens (L); neutral density filter (NDF). The PCF spectral output is broader than the spectral input as a result of the SC generation.

The optimal output from the PCF for a particular axis was obtained by measuring the power after the polarizer with a power meter (Thorlabs PM160D). This was achieved by iteratively measuring the PCF output power for a given polarization as a function of the incident pulse polarization orientation, as controlled by the half wave plate directly in front of the PCF. The exiting SC beam consists of two separate beams corresponding to the fast and slow axes transmissions and are therefore shifted by 90 degrees relative to each other. Therefore the exit beam is a superposition of two $\cos^2$ graphs. The spectral profile of the generated supercontinuum beam was analysed for each input-output polarization pair by coupling into a spectrometer (Avantes AvaSpec-3648). It should be noted that the beam after the polarizer is re-oriented horizontally.

3.1.2 Pulse characterization setup

Knowledge of the nature of the pulse in the object plane is essential in understanding the dynamics of the signal responses measured. In this section, a detailed description

is given into the components and features used in determining the characteristic features of the SC pulse. Pulse characterization techniques used in this imaging setup include broadband dispersion control with chirped mirrors, MIIPS and i^{2}PIE as collinear spectral phase measurement techniques used for pulse compression. The schematic of the characterization and compression setup integrated with the SC generation is shown in 3.2.

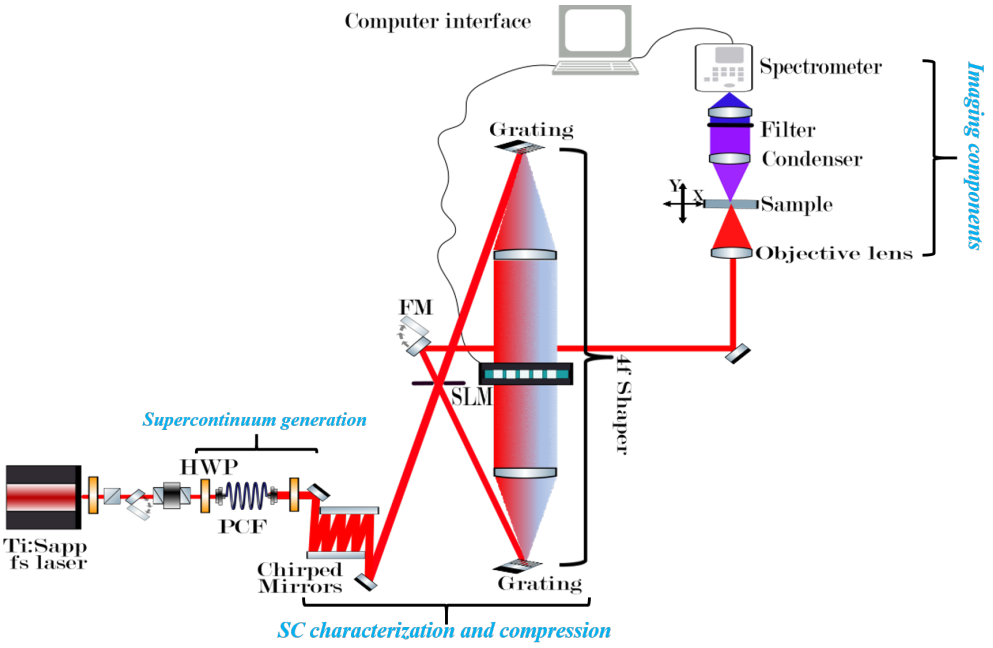

Figure 3.2: Schematic diagram of the compression setup showing the region of supercontinuum generation, pulse characterization and compression as well as imaging configuration.

Figure 3.3 shows the computer-aided design (CAD) of the supercontinuum generation setup and the pulse characterization setup up designed before construction. Separation between the SC generation components and the characterization components is shown with the dash blue line while the red dashed line shows the illumination path used when working with the pulse originating directly from the oscillator. The path of the beam as a result of SC generation is shown with the solid red line.

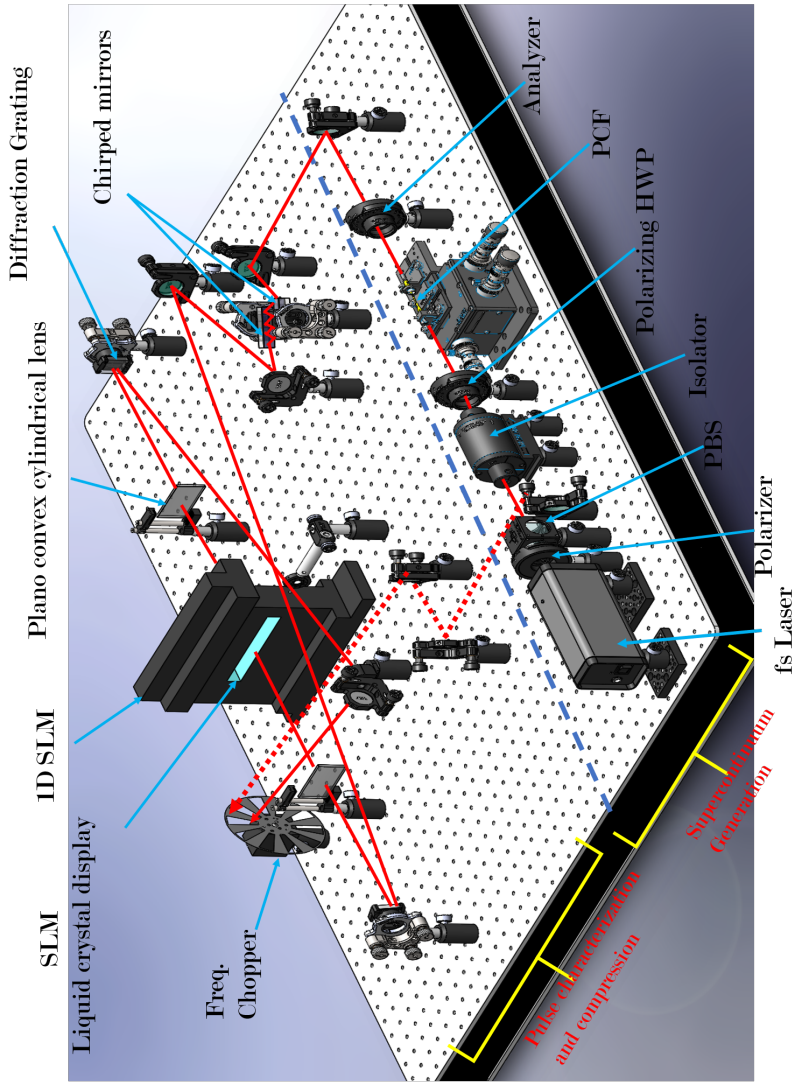

Figure 3.3: CAD model of the supercontinuum generation as well as the phase measurement and pulse compression systems The sections are separated by the blue dashed line. The path of the laser beam when the fundamental beam from the cavity is used in the imaging is shown in the red dashed line while the path for the SC beam is shown in solid red lines. The SC generation and characterization sections are labelled.

As stated in section 2.2.2, the pulse also undergoes dispersion during the SC generation. This dispersion has to be compensated in order to compress the pulse. Pulse pre-compression was carried out by the use of chirped mirrors. The spectrally broadened SC pulse undergoes 48 bounces between two chirped mirrors (Thorlabs DCMP175, 700 nm - 1000 nm, >99% reflectance, -175 fs^2 GDD compression per reflection). The basic working principle of the chirped mirrors is briefly explained in section 3.1.2.1 below.

The pre-compressed beam from the chirped mirrors (which will be referred to as chirped mirror (CM-) compressed pulse for the rest of this report) goes into a pulse shaper consisting of two diffraction gratings (Thorlabs GR13-0608, 600 grooves/mm, 750 nm blaze, 13°0' blaze angle), two plano cylindrical lenses (Laser Components GmbH AR/AR800 RCX12.5-75-113UV) and a 1-D computer addressable spatial light modulator (SLM)(JenOptik SLM 640-d). The components were arranged in a $4f$ configuration similar to that outlined by Weiner et al [131, 132] and elaborated in section 3.1.2.2. After the 4f shaper the pulse is focused into a 100 thick μm β-barium borate (BBO) crystal used to generate SH signals which were collected by a fibre coupled spectrometer (Avantes-AvaSpec-3648) after passing through a band pass emission filter (Thorlabs FBG39) used to block the fundamental laser.

As stated previously above, the phase measurement setup which is subsequently used for pulse compression consist basically of chirped mirrors and a 4f-shaper. The following subsections discusses the major components in the characterization section of the setup.

3.1.2.1 Pre-compression with chirped mirrors

Chirped mirrors (CM) are multilayered mirror coatings that exhibit a constant GDD over a frequency range as a result of the group delay varying linearly with frequency. These layers are made of dielectrics such as silicon dioxide (SiO_2) with refractive index, $n = 1.45$ and titanium dioxide (TiO_2) with $n = 2.3$ [133, 134]. CM work on

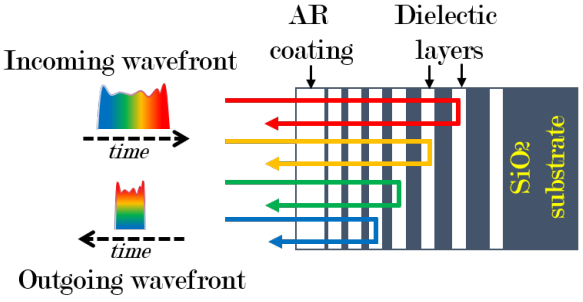

Figure 3.4: Schematic representation of chirped mirrors. Longer wavelengths travel a further distance and are reflected on a deeper layer than shorter wavelengths. The layers consist of SiO_2 and TiO_2.

the principle of interference of light reflected of the different dielectric layers and can be designed to exhibit constant negative GDD for normal dispersion compensation

[133]. Detailed design of each section and derivations of laws governing the functions of chirped mirrors are presented in [134]. In typical glass, longer wavelengths have lower wavelength dependent indices of refraction than shorter wavelengths as such the shorter wavelength components cover a shorter distance through the mirror than the longer wavelength components before being reflected. For example, consider the red and blue wavelengths in figure 3.4. Red light is known to have a longer wavelength ($\approx$ 600 nm) and so travels a longer distance before reflection as compared to the blue with a shorter wavelength ($\approx$ 400 nm). Hence the group delay of the bluer components are less than that of the redder components.

3.1.2.2 4f Shaper

A 4f Shaper is a pulse shaper which makes use of Fourier transform methods to manipulate the phase and amplitude of quasi narrow bandwidth sections of a mode-locked pulse spectrum in order to produce a desired output pulse spectrum and pulse duration. Although there are different configurations [135], the specific configuration used in this work is shown in figure 3.5. This geometry is known as a zero-dispersion compressor because ideally it creates a pulse free of temporal dispersion and therefore produces an output pulse identical to the input pulse. It is however commonly referred to as a 4f shaper due to the configuration of the components.

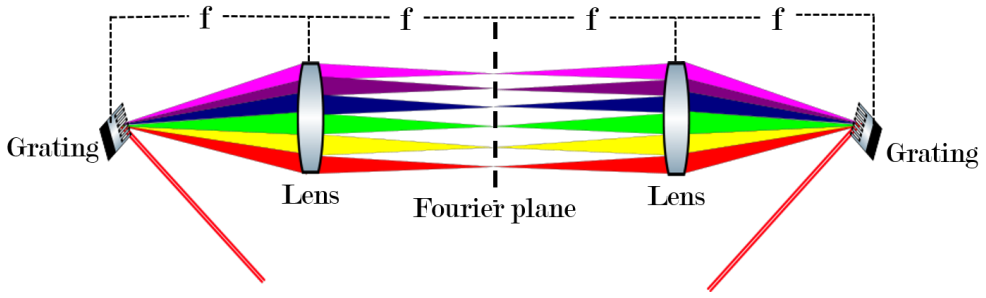

Figure 3.5: Schematic diagram of a Fourier transform pulse shaper showing the projections of spectral components onto the focal plane.

A diffraction grating angularly disperses the incoming pulse into spectral components and projects them onto the back focal plane of a lens placed at its focal length f from the grating. This ensures the projection of a planar wavefront into the Fourier plane. A pulse shaper can be placed as a mask in the Fourier plane to provide active control of the ultrashort pulse reaching the plane. Manipulation of spatial frequencies in the Fourier plane enables filtering of the input field. The second lens and grating are also placed at distances f and $2f$ respectively from the Fourier plane to recombine all the frequencies into a single collimated beam. The shape of this output pulse is determined by the Fourier transform of whatever pattern is transferred by the mask onto the spectrum.

As stated earlier, a liquid crystal spatial light modulator (LC-SLM) was used as a pulse shaper mask in this work although there are many other options such as

acousto-optic elements and deformable mirrors [131]. A LC-SLM in a Fourier transform pulse shaper relies on the Fourier transform between the time and frequency domains and provides an inherent high efficiency compared to the other techniques and is independent of pulse repetition rate [135]. Direct shaping of ultrashort pulses in the time domain is non-trivial due to their short durations. As a result, placing a SLM at the Fourier plane permits the modification of the individual spectral components of the original pulse which translates to changes in the temporal domain. For example, the use of a frequency domain mask function

$$\tilde{M}(\omega) = \tilde{A}(\omega)\exp[i\Delta\varphi(\omega)] \tag{3.1.1}$$

in modulating the incoming spectral electric field $\tilde{E}_{in}(\omega)$ gives an outgoing shaped spectral field such that

$$\tilde{E}_{out}(\omega) = \tilde{M}(\omega)\tilde{E}_{in}(\omega) \tag{3.1.2}$$

From the mask function, it shows modulation of the spectral amplitude $\tilde{A}(\omega)$ and phase $\varphi(\omega)$ are possible. It should be noted that polarization shaping is also possible with the use of a appropriate mask function [136].

3.1.3 Calibration of SLM

Spatial light modulators (SLM) allow for the modulation of phase and/or amplitude of the pulse depending on the number of crystal layers. A double layered SLM allows for independent shaping of amplitude and phase. It consists of two thin nematic liquid crystals (LC) embedded between two Indium Tin Oxide (ITO) glass electrode plates. The LC is made of pixelated electrodes as shown in figure 3.6a. The SLM used in this work has 640 pixels. These pixels are oriented orthogonal to the chosen

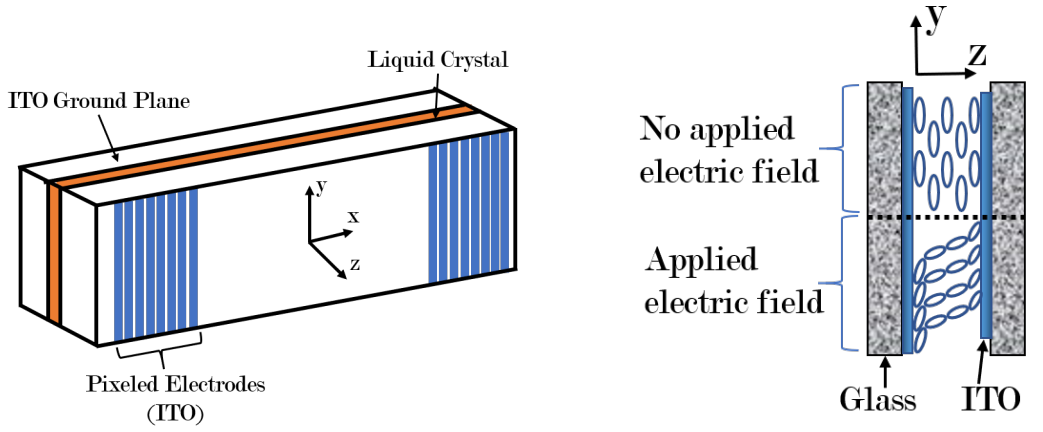

(a) Layout of SLM Liquid Crystal

(b) Liquid crystal pixel orientation

Figure 3.6: Mechanism for SLM liquid crystals for pulse shaping. Single layer SLM crystal display for pulse shaping 3.6a. Double layered SLMs have two layers aligned and bonded together. A close up of the orientation of pixels in ITO based on the application of an electric field or otherwise is shown in 3.6b.

polarization thereby creating an optical birefringence when no electric field is applied to the electrodes. In the presence of an applied electric field in the (z-) direction of propagation, these LC reorient along the z-direction hence reducing the birefringence as shown in figure 3.6b [132]. Proper calibration of each pixel on each layer of the SLM is required for effective pulse shaping due to the frequency dependent changes in the index of refraction which become significant for pulses with durations less than 30 fs [63]. SLM calibration maps each pixel to a specific wavelength within the SC pulse making it possible to address each spectral component independently. This calibration was performed experimentally by programming a slit on the SLM which scanned the pixel array and collected the spectrum while mapping it to the pixel number.

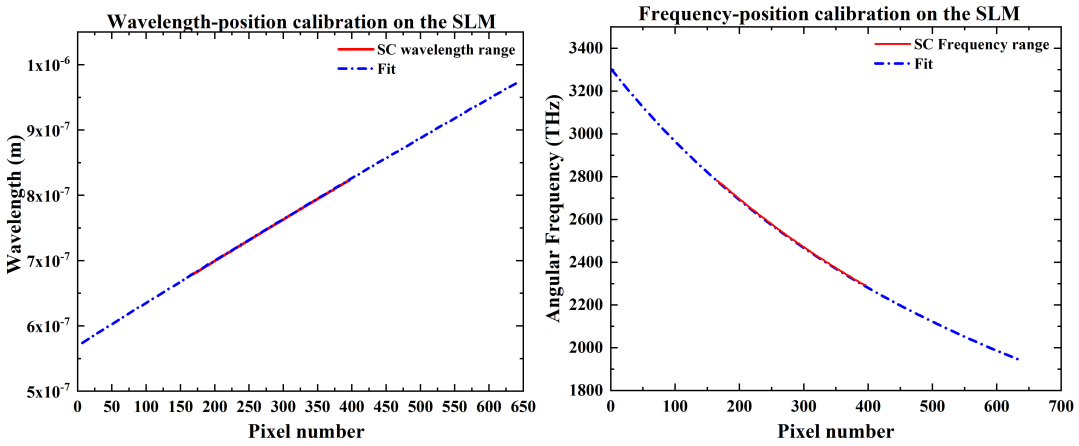

(a) Wavelength-position calibration of SLM **(b)** Angular frequency mapping of SLM calibration

Figure 3.7: Calibration of SLM mapping pixel number to wavelength range. The red line in figure 3.7a shows the wavelength-pixel range corresponding to the spectral range of the SC. The corresponding frequency data is given in figure 3.7b.

3.1.4 Imaging detection setup

The custom-built detection system was modelled in SOLIDWORKS® 2017 using CAD assembly parts from Thorlabs. As shown in figure 3.3, there are two possible beams that are used for imaging. The first is the beam originating directly from the Ti:Sapphire oscillator. This will be referred to as the "fundamental" beam for the rest of this work. The second beam is the spectrally broadened supercontinuum source. When using the fundamental beam, the beam is expanded using a beam expander (B.E.) with two achromatic lenses (Thorlabs AC254-050-B (f_1 = 50 mm) and AC254-200-B (f_2 = 200 mm)) arranged using the Keplerian geometry. This expanded the beam spot size from a diameter of ≈3 mm to a diameter of ≈10 mm. However when using the SC beam, this beam expander was removed since the SC beam was large enough (≈ 9 mm) to fill the back aperture of the microscope objective. Pulse propagation continues through a broadband achromatic

polarizer (Thorlabs LPVIS050-MP2) and is reflected by a dichroic mirror (Thorlabs DMSP650R) before being focused onto the sample through a microscope objective (Olympus plan fluorite/IR 60x/0.9 air). The microscope (imaging system) builds an image of a sample in a point by point manner, hence necessitating sample scanning. Scanning was carried out using computer controlled piezo stages (Newport AG-LS 25) using a custom-built LabView program while detection was carried out in the transmission geometry using a collector lens (Olympus plan achromat/10x/0.25 air). Appropriate band pass emission filters were used to block illumination light and transmit only required TPEF and SHG signals which were detected with a photomultiplier tube (PMT)(Hamamatsu H678003). The PMT was interfaced with a digital lock-in amplifier (Zurich Instrument, HF2LI) to amplify the signal recorded by the PMT while an optical chopper operating at 500 Hz was used to generate a reference signal for the lock-in amplifier. TPEF and SHG imaging were carried out using raster scanning. Motion control and data acquisition was carried out using a custom-built Labview program. In addition, bright field images were taken using a CMOS camera (Thorlabs DCC1545M, Monochrome sensor) with LED illumination provided by an in-house built source. The complete integrated imaging system is shown in figure 3.8. CAD models of the detection system are shown in figure 3.9 and the constructed system is shown in figure 3.10.

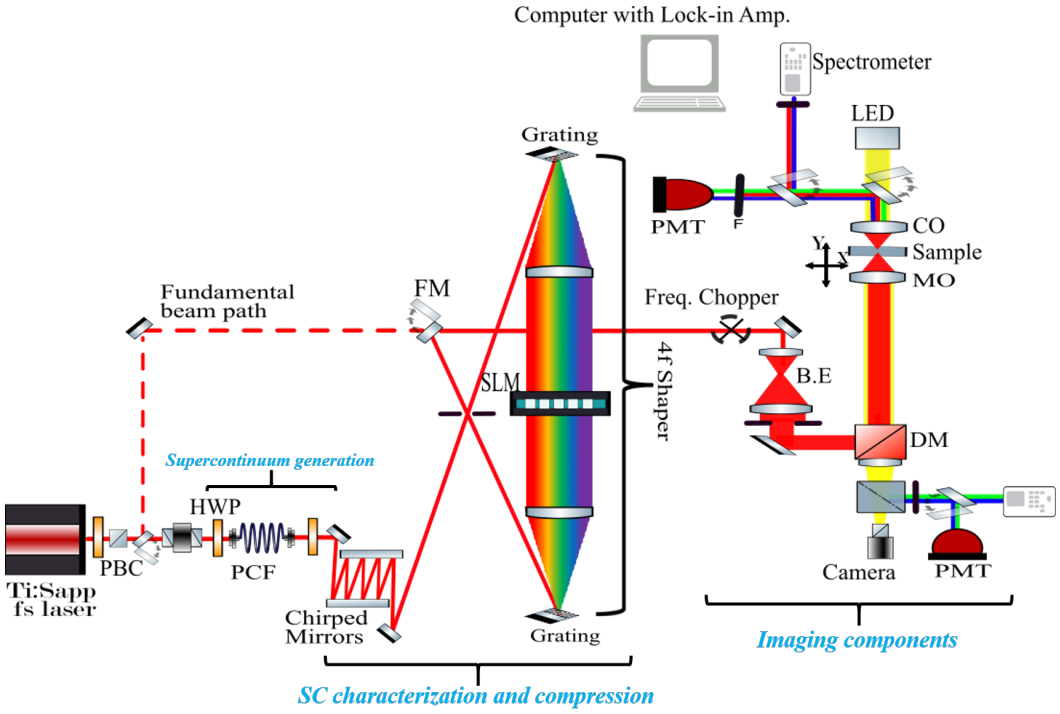

Figure 3.8: Integrated imaging setup showing the region of supercontinuum generation, pulse characterization and compression as well as imaging configuration. Abbreviations: PBC: polarization beamsplitter cube; HWP: halfwave plate, PCF: photonic crystal fibre; SLM: spatial light modulator; FM: flip mirror, B.E.: beam expander; DM: dichroic mirror: MO: microscope objective lens; CO: condenser lens, LED: while LED light source; PMT: photomultiplier tube.

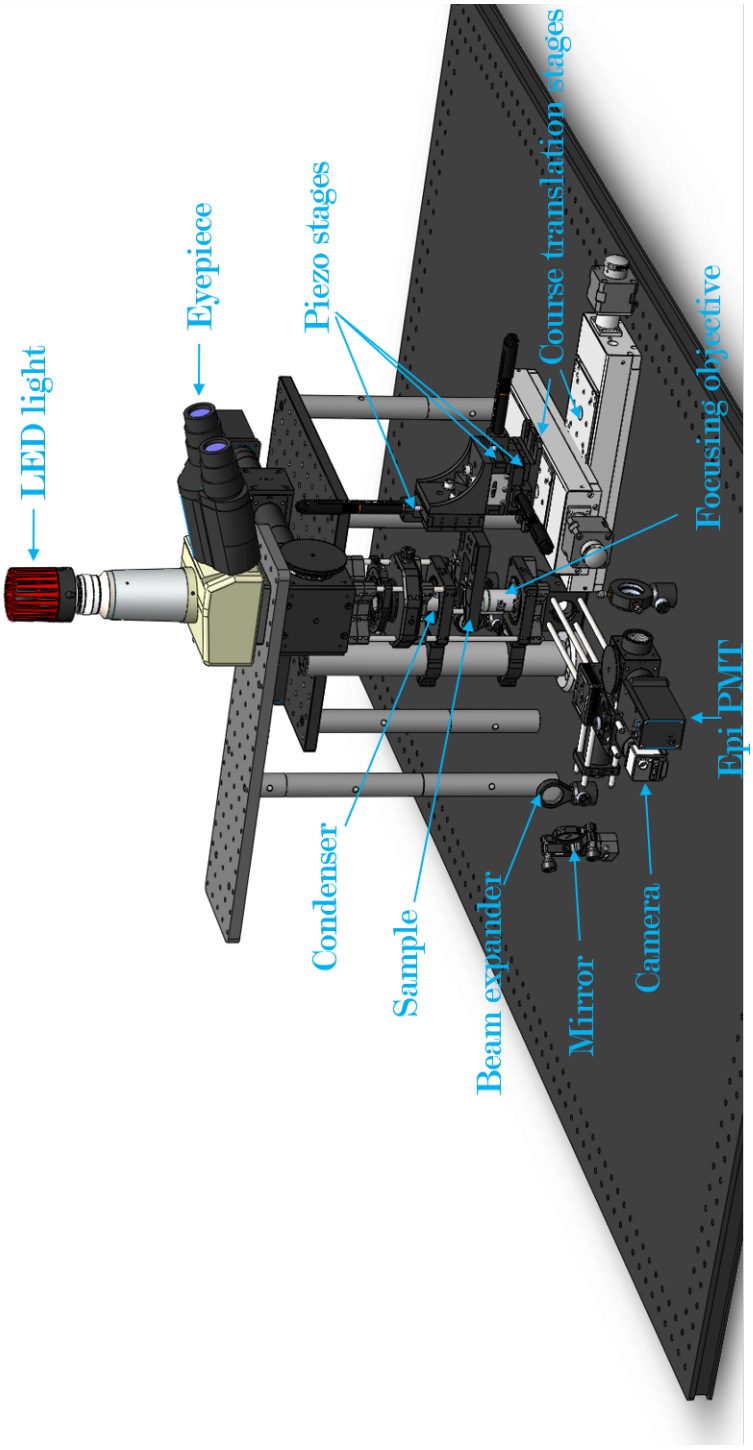

Figure 3.9: CAD model of the custom built detection configuration.

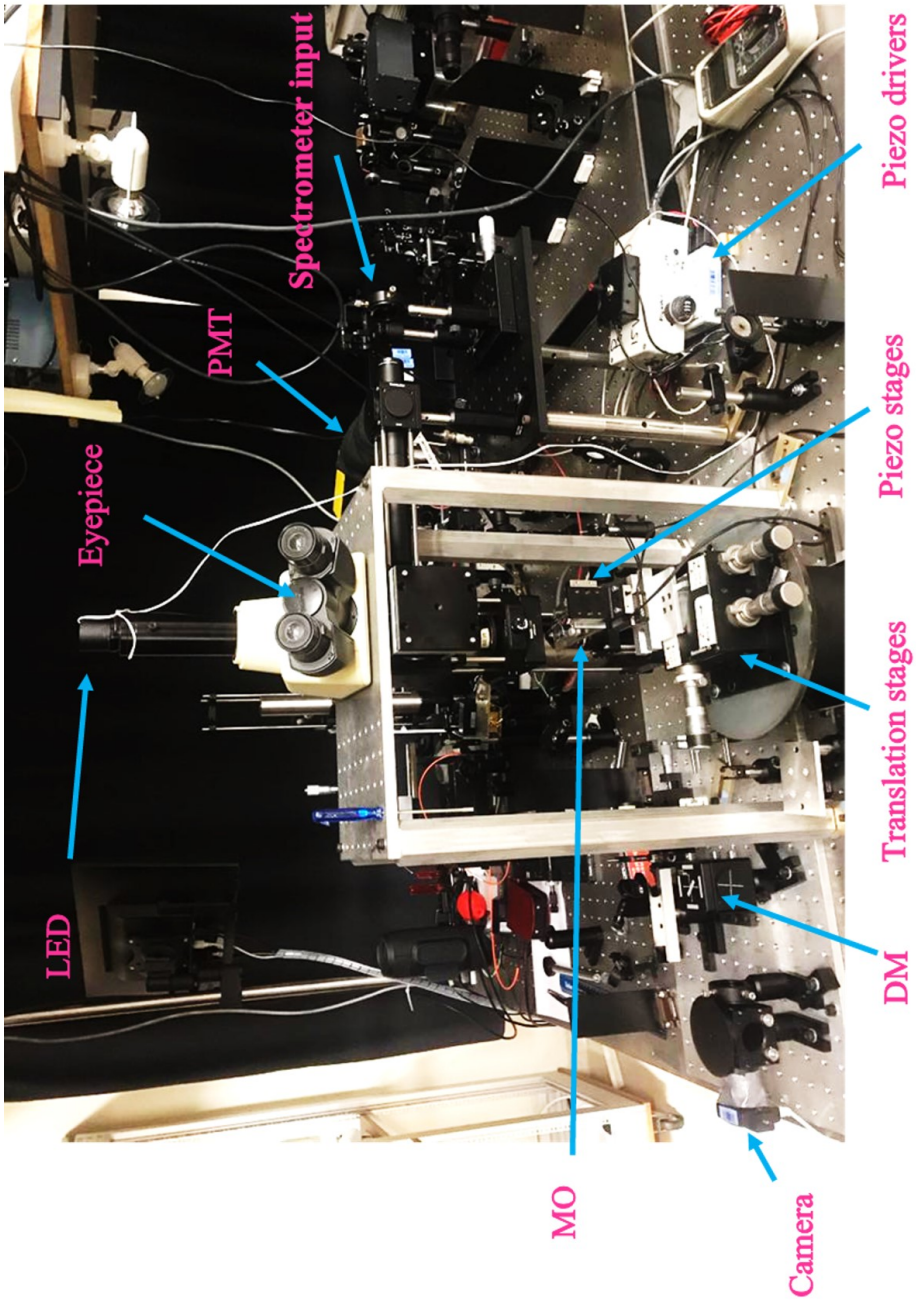

Figure 3.10: The constructed detection system in the laboratory showing some components. LED: LED light source, PMT: Photomultiplier tube, MO: microscope objective, DM: dichroic mirror. Camera is a CMOS monochrome camera

3.2 Spectral phase measurements

In this section, the two main phase measurement techniques employed ie MIIPS and i^{2}PIE will be discussed. It is important to note that pulses discussed in this section have already been pre-compressed by the chirped mirrors after undergoing 48 bounces with a compression of -175 fs^2 per bounce. Pulse compression involve the determination of the spectral phase distortions of the pulse in the focal plane of the microscope and compensating for this phase by applying a negative of the measured phase onto the SLM in order to compensate for the distortions.

For the spectral phase measurements, it should be noted that both MIIPS and i^{2}PIE characterizations were carried out using SHG signals generated from a 100 μm thick BBO crystal after focusing tightly with a 0.9 NA microscope objective. The signal was collected via a fibre coupled into a spectrometer interfaced with a custom-built Labview program.

3.2.1 MIIPS measurements

As stated in section 2.5.1.3, MIIPS works by adding a guess reference phase function to the phase of the input pulse and iteratively scanning over the laser pulse while determining the influence of the phase change on the SHG spectrum of the pulse. Experimentally, this is achieved by programming the reference phase function onto the SLM. This guess phase function now serves as a mask function which iteratively reduces or cancels phase distortions along the spectrum. This reference phase function (equation 2.5.9) of amplitude α and duration γ is scanned over a parameter δ to satisfy the Nyquist condition. The guess reference phase function parameters used as a guess function in this work include an amplitude (α) of 35 rads, duration (γ) of 20 fs and a δ value from 0 to 4π in 256 steps. These parameters were chosen based on extensive measurements previously performed on the setup where combinations of α and γ were examined to determine the best phase determination parameters for this particular setup [137]. The guess phase function is scanned across the input pulse and the spectrogram is recorded by collecting the SHG spectrum for different δ values. This spectrogram is what is referred to as a MIIPS trace. The phase values of each angular frequency (ω) component can be extracted from the MIIPS trace values of δ corresponding with ω where second harmonic is maximised. A successful spectral phase distortion measurement is indicated by recording SHG traces that are equidistant apart, parallel and approximately straight. A schematic representation of the MIIPS process is as illustrated in figure 2.7 in the previous chapter.

3.2.2 i^{2}PIE measurements

The i^{2}PIE phase measurement follows the schematic process outlined in figure 2.8. It starts with the initial guess of the input pulse. Here, a transform limited Gaussian pulse of duration 200 fs FWHM was assumed. The object field in the time domain $O_n(t)$ is created by applying this input pulse to a quadratic phase-only transfer function given by equation 2.5.19. The object function is multiplied by itself to form a product field in the time domain $G_n(t)$ whose Fourier transform into the frequency domain $G_n(\omega)$ yields a second harmonic spectrogram of intensity $S_n(\omega)$.

For example, figure 3.11 shows a measured i^{2}PIE spectrogram for $n = 51$ measured spectra. This spectrogram is used as the input for the i^{2}PIE phase reconstruction after an inverse Fourier transform into the time domain. For the ptychographic phase reconstructions, an $\alpha = 0.0001$ and $\beta = 0.3$ were used in equations 2.5.16 and 2.5.17. The reconstructed object field $O'_n(t)$ is Fourier transformed into the

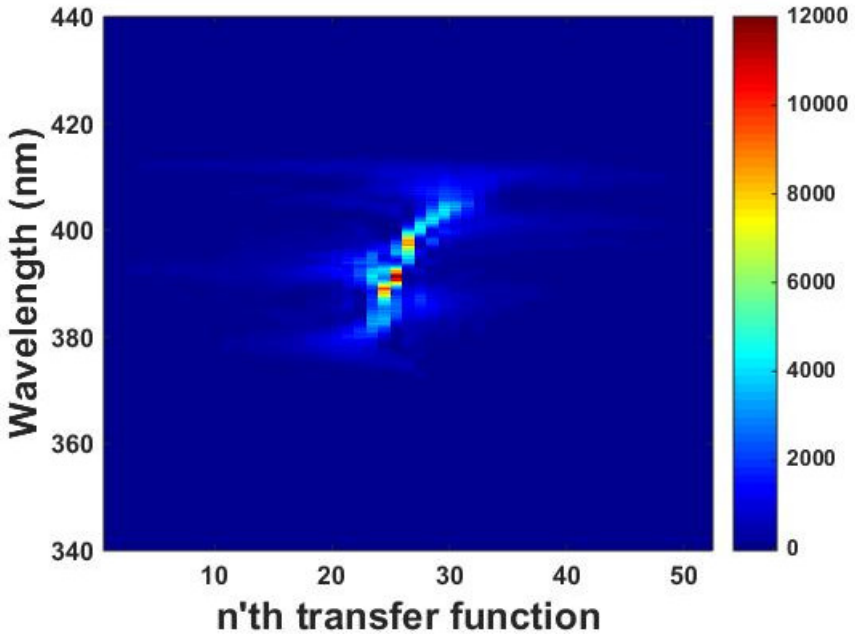

Figure 3.11: Spectrogram for i^{2}PIE phase reconstruction. Each n'th spectrum is recorded by applying each transfer function in equation 2.5.19 sequentially to the unknown object signal.

frequency domain and the electric field of the input pulse is updated.

Once the spectral phase for both MIIPS and i^{2}PIE have been determined, the negative value of the measured phase for each spectral component is applied to the SLM in the Fourier plane thus compensation for the phase distortions of the incoming pulse and generating compressed pulse.

3.3 Characterization of the imaging system

This section discusses the characterization of the imaging components. This includes the determination of the pulse durations achieved after compressing the pulse. It also discusses the steps employed in measuring the spot size of the compressed pulses in the focus of the microscope objective. The spatial resolutions and contrast determination procedures will also be discussed.

3.3.1 Determination of pulse duration

The pulse duration at the sample plane of the beam originating directly from the oscillator (fundamental beam) was estimated based on the documented GVDs of

the optical materials the beam traverses during propagation due to complications in employing other pulse measurements techniques at the sample plane. Pulse durations for the SC source were determined using a pulse shaper assisted frequency resolved autocorrelation. It requires the scanning of two identical replicas of the input pulse in a nonlinear medium and measuring the nonlinear response as a function of the delay between the replicas. These two replicas can be generated due to the ability of the pulse shaper (SLM) to control the spectral amplitude and/or phase. The delay scan can be achieved by either simultaneously shifting the carrier envelope and carrier phase or only shifting the envelope while keeping a fixed carrier phase [121]. The waveform of the two replicas is given by [121]

$$E(t) = E_0(t + \tau/2)e^{i\omega_0(t+\Gamma\tau/2)} + E_0(t - \tau/2)e^{i\omega_0(t-\Gamma\tau/2)} \tag{3.3.1}$$

where ω_0, τ, Γ represent the carrier frequency, temporal delay between the two replicas and the carrier phase shift respectively with $0 < \Gamma < 1$. For $\Gamma = 0$, there is no carrier phase change and for $\Gamma = 1$, there is a phase shift with the carrier envelope resulting in interference patterns.

For pixelated devices such as the SLM used in this work, waveform distortions can occur. For example, the gaps between two adjacent pixels allow some spectral components to pass through unmodulated which result in unwanted replicas at t=0 in the Fourier domain. Such distortions and effects are highlighted in [121]. To circumvent this problem, it is advisable to fix one replica at t=0 and scan the other replica. This approach was applied in this work and the spectral transfer function applied to the SLM under such condition is given by

$$M(\omega) = \frac{1}{2}[1 + e^{i[\omega-(1-\Gamma)\omega_0]\tau}] \tag{3.3.2}$$

Spectrally resolving the second harmonic signal generated from a BBO crystal produces a time-frequency spectrogram where the interference fringes can be adjusted by varying the Γ parameter. For example, figures 3.12a and 3.12b show measured time-frequency spectrograms for $\Gamma = 0$ and $\Gamma = 1$ respectively. The corresponding autocorrelation traces are shown in 3.12c and 3.12d. Figures 3.12a and 3.12c show an interference free signal while 3.12b and 3.12d mimic a frequency resolved autocorrelation signal as reported by [120–122]. Due to the non-interferometric nature of this technique and the collinear geometry employed, this technique will be referred to as non-interferometric collinear autocorrelation (NICA).

NICA provides a pulse duration comparable to durations measured with interferometric autocorrelation as can be seen in figure 3.12e where the autocorrelation traces of the NICA and collinear interferometric autocorrelation are superimposed and fitted with a Gaussian. The full width at half maximum (FWHM) of an autocorrelation $\Delta\tau_A$ is related to the FWHM of the pulse $\Delta\tau_p$ by [115]:

$$\Delta\tau_A = \sqrt{2}\Delta\tau_p \tag{3.3.3}$$

Applying equation 3.3.3 to the fits in figure 3.12 as an example shows an average duration of (18.3±1.0) fs for NICA trace and (17.6±1.0) fs interferometric technique. This clearly indicates that both techniques offer same results, however NICA requires

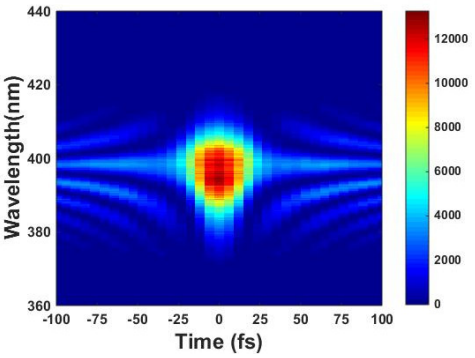

(a) Spectrogram for non-interferometric autocorrelation

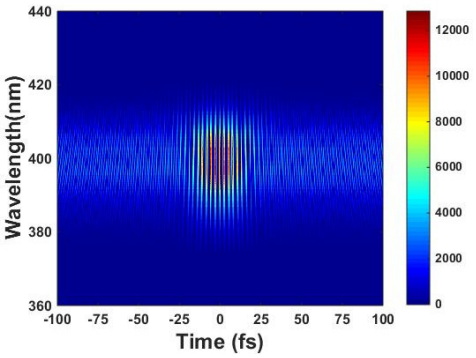

(b) Spectrogram for interferometric autocorrelation

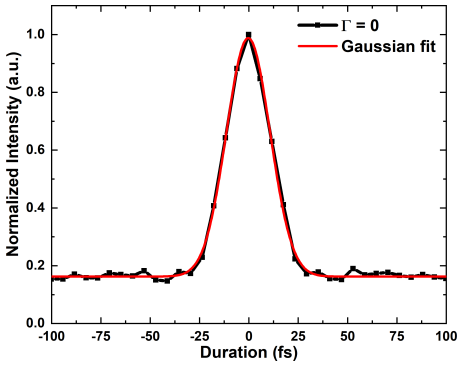

(c) Non-interferometric autocorrelation trace

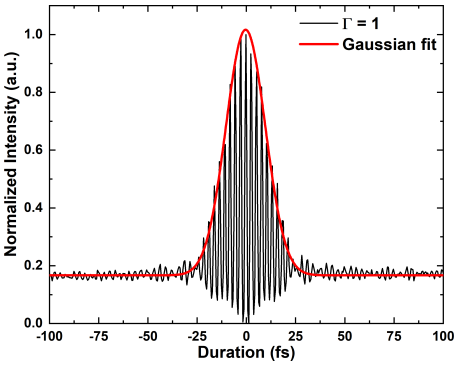

(d) Interferometric autocorrelation trace

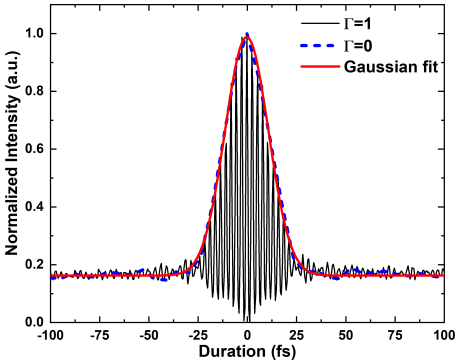

(e) Superposition of interferometric and non-interferometric autocorrelation traces

Figure 3.12: Measured time frequency distribution spectrograms for (a) $\Gamma = 0$, (b) $\Gamma = 1$ and the corresponding autocorrelation traces shown in (c) $\Gamma = 0$, (d) $\Gamma = 1$. Figures (c) and (d) are superimposed in (e). Figures (c),(d) and (e) are fitted with a Gaussian to indicate the temporal duration.

fewer data points. This greatly reduces the data acquisition and computational processing time.

NICA was chosen over interferometric autocorrelation techniques because of the simplicity in its implementation in collinear geometry as well as the need to ensure complete modulation of the entire SC pulse.

3.3.2 Spot size determination

The beam spot size in the focus of the microscope was determined by adapting a technique analogous to the open aperture z-scan technique which is a method usually used to measure the nonlinear index of refraction and absorption coefficient of materials [138, 139]. By moving a nonlinear crystal (urea crystal in our case) through a tightly focused Gaussian beam, the second harmonic intensity (I_{SH}) generated scales with the square of the incident intensity (I) i.e. $I \propto I_{SH}^2$. The interaction

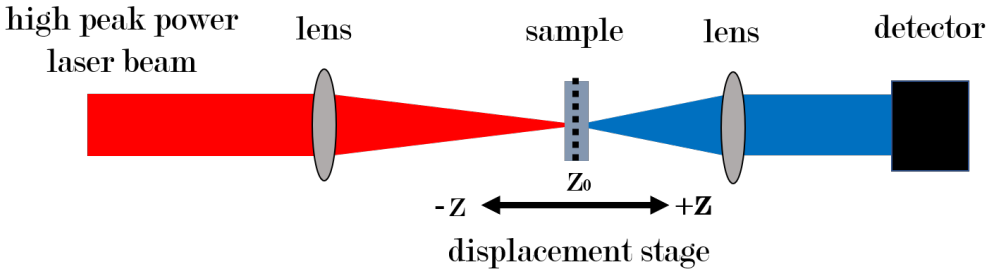

Figure 3.13: z-scan technique for determining the Rayleigh lengths for the focused laser beam. The signal response recorded on the detector is dependent on the position of the sample in the focus of the excitation lens.

between the nonlinear crystal and the laser intensity at any (z) position relative to the focus ($z = 0$) results in different signal intensity generated. Maximum signal generation occurs when sample is in the focus as this correlates with the highest incident intensity. Thus the signal measured from this analogous z-scan technique can be treated as a Gaussian profile.

For a Gaussian beam of waist radius w propagating in the $+z$ direction from the beam waist, the intensity profile has the form [140]

$$I(x, y, z) \sim I_0 \exp\left(\frac{-2(x^2 + y^2)}{w^2}\right) \tag{3.3.4}$$

where I_0 is the on-axis intensity ie $I_0 = I(0, 0)$. The beam radius $w(z)$ is related to the z-position by the relation

$$w(z)^2 = w_0^2\left(1 + \frac{z^2}{Z_0^2}\right) \tag{3.3.5}$$

where $w_0 = w(z = 0)$ and Z_0 is the Rayleigh or diffraction length of the beam. Z_0 is also related to the laser wavelength (λ) and the radius of the beam at its waist w_0 by

$$Z_0 = \pi w_0^2/\lambda \tag{3.3.6}$$

and $\lambda = 2\pi c/w_0$ with c being the speed of light in vacuum. The radius of curvature of the wavefront at position z is given by

$$R(z) = z\left(1 + \frac{Z_0^2}{z^2}\right) \tag{3.3.7}$$

For a Gaussian beam, integrating equation 3.3.4 gives the fundamental power, P_w, incident on the sample and is given by

$$P_w = I_0 \frac{\pi w^2}{2} \tag{3.3.8}$$

The generated second harmonic intensity is related to the fundamental intensity by

$$I_{2w}(x, y) = \eta I_0^2 \exp\left(\frac{-4(x^2 + y^2)}{w^2}\right) \tag{3.3.9}$$

with η being the second order NL conversion efficiency constant. Integrating over $I_{2w}(x, y)$ gives the power of the generated second harmonic

$$P_{2w} = \eta I_0^2 \frac{\pi w^2}{4} \tag{3.3.10}$$

Comparing equations 3.3.8 and 3.3.10 implies

$$P_{2w} = \frac{\eta P_w^2}{\pi w^2} \propto \frac{1}{w^2} \tag{3.3.11}$$

Inserting equation 3.3.5 into equation 3.3.11 gives

$$P_{2w} = \frac{\eta P_w^2}{\pi w_0^2} . \frac{1}{1 + \frac{z^2}{Z_0^2}} \tag{3.3.12}$$

Setting $K = \eta P_w^2/\pi w_0^2$ implies

$$P_{2w} = \frac{K}{1 + (\frac{z}{Z_0})^2} \tag{3.3.13}$$

Thus the SHG signal gives a peak function governed by equation 3.3.13 from which the Rayleigh length can be extracted and from equation 3.3.6, the beam radius and spot size can be determined.

Second harmonic data for each sample position relative to Z_0 was recorded for the fundamental beam as well as the MIIPS and I^{2}PIE phase compensated pulses by focusing into a 100 μm thick BBO crystal. The signal generated was recorded by a Hamamatsu PMT interfaced with a lock-in amplifier (Zurich Instrument). The measured intensity responses were fitted with the peak function in equation 3.3.13 with K and Z_0 as fit parameters.

3.3.3 Spatial resolution and contrast measurements

Lateral resolution (resolution in the direction perpendicular to the beam propagation) of the system was determined using recrystallized urea crystals through the z-scan method discussed in section 3.3.2. It should be noted that the scope of this work is limited to 2D images and as a result, axial resolution measurements were not carried out. The spot size obtained is an indication of the smallest possible beam diameter in the focus of the microscope objective. Minimum resolvable distance was estimated by measuring the fluorescence intensity across fluorescent microbeads stained with "Light yellow" fluorophores (FP-2045-2, Spherotech) with 2.00±0.03 μm average size and 405/450 nm peak absorption/emission wavelengths. Refer to figure 3.14 for micrograph of beads and measured fluorescence spectrum recorded with an in-house developed portable fibre-probe fluorescence detection system [141]. Beads were sonicated in methanol and spin coated onto a microscope cover slide for fluorescence measurements. It should be noted that these beads were only used for system calibration purposes due to their well defined dimensions.

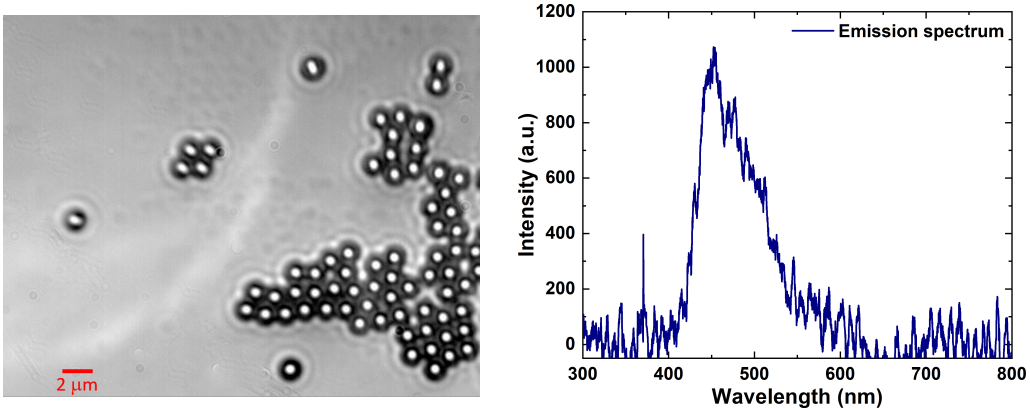

(a) Micrograph of FP-2045-2 fluorescence beads

(b) Emission spectrum of FP-2045-2 fluorescence beads

Figure 3.14: Micrograph of fluorescent beads imaged through a 60X microscope objective(a): image scale 2 μm and fluorescence emission spectrum of fluorescent bead (b).

Chapter 4

Experimental Results

This chapter showcases the various measurements carried out throughout the course of this work. It focuses on exploring the unique features of the nonlinear microscopy system constructed. It presents and discusses the spectral features of the polarization maintaining PCF used. This chapter also presents a comparative analysis of the new i^{2}PIE phase measurement technique with the commonly used MIIPS technique. The characteristic features of each technique and how they contribute to the generation of compressed pulses which can be used to generate high peak intensity pulses for nonlinear microscopy will also be presented and discussed. For direct comparative analysis of results, all measurements were conducted under same conditions. Where conditions differ, a vivid clarification will be given accordingly.

4.1 Laser characteristics (fundamental pulse)

The spectral output from the Spectra-Physics Tsunami laser was measured with a fibre coupled spectrometer. The measured spectral intensity is shown in figure 4.1

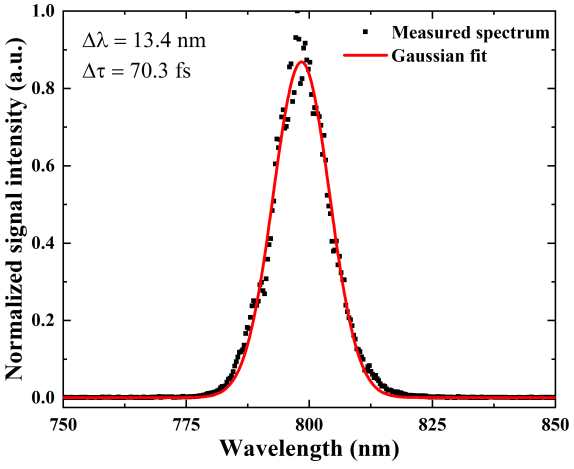

Figure 4.1: Spectral intensity profile of the Tsunami laser (black dots) with a Gaussian fit (line). As stated in previous chapters, this will be referred to as fundamental pulse throughout this work.

where the peak wavelength $\lambda_0 = 800 \pm 1$ nm. The measured spectral full width at half maximum (FWHM) bandwidth is $\Delta\lambda = 13.4 \pm 1$ nm. This corresponds to a frequency bandwidth ($\Delta\nu$) of 6.27 THz from the relation $\Delta\nu = \frac{c\Delta\lambda}{\lambda^2}$. For a transform limited (TL) Gaussian pulse, the spectral bandwidth ($\Delta\nu$) and temporal duration ($\Delta\tau$) are related by $\Delta\nu\Delta\tau \approx 0.441$. Therefore for a given TL Gaussian pulse, the minimum time duration is related to the wavelength by

$$\Delta\tau \approx \frac{0.441\lambda^2}{c\Delta\lambda} \tag{4.1.1}$$

Assuming a TL Gaussian pulse, the calculated pulse duration of the fundamental beam at the exit of the oscillator is 70.3 fs. However, previous pulse duration measurements taken in our lab shows a pulse duration of 80 fs [137, 142].

4.2 Supercontinuum generation

In general, when working with PCFs, it is essential to characterise and optimise the polarization of the SC spectrum exiting the fibre. This section considers the measurement and characterization of the induced birefringence within the PCF due to structural symmetry breaks in the fibre drawing processes. Procedures to overcome this intrinsic birefringence is also discussed. The dependence of the SC generation on input power will also be considered for both the new experimental polarization maintaining PCF provided by NKT photonics and a commercial non-polarization maintaining PCF.

4.2.1 Polarization contrast measurements in PCF

The setup for the SC characterization of both the polarization maintaining (PM-) and non polarization maintaining (non-PM-) PCF is shown in figure 3.1. As stated in section 3.1, the incoming laser before the HWP is horizontally polarized. The coupling efficiency into the PCF was between 58-68%. In order to improve the purity of the exit polarization, the pulse has to be coupled into the fibre at an angle parallel to a specific axis. As a result of the twists during the drawing process, the fibre output will be rotated from the horizontally polarized beam. The polarization of the output SC pulse is rotated by a second HWP (acts as an analyser) relative to a horizontally oriented polarizer in order to obtain maximum transmission of horizontally polarized light. By recording the power transmitted for the horizontal and vertical polarizations, the ratio of the optical powers in the two polarizations can be determined. This ratio is what is mostly referred to as the extinction ratio. For this work, this extinction ratio (ER) is the percentage power in the perpendicular axis ($Power_\perp$) to the sum of the powers in both axes i.e.

$$ER = \frac{Power_\perp}{Power_\parallel + Power_\perp} \times 100\% \tag{4.2.1}$$

where $Power_\parallel$ is the power transmitted in the principal axis which is the axis parallel to the horizontally polarized beam. The output beam from the fibre consists of transmissions in both axes and is a superposition of two cosine-squared graphs shifted

by 90°. Therefore, transmission in each axis was determined by fitting the measured transmitted powers with the model of the Malus's law[1]:

$$a\left[\cos\left(\frac{x\pi}{90}\right)\right]^2 + b\left[\cos\left(\frac{x\pi}{90}+\frac{\pi}{2}\right)\right]^2 \tag{4.2.2}$$

where a, b correspond to the transmission in orthogonal polarizations.

Figure 4.2a shows the power measured at the output of the vertical polarizer for input polarization angles of 0°, 30° and 90°. The analyser orientation angles are

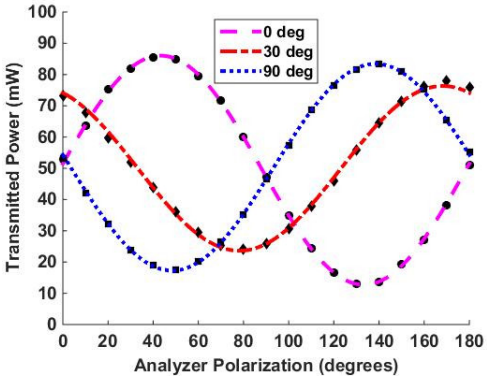

(a) Variations in power transmission with polarizer-analyzer orientations

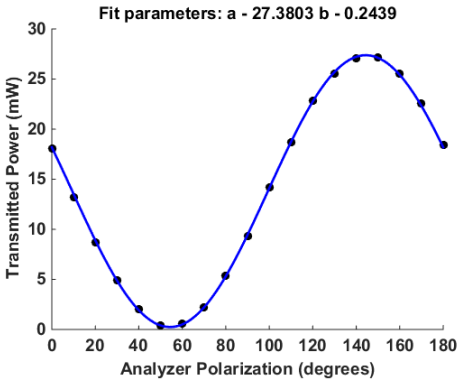

(b) Estimation of maximum and minimum power transmission for a fixed input polarization of 104°

Figure 4.2: Determination of polarization transmission properties for all PCFs: (a) depicts how the transmitted power depends on the input polarization angle. The fit parameters extracted based on Malus's law is shown in (b) with a representing the power in the parallel axis and b representing the power in the orthogonal axis.

shown as the x-axis. The measured data points are the black discrete points and the fit from Malus's law (expression 4.2.2) are shown in coloured line. As expected, there is the transfer of power from one axis to the orthogonal axis for a 90° rotation of the input polarization as seen by the measured powers for 0° and 90° input angles. In between the orthogonal axes, the transmission profile varies as seen in the 30° plot. For the rotation of the output analyser, the angle difference between the minimum and maximum transmission corresponds to a 90° rotation. For example, considering the 90° input polarization, the minimum transmission occurred at an analyser orientation of 50° which implies the analyser was oriented perpendicular to the horizontal polariser. The maximum transmission occurred at 140° when the PCF output polarization was rotated to be parallel to the polariser.

The ER was calculated for each input polarization orientation. The smaller the ER, the more pure the polarization is in the specific axis. For example, figure 4.2b shows a $\cos^2$ graph for an input polarization of 104°. From the fit parameters $a = 27.38$

[1]Malus's law states that: "For a beam of plane-polarized light, the intensity after transmission through a rotatable polarizer varies as the square of the cosine of the angle through which the polarizer is rotated from the position that give maximum intensity"

and $b = 0.24$ on the graph, the ER is found to be 0.87% with maximum transmission at an analyser orientation of 145°. Considering figure 4.2a, the minimum/maximum parameters with the calculated ER are shown in table 4.1. The input HWP angle

Table 4.1: Extinction ratio table

Input pol.	Min. power (mW)	Max. power (mW)	ER (%)	Max. HWP2 angle
0°	12.74	86.03	12.90	40°
30°	23.62	76.34	23.63	170°
90°	17.26	83.42	17.14	140°

which results in the least ER is chosen as the input angle and the analyser orientation with the highest transmitted power serves as the output HWP angle. Therefore considering table 4.1, the input/output polarization angles of 0°/40° offer the best ER. For an input power of 100 mW, the supercontinuum spectrum captured as function of analyser orientation for figure 4.2b is shown in figure 4.3. It is observed

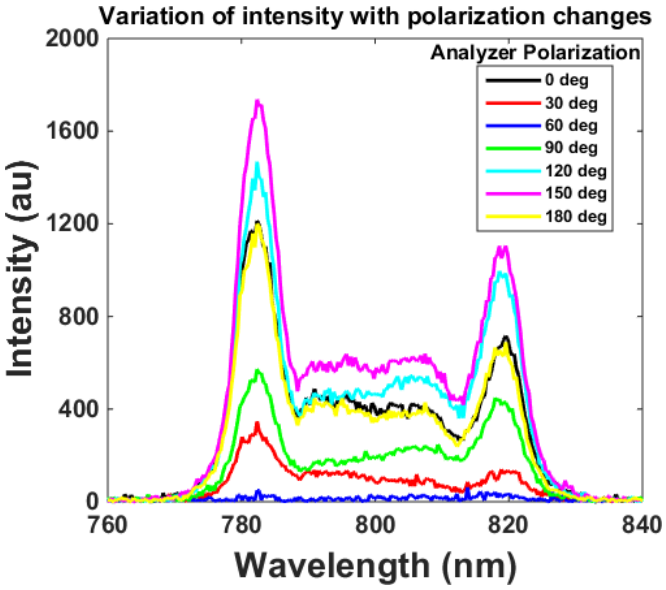

Figure 4.3: Transmitted spectral profiles recorded with varying analyser polarization for a fixed input polarization. The spectral profiles plotted here are the measured data corresponding to analyser orientations in figure 4.2b.

that for a fixed input power, the intensity of the spectral output of the PCF varies with the analyser orientation relative to the horizontal polarizer. At lower powers, the spectral profiles look the same for a particular polarization orientation for both polarization and non-polarization PCFs.

4.2.2 Dependence of supercontinuum spectrum on input power

We investigated the spectral output of two different types of ANDi-PCFs as a function of input power. The two PCFs types are the polarization maintaining (PM-) and non- polarization maintaining (non-PM-) PCFs with features discussed in section 2.4.1. In order to do this, the halfwave plates were set at their optimal orientations. Figures 4.4a and 4.4b show the SC spectra generated by non-PM-PCF and PM-PCF respectively. They clearly show an increase in spectral bandwidth with increasing input power. This can mainly be attributed to greater nonlinear effects being induced

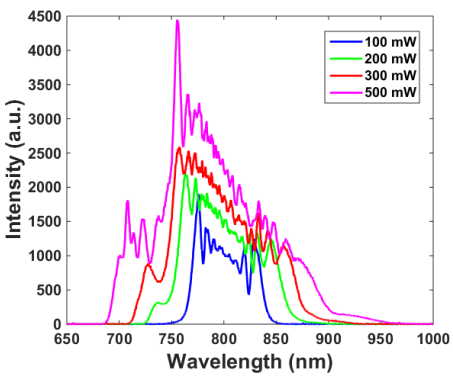

(a) Power dependence spectra for non-PM-PCF

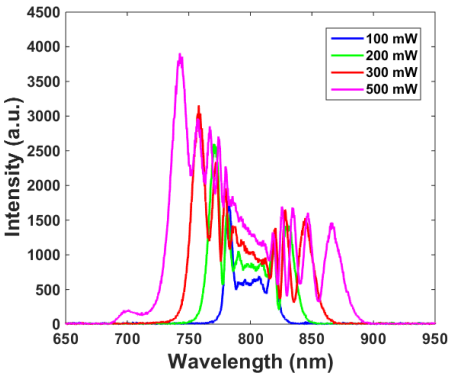

(b) Power dependance spectra for PM-PCF

Figure 4.4: SC generation with varying input power for non-PM-PCF and PM-PCF. The higher the coupled input power, the broader the SC pulse as a result of greater nonlinear effects induced.

in the fibre resulting from higher intensities within the fibres. The broader SC bandwidth provides the possibility for dynamic control of the pulse length and ultimately the peak intensities generated after suitable compression. However at higher powers (500 mW), the spectral profile changes considerably in the non-PM-PCF while the shape of the PM-PCF remains the same. These results correspond to previously reported works on nonlinear polarization dynamics in weakly birefringent PCFs where it was determined that at higher coupling powers, depolarization is known to occur over time where power is gradually decoupled into the orthogonal mode thus distorting the spectrotemporal field of the SC pulse along the fibre length[111]. This spectral profile change will have a corresponding effect in the temporal profile thus affecting the coherent control of the pulse. The strong birefringence induced in the PM-PCF is seen to provide high confinement along the principal axis at higher coupling powers thereby eliminating this scrambling of the polarization state of the supercontinuum.

A measure of the transfer of power between axes of each fibre was determined by recording the SC power transmitted along the principal (parallel) and orthogonal (perpendicular) axes over time as shown in figure 4.5. Figures 4.5a and 4.5b show the power recorded for a non-polarization maintaining PCF at the start of measurement and 60 minutes later with 700 mW average coupling power. Figures 4.5c and 4.5d

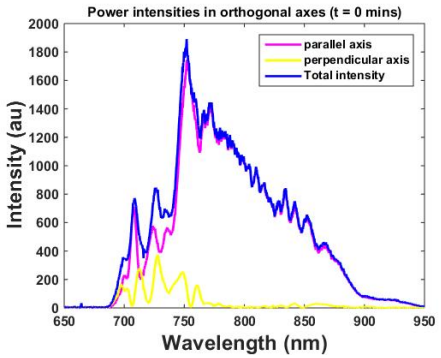

(a) Pump-time-dependent spectra for non PM-PCF at onset of pumping

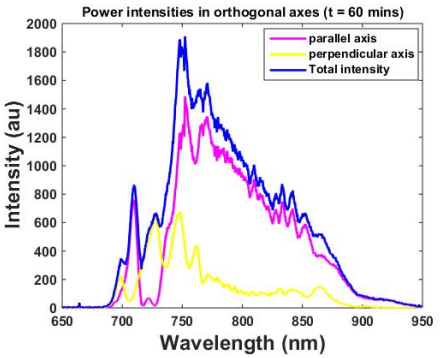

(b) Pump-time-dependent spectra for non PM-PCF after 60 minutes of pumping

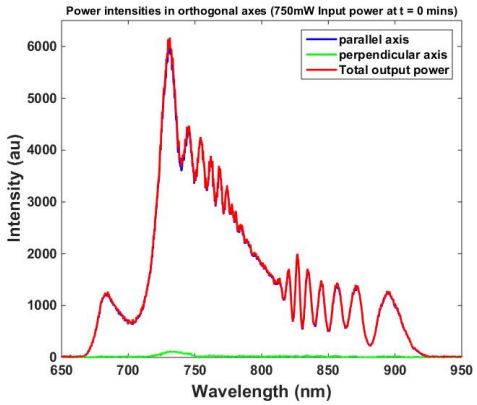

(c) Pump-time-dependent spectra for PM-PCF at onset of pumping

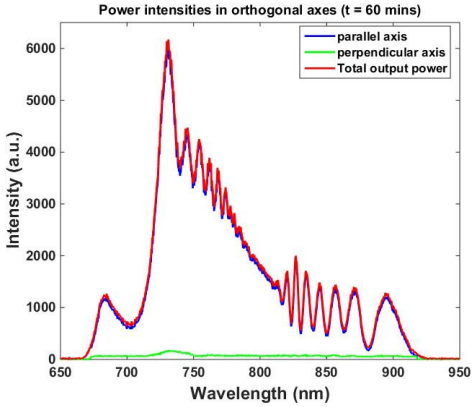

(d) Pump-time-dependent spectra for PM-PCF after 60 minutes of pumping

Figure 4.5: Power intensities recorded in orthogonal axes for non-PM-PCF and PM-PCFs at onset of measurement i.e. time t = 0: figures 4.5a and 4.5c and after 60 minutes of pumping: figures 4.5b and 4.5d respectively.

show the same measurements for a PM-PCF under similar conditions. Depolarization is seen to occur in the non-PM-PCF even at the onset due to the high power and is seen to increase over time. For the same time interval, the PM-PCF shows a more stable SC profile making them a more suitable choice over the weakly birefringent non-PM-PCF for applications that require higher SC stability.

In view of the high polarization confinement and its corresponding higher stability of the polarization maintaining fibre over the non-PM counterpart, the PM-PCF was preferred. As such, for the remaining sections, only the polarization maintaining fibre was used. Hence, subsequent reference to PCF only implies a polarization maintaining fibre.

4.3 Pulse characterisation and compression

In this section, we consider the experimental data recorded throughout the pulse characterization and compression. As discussed previously, two phase measurement techniques were employed in this work: MIIPS which is well established and is regularly applied in microscopy [59, 65, 66, 143] and a novel i^{2}PIE technique recently developed in our laboratory [70]. The pump power of 200-300 mW was chosen for this investigation due to our confidence in the fact that the SC phase can be well compensated for by the chirped mirrors and 4f shaper at this generated supercontinuum bandwidth as well as the greater possibility to generate effective phase matching in the BBO with the spectral bandwidth generated by pumping at this average power range. The SC spectrum recorded at 200 mW input power is shown in figure 4.6a with a spectrum spanning from approximately 710 - 850 nm. The spectral bandwidth of the SC spectrum was measured at 5% of the maximum intensity. The bandwidth for figure 4.6a was therefore measured to be approximately 110±1 nm with the bandwidth measured between the arrowed regions in figure 4.6a. Its corresponding calculated Fourier limited temporal pulse is plotted in figure 4.6b with a FWHM of 11±1 fs. As can be seen from figure 4.6a, the SC spectrum spans

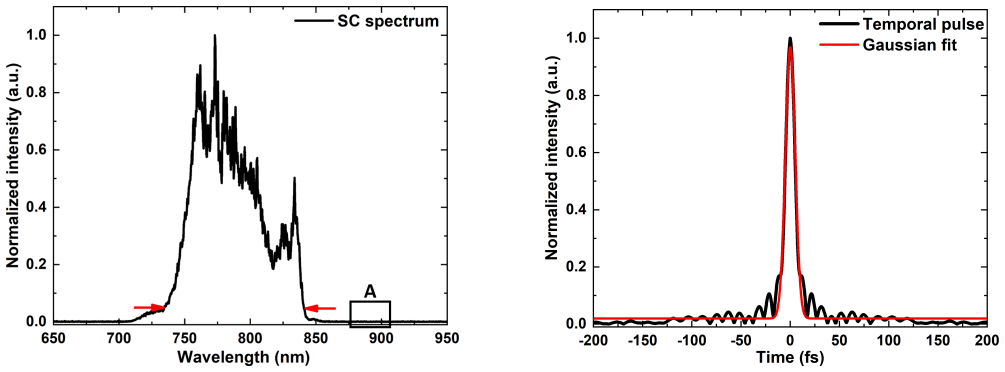

(a) Spectrum of PCF output for pulse characterization

(b) Temporal pulse of PCF output

Figure 4.6: Spectral and temporal profiles of SC generated. (a) Supercontinuum spectrum of PCF output with 200 mW input power at a coupling efficiency of 65%. Region 'A' defines the noise region for the signal. (b) represents the corresponding calculated pulse in time.

a specific wavelength range. However, the spectrometer records data for a broader spectral range between 200 -1300 nm. In order to determine if the measured intensity is attributed to SC generation, we estimated an intensity threshold for the detector noise. This noise was estimated by determining the standard deviation (SD) of the region outside the SC spectrum (eg. region "A" in figure 4.6a). The background noise was determined to be approximately 0.2% of the maximum intensity recorded for a SC generated with 200 mW input power. Therefore, any intensity above three times the noise (3×SD) was attributed to SC generation.

The phase of the generated SC pulse at the output of the PCF is however unknown. The SC was therefore sent into the 4f shaper consisting of a spatial light modulator

to quantitatively measure the phase of the pulse by either applying MIIPS or the new i^{2}PIE technique. Section 4.3.1 presents and discusses the phase measurement achieved by implementing MIIPS while section 4.3.2 focuses on the implementation of the novel i^{2}PIE technique.

As stated previously, the pulse reaching the 4f shaper has been pre-compressed with 48 bounces between a pair of chirped mirrors with -175 fs^2 GDD compensation per bounce. With GDD being a second order dispersion (SOD) parameter, it implies that the pulse exiting the chirped mirror has most of its SOD compensated. Furthermore, the pre-compression reduces the "range" of phase to be corrected by 4f shaper, so that the difference between adjacent pixels on the SLM is less thereby increasing the compression efficiency of the 4f shaper. However, the chirped mirrors cannot compensate for phase distortions attributed to higher order dispersions (HOD) i.e. third order dispersions and above. Furthermore, pulse propagating through the microscope objective also adds some amount of second order phase distortions. Since the measurement is done at the plane of the object, MIIPS and i^{2}PIE are therefore used to measure and compensate for these added second and other higher order phase distortions.

4.3.1 MIIPS phase determination

As previously stated in section 3.2.1, MIIPS works by applying a reference phase function to the SLM and iteratively scanning over the laser pulse while determining the influence of the phase change on the SHG spectrum of the pulse. The phase recorded can be extracted from this measured SHG spectrum (from equation 2.5.12). The phase on the SLM is then updated by applying the negative of the measured phase before the next iteration. The phase on the pulse converges after a number of iterations when the phase distortion is close to zero.

In determining the phase extraction from MIIPS, let us consider figure 4.7 as an example. The graphs presented here are representative of the numerous measurements taken. From equation 2.5.9, $f(\omega) = \alpha\cos(\gamma(\omega - \omega_0) - \delta)$, an amplitude ($\alpha$) of 35 rads and a pulse duration scaling parameter (γ) of 20 fs were used as reference phase function parameters and scanned over a parameter δ. Figure 4.7a shows the second harmonic intensity recorded after 10 iterations as a function of wavelength (λ) and reference phase position (δ) over a 4π range. This trace is a representation of where the SHG signal is maximised for each frequency component. It can be noticed that the trace depicts parallel and equidistant features which is characteristic of transform limited pulses and is consistent with previously documented MIIPS traces [63, 124].

Employing an iterative scan while correcting the recorded group delay dispersion (GDD) between successive iterations until the residual GDD falls below a certain threshold is the best way of improving measurement accuracy for MIIPS [64, 124]. Figure 4.7b shows the error in the residual phase recorded after each iteration. A small error signifies convergence in the residual phase measured for each iteration. Addition of a negative value of the retrieved phase (from equation 2.5.12) to the pulse after each iteration using the pulse shaper reduces the phase distortions thereby

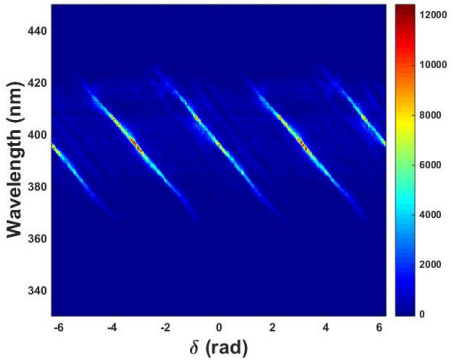

(a) SHG intensity recorded with MIIPS showing SHG traces

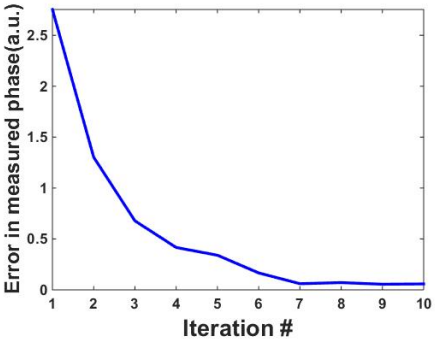

(b) Error in residual measured phase after each MIIPS iteration

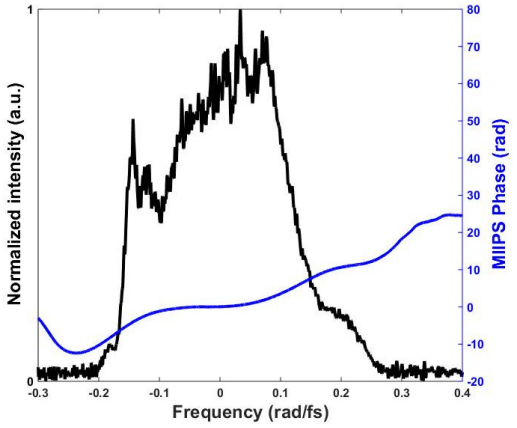

(c) SC phase retrieved with MIIPS

Figure 4.7: Pulse characterization with MIIPS. Figure 4.7a shows the SHG trace recorded after the 10th iteration plotted as a function of wavelength and reference phase position. The error in the residual phase after each iteration is plotted in (b) showing the convergence in the error per iteration. The measured phase after the last iteration is shown by the blue line in (c) plotted over the SC spectrum (black line). The matlab code for analysis is shown in appendix C.1.

resulting in lower residual GDD recorded per iteration. From figure 4.7b, the residual GDD converges close to zero after 7 iterations indicating a convergence in the phase characterization has been reached. The retrieved phase after the 10th iteration is plotted along the SC spectrum in figure 4.7c where the SC intensity and phase are plotted centred around $\omega - \omega_0$ with ω_0 being the central frequency. The phase is recorded based on the resolution of the spectrometer hence only the retrieved phase for non-zero spectral components is of interest. That is phase recorded for spectral components with intensities three times the standard deviation of the spectrometer noise level. It should be noted that this phase is only a measure of the residual phase on the pulse before the last iterative measurement and not the exact phase of the pulse. Therefore, the exact phase left on the pulse can not be directly measured.

4.3.2 i²PIE phase determination

From section 3.2.2, i²PIE also works by applying a known spectral phase-only transfer function to the pulse and recording the SHG spectra. The phase and amplitude of the pulse can be extracted from this single set of data. The typical spectrogram recorded using i²PIE is presented in figure 3.11 and reproduced in figure 4.8a. This intensity spectrogram was the input for the time-domain PIE (i²PIE) algorithm and was used to sequentially update the guess spectrum for each time delay. The reconstruction process is detailed in [70, 126]. The algorithm produces a reconstructed temporal object pulse. The spectral phase recorded, upon a Fourier transform of this reconstructed temporal pulse, is shown in figure 4.8b. Again, only the phase corresponding to the region of significant spectral intensity in the SC pulse is of relevance.

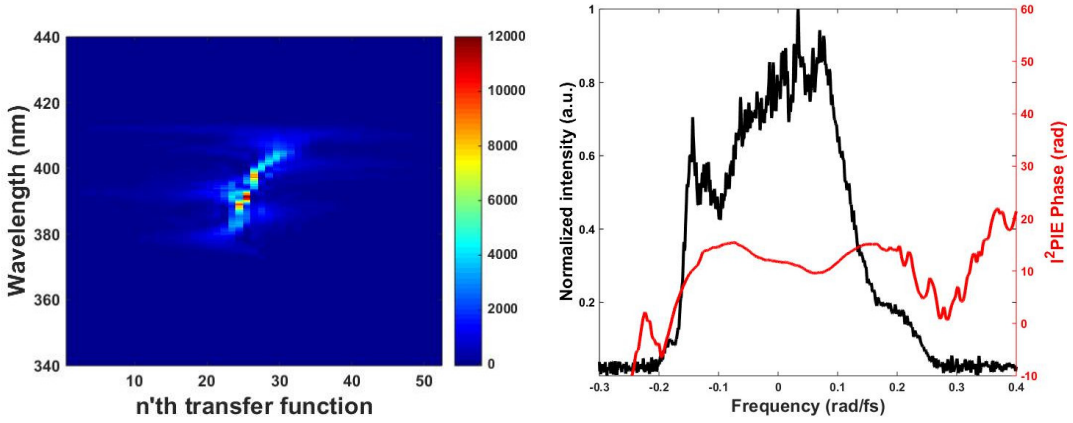

(a) Spectrogram for i²PIE phase reconstruction

(b) SC phase measured with i²PIE

Figure 4.8: Spectrogram and phase measured with i²PIE. (a) is the same as figure 3.11 and recorded as described in section 3.2.2. (b) Phase measured with the i²PIE characterization technique (shown in red) over the SC pulse (black).

In order to compare the phase measurement abilities of MIIPS and i²PIE on equal terms, it is imperative to compare them on the same level. The next section presents comparative analyses of the two pulse shaper assisted spectral phase measurement techniques.

4.4 Comparison of MIIPS and i²PIE phase measurement techniques

This section presents and discusses the features of the novel i²PIE technique against the most commonly used MIIPS technique. Comparative analysis will also be made with pulse compression techniques that rely only on group delay dispersion (GDD) compensation such as through the use of chirped mirrors.

4.4.1 Phase measurement

The ability of each technique to accurately measure the phase distortions plays a key role in the successful compression of the pulse to a near transform limited pulse. With GDD compensated for by the chirped mirrors, the distortions resulting from higher order dispersions (HOD) are expected to dominate the spectral phase reaching the 4f-shaper. The spectral phases recorded by the MIIPS and i^{2}PIE techniques are shown in figures 4.7c and 4.8 are plotted together in figure 4.9a along with other phase measurement sets in figure 4.9. Other measurements are shown in appendix A.1. These phases are plotted within the region of SC intensity hence regions where the signal is above the calculated spectrometer noise. The phase values at the central frequency were overlaid by shifting the measured phase by a constant. This constant term added to the phase has no effect on the pulse in the temporal domain as it only shifts the position of the pulse. It is observed that for each measurement, the

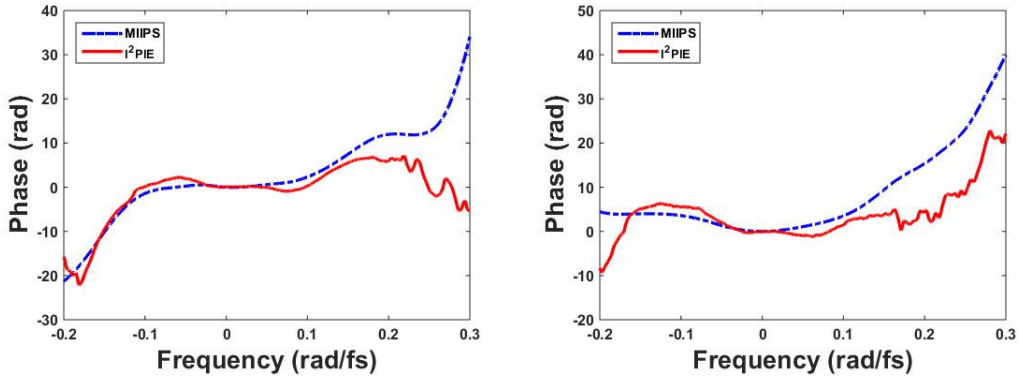

(a) Spectral phase set 1 **(b)** Spectral phase set 2

Figure 4.9: Comparison of spectral phases measured with MIIPS and i^{2}PIE. Spectral phase measured with MIIPS (dash blue lines) and i^{2}PIE (solid red line) techniques are shown plotted within regions of significant SC intensity i.e intensities above 3 times the standard deviation of the background. (a) represents an overlay of the phases plotted in figures 4.7c and 4.8b. Other measurements are shown in appendix A.1. The matlab code used can be found in appendix C.2.

same phase trend is observed but i^{2}PIE phase (solid red lines) shows more structure than the MIIPS phase (blue dash lines). The modulations in the i^{2}PIE phase can be attributed to its sensitivity to the complex phase of the pulse. This implies i^{2}PIE offers a better measurement of HODs thereby making it more accurate in measuring the phase for each spectral component. These results confirm that the MIIPS technique is limited in its sensitivity to detect HODs. It considers only second order dispersion (SOD) corrections [67, 124] which reduces its accuracy in comparison to i^{2}PIE.

Although both MIIPS and i^{2}PIE are both pulse shaper assisted phase measurement techniques, it has been shown that their implementation and phase reconstruction algorithms differ. MIIPS requires an iterative set of measurements with an algorithm that updates the phase per iteration until the residual phase converges to a

zero phase between iteration. In i^{2}PIE however, only one set of measurement is required from which the phase of the pulse can be derived using a reconstruction algorithm. Therefore in terms of implementation, the new i^{2}PIE technique has several advantages over MIIPS in that it is a faster technique since fewer measurements are required. The elimination of the iterative process also contributes to the speed of implementation. The results obtained here have also proven i^{2}PIE to be more sensitive to the complex phase and therefore offers better phase measurement and reconstruction.

Pulse compression is performed by applying the negative of the measured phase onto the SLM with the aim of achieving a zero phase on the pulse. Applying the negative of this measured spectral phase compensates for the spectral distortions thereby producing a pulse with a negligible phase. This pulse, with a negligible spectral phase, results in a near transform limited pulse in the temporal domain. In order to determine the actual pulse duration after compression, it was necessary to measure the durations with an autocorrelation since an autocorrelation provides a quantitative way to estimate the degree of compression achieved by each technique.

4.4.2 Pulse duration measurements

The pulse duration of the chirped mirror compressed, MIIPS compressed and i^{2}PIE compressed pulses were measured using a spatial light modulator through a collinear autocorrelation. As stated in section 3.3.1, a collinear autocorrelation can be performed with the SLM by applying an appropriate transfer function. Pulse durations for the supercontinuum generated pulses were measured by performing non-interferometric collinear autocorrelation (NICA) using SHG signals generated from a nonlinear (BBO) crystal. The transfer function applied is as stated in equation 3.3.2 with $\Gamma = 0$. Figure 4.10 shows the frequency-time SHG autocorrelation spectrograms recorded for a pulse with a time step size of 5 fs between the two pulses. The time delay is based on the number of steps taken within a defined scanning temporal window. A temporal window of 2 ps was chosen and scanned between -1 to 1 ps in 401 steps. The higher the number of steps taken within a defined window, the better the resolution of the autocorrelation traces. The second harmonic response trace corresponding to a measurement of the SC pulse with only GDD compensation (chirped mirror (CM) compression only) is shown in figure 4.10a with figures 4.10b and 4.10c representing that of MIIPS and i^{2}PIE compressed SC pulses respectively. In all spectrograms, the intensity is maximum at time, t = 0, corresponding to a zero delay between the two replica pulses on the SLM. Comparing the trace responses recorded, i^{2}PIE provides the highest response. This is simply as a result of the higher peak intensity generated from the shorter pulse duration it provides.

Integrating the SH intensities for each frequency component at each time delay results in a temporal pulse profile as shown in figure 4.10d. In determining the temporal widths of these autocorrelations, the pulse durations for each technique was determined by measuring the FWHM after fitting with a Gaussian curve. The average autocorrelation durations, τ_A measured for each technique is listed in table 4.2 together with the calculated pulse durations, τ_p obtained by applying equation 3.3.3.

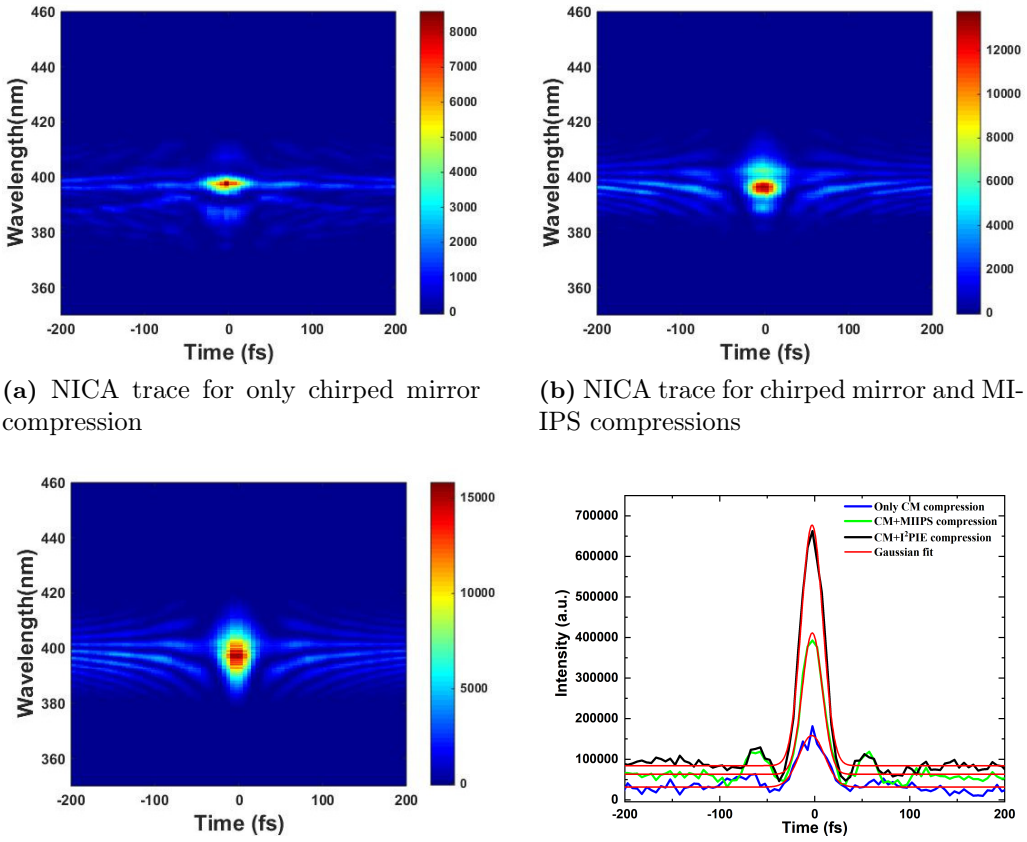

(a) NICA trace for only chirped mirror compression

(b) NICA trace for chirped mirror and MIIPS compressions

(c) NICA trace for chirped mirror and i^{2}PIE compressions

(d) Pulse durations measured based on compression technique

Figure 4.10: Compression technique-based non-interferometric collinear autocorrelation traces for (a) Chirped mirror (CM) compression only, (b) MIIPS compression after CM compression, (c) i^{2}PIE compression together after CM compression. Pulse durations measured via non-interferometric collinear autocorrelation for the different pulse compression techniques is shown in (d). The generated matlab code used in analysing the spectrograms can be found in appendix C.3.

Table 4.2: Durations of pulses based on compression technique

Technique	τ_A (fs)	τ_p (fs)
Chirped mirrors (CM) only	35.8	25.3±1.0
CM + MIIPS	29.8	21.1±0.8
CM + i^{2}PIE	25.3	17.9±0.7

The fundamental pulse however does not pass through the SLM as can be seen from the layout in figure 3.8 and therefore can not be measured with the NICA technique. The pulse duration for the fundamental pulse was therefore estimated using Lab2 virtual femtosecond laboratory package[2] [144] in LabView since it could

[2]Available at http://lab2.de/

not be measured directly at the experimental plane due to the system layout. The program code developed from the package for pulse length estimation is shown in appendix B.1. It calculates the change in electric field due to propagation through a transparent but dispersive medium. The response of the material is calculated using the Sellmaier equations. The Lab2 package provides a complimentary database of common transparent materials with predefined Sellmeier coefficients. It estimates the duration after each dispersive element based on the Gaussian time bandwidth product (TBP) for a chirped pulse [145]:

$$TBP = 0.441\sqrt{\left[1 + \left(\frac{b}{a}\right)^2\right]} \tag{4.4.1}$$

where a and b represent the duration of the incoming pulse and the linear chirp parameter of the dispersive medium respectively. The optical elements traversed by the fundamental pulse before reaching the focal plane are (from figure 3.8): the polarization beam splitter cube (P.B.C.), the beam expander lens (B.E.L1 and B.E.L2) and the microscope objective lens. The dispersive materials used in the fabrication of each element is provided in table 4.3[3]. With the microscope objective assumed to be fabricated from 30 mm of Calcium Fluoride (CaF_2) due to its low spectral dispersion over a broad wavelength range [146], the estimated pulse durations after each dispersive element is shown in table 4.3.

Table 4.3: Optical elements and their GVD

Optical element	Material	Thickness (mm)	Output duration (fs)
P.B.C.	N-SF1	10	90
B.E. L1	N-LAK22	8.0	110
B.E. L2	N-LAK22	9.3	130
Objective lens	CaF_2	30	160

The success of each SC compression technique was also determined by measuring the spectral bandwidth of the SHG signal generated for each technique at the point of no time difference between the two replica pulses on the SLM (i.e. $t = 0$) where the intensity is maximized. These were compared to the spectrum of the total SHG signal expected to be generated by the SC pulse assuming 100% conversion efficiency and perfect phase matching for all spectral components. This expected signal was calculated by performing an autocorrelation of the SC pulse with itself and is represented by the black spectra lines in figure 4.11.

The calculated SHG signal averaging a spectral FWHM of 31.9±0.8 nm is shown by the black arrows in figure 4.11a. The FWHM recorded for the three techniques (represented by "X" in figure 4.11) are averaged 12.0±1.1 nm, 14.7±0.4 nm and 19.2±0.3 nm representing 37.7%, 46.0% and 60.1% conversion efficiencies for CM, MIIPS and i^{2}PIE respectively. The second harmonic response, like in many other

[3]Materials sourced from Thorlabs website https://www.thorlabs.com

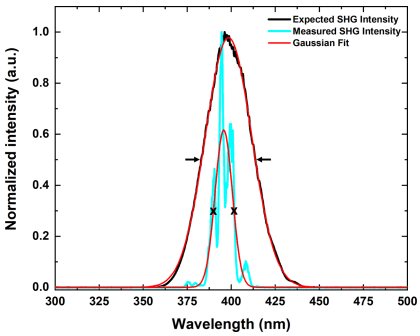

(a) SHG signal efficiency with chirped mirror compression

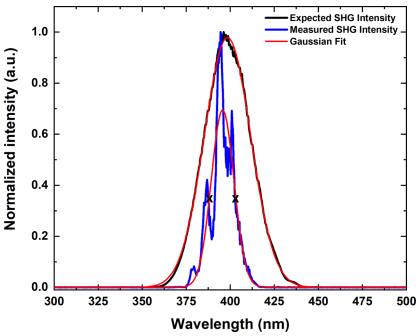

(b) SHG signal efficiency with MIIPS compression

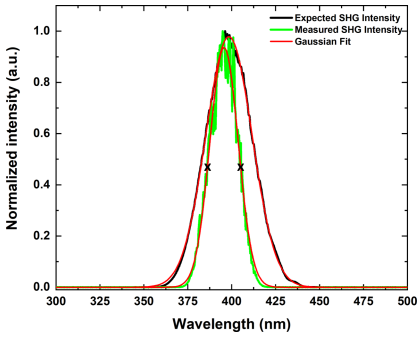

(c) SHG signal efficiency with i^{2}PIE compression

Figure 4.11: SHG efficiency based on phase compensation technique employed. The expected SHG spectrum to be generated from the SC pulse is shown in black in each of the plots. The SHG generated at time t=0 in the NICA (ref figure 4.10) is depicted in cyan, blue and green for chirped mirror, MIIPS and i^{2}PIE compressions respectively. The arrows in (a) and 'X' in (a-c) represent the FWHM positions in each spectrum.

parametric processes, is dependent on effective phase matching between the interacting fields. Results from figure 4.11 implies better phase matching is achieved with i^{2}PIE compression hence the greater response generated.

Considering the spectral phase measured with each characterization technique, the pulse durations recorded and the SHG conversion efficiencies, i^{2}PIE is seen to provide better pulse compression for broadband supercontinuum pulses than MIIPS. The sensitivity of i^{2}PIE to higher order phase distortions leads to better phase measurement hence better pulse compression. The duration of the SC pulse at the sample position is significantly shorter for i^{2}PIE compression than with MIIPS compression. This yields higher intensities and ultimately higher SHG signals.

4.4.2.1 Effect of ND filter on pulse duration

In order to reduce photodamage and photobleaching in imaging, the peak power impinging on the sample is often attenuated with neutral density (ND) filters. These glass materials also add phase to the incoming pulse. Our setup consists of a 2 mm

thick rectangular reflective ND filter (NDL-25C-2, Thorlabs, Fused silica) with a continuous variable optical density of 0.04 - 2.0. We investigated the effect of the optical density (OD) of the filter on the temporal pulse, in order to ensure that by changing the OD of the filter, we do not alter the duration of the laser pulse incident on the sample. With the ND filter removed from the beam path, the (free space) phase was measured and compensated using both MIIPS and i^{2}PIE techniques. These measurements were repeated with the ND filter in place.

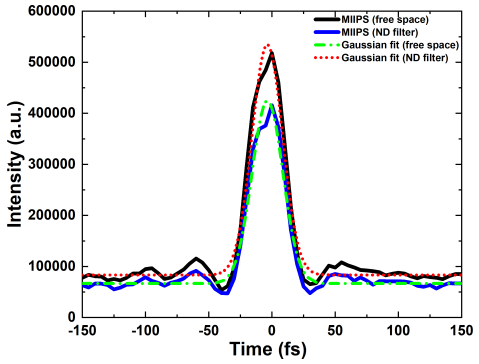

(a) Temporal profile of pulse after MIIPS compensation through free space and ND filter.

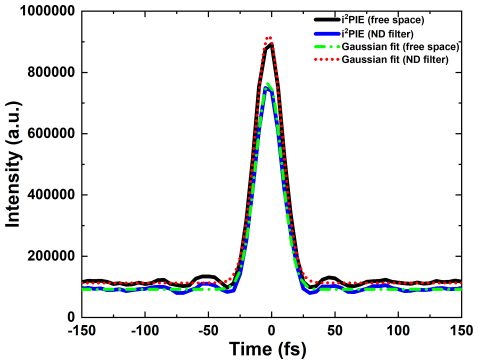

(b) Temporal profile of pulse after i^{2}PIE compensation through free space and ND filter.

Figure 4.12: Determining the effect of ND filter on the temporal pulse. (a) and (b) represent the temporal profile of pulse after compressions with MIIPS and i^{2}PIE respectively with free space temporal pulses (black lines) and temporal pulses after traversing the ND filter (blue). The red and green lines represent Gaussian fit on the respective graphs.

The pulse durations measured with the MIIPS and i^{2}PIE techniques are shown in figures 4.12a and 4.12b respectively with the free space durations in black and the durations measured after traversing the ND filter given in blue. There is a decrease in intensity as a result of the introduction of the ND filter. Fitting both pulses with a Gaussian, the average duration of the compressed pulse propagating through free space was determined to be 20.9±1.0 fs for MIIPS and 17.3±1.0 fs for i^{2}PIE. The corresponding average durations after propagating through the ND glass was found to be 21.3±1.0 fs and 18.1±1.0 fs for MIIPS and i^{2}PIE respectively. These results indicate that there is no significant difference in durations measured through free space and through the ND filter. They further prove that each phase measurement technique compensates effectively for phases introduced in the path of the pulse and ultimately, in the plane of the object, the phase is zero. Furthermore, these results show that the compression only depends on the phase of the pulse and not the intensity thus changes in the intensity by the OD does not change the phase of the pulse.

4.5 Spatial resolution and contrast measurements

The ability of our nonlinear microscope to resolve the fine spatial features was determined using 2 μm sized fluorescent beads. Figure 4.13 shows the two photon excitation fluorescence intensity recorded from two adjacent fluorescent beads shown in 4.13a using the fundamental pulse. The scanned image was taken at a damage threshold energy of 1.9 nJ per pulse as any energy above resulted in photo degradation of the sample. The micrograph image taken with the CMOS monochrome camera integrated in the setup is shown in figure 4.13a. Figures 4.13b and 4.13c show a 3D and 2D representation of the fluorescence signal response recorded after a raster scan imaging. There is a clear distinction between the peaks of the two beads as expected for well resolved images.

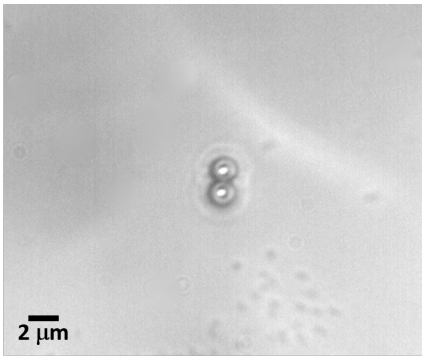

(a) Micrograph of fluorescence beads

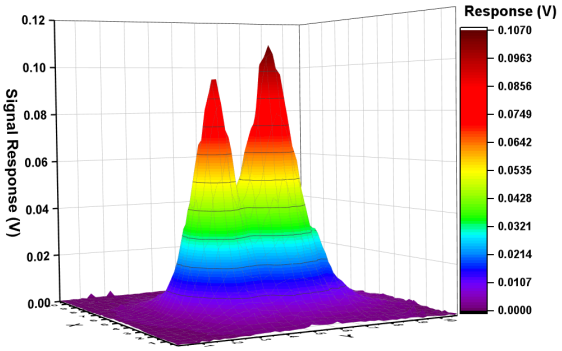

(b) 3D-Surface plot of TPEF intensity from beads

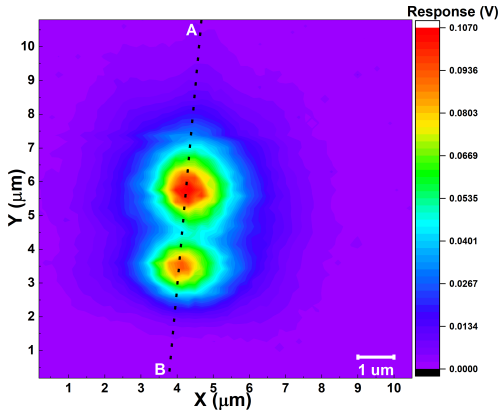

(c) TPEF image of fluorescence beads

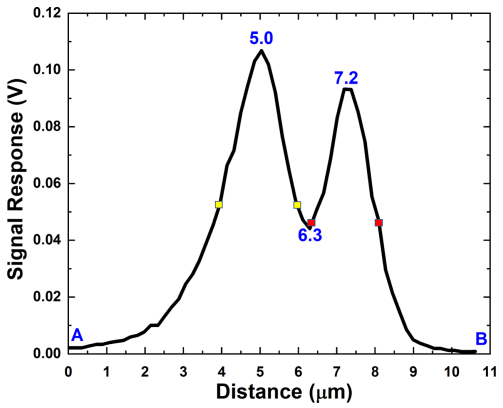

(d) Cross section across peaks of beads

Figure 4.13: TPEF signal images recorded from fluorescence beads. Micrograph captured with CMOS monochromatic camera is shown in (a) with corresponding 3D and 2D representation of intensity given in (b) and (c) respectively. (d) represents an intensity cross section taken between point A and B across the beads along dotted lines in (c).

Throughout this dissertation, signal contrast will be calculated using the Weber

contrast approach [56]:

$$\text{Contrast} = \frac{\text{L}_{\text{max}} - \text{L}_{\text{min}}}{\sigma_{\text{background}}} \tag{4.5.1}$$

where L_{max} is the maximum signal response, L_{min} is the minimum response and $\sigma_{\text{background}}$ is the standard deviation of the noise. The signal-to-noise ratio (SNR) will also be calculated using the expression:

$$\text{SNR} = \frac{\text{maximum mean intensity}}{\sigma_{\text{background}}} \tag{4.5.2}$$

The standard errors (SE) in all the mean measurements will be calculated using the standard error equation

$$\text{SE} = \frac{\sigma_m}{\sqrt{n}} \tag{4.5.3}$$

where σ_m represents the standard deviation of the measured mean values and n represent the number of measurements taken. Therefore for figure 4.13, using equations 4.5.1 and 4.5.2, a contrast of 289.1 ± 27.0 was determined and the signal-to-noise was found to be 102 ± 5.7.

Considering the 800 nm central wavelength and the 0.9 NA focusing objective, the calculated lateral resolution, based on the 2-point separation equation (1.4.5) ($r = \frac{0.61\lambda}{1.31\text{NA}}$) is 413 nm. The axial resolution, based on equation 1.4.4b ($r = \frac{2n\lambda}{(\text{NA})^2}$ with $n = 1$ due to air objective used) is calculated as 2.0 μm. The minimum resolvable distance for our system was determined by recording the fluorescence intensity across the maxima of the beads (represented by the black dash lines between points A and B in 4.13c). The resulting plot is shown in figure 4.13d with a peak to peak separation distance of 2.2 μm between the two beads. This separation distance is approximately 7 times large than the diffraction limit which contributes to the well resolved peaks shown in figure 4.13b. The fluorescence intensity FWHM (coloured marks on 4.13d) for the two beads is measured to be 2.0±0.2 μm and 1.8±0.2 μm respectively which corresponds to the specified size of the beads.

4.5.1 Spot size determination

The lateral resolution of the system was determined by adapting a technique analogous to the open z-scan technique [139] as explained in section 3.3.2. The Rayleigh length (Z_0) can be determined from the generated SH intensity (P_{2w}) by applying equation 3.3.13. From the resulting Z_0, the beam radius in the focus can be calculated using equation 3.3.6. Figure 4.14 shows the measurement of second harmonic power $P_{2w}(z)$ generated in a thin layer of urea crystal as a function of sample position z for the different pulse compression techniques. The solid curve is the fit based on equation 3.3.13 with the fit parameters Z_0 and K. The average Rayleigh length, Z_0, for the fundamental pulse with 800 nm central wavelength was found to be $Z_0 = (1.054 \pm 0.003)$ μm corresponding to a beam waist of $w_0 = 0.518$ μm (from equation 3.3.6). The beam spot diameter was determined to be (1.036 ± 0.006) μm. The average spot size parameters recorded for the different pulse techniques are given in table 4.4.

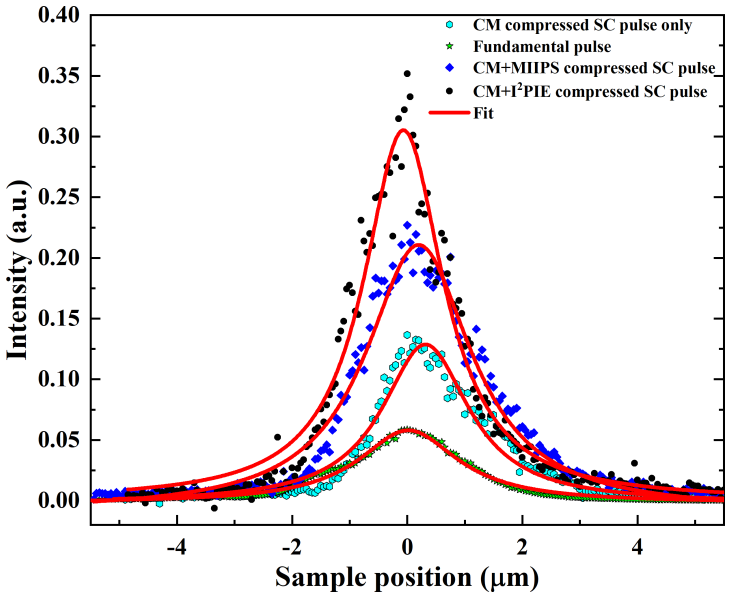

Figure 4.14: Measurement of the beam radius at the sample position z = 0 on a thin layer of urea. Solid curve is a fit according to equation 3.3.13.

Table 4.4: Spot size determination for different compression techniques

Technique	Rayleigh length (Z_0)	Beam radius (w_0)	Spot size (μm)
Fundamental pulse	1.05 μm	0.52 μm	1.04±0.01
Chirped mirror only	0.92 μm	0.49 μm	0.98±0.01
MIIPS pulse	1.02 μm	0.51 μm	1.02±0.01
i^{2}PIE pulse	0.84 μm	0.46 μm	0.92±0.01

It can be observed that the beam radius, w_0, is the same (to a 1 decimal approximation) for the fundamental as well as the compressed SC pulses. This implies that no beam distortion occurred irrespective of the phase measurement and compression technique used hence the spatial profile is not altered. As previously calculated in section 4.5, the lateral resolution for second order nonlinear microscopy is 0.41 μm which gives a calculated spot size of 0.82 μm. Our measured spot sizes are larger by an average of 0.18 μm representing a 20% increase in the spot size of our system.

4.5.2 Peak intensities in focal spot

The signal response in imaging is dependent on the intensity of the pulse in the focal spot. As stated previously, the repetition rate of the laser used in this work is 80 MHz. Assuming an input pulse with 40 mW average power, then from equation 1.2.1 (i.e. $I = \frac{E}{A\tau}$), the peak intensity using the durations and beams radius from tables 4.2 and 4.4 is summarised in table 4.5. A higher intensity is recorded with the use of SC pulse pulse with i^{2}PIE providing the highest. Comparing the intensities for MIIPS and i^{2}PIE, there is an 18% increase in the i^{2}PIE intensity over that of MIIPS as a result of the shorter pulse duration achieved upon compression.

Table 4.5: Laser peak intensities in sample plane

Technique	Peak intensity (TW/cm^2)
Fundamental pulse	0.4
Chirped mirror only	2.5
MIIPS pulse	3.0
i^{2}PIE pulse	3.6

4.5.3 Signal strength for each compression technique

The strength of the second order nonlinear signal response for each compression technique in a nonlinear medium was measured by recording the SHG signal from a BBO crystal. As a control, the SH response was also determined under the same energy per pulse conditions with the fundamental pulse. Figure 4.15 shows the signal responses for an input pulse energy of 500 pJ per pulse (40 mW average power at 80 MHz repetition rate) from BBO placed in the focus of microscope objective. The signal recorded by fibre coupling into a spectrometer is shown in

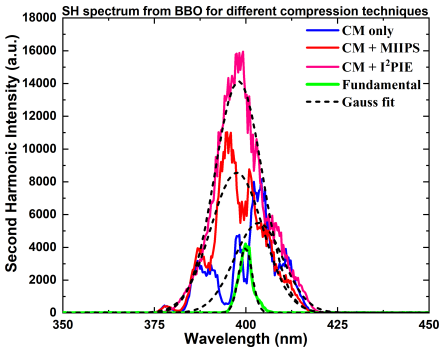

(a) SH spectrum from BBO for different compression techniques

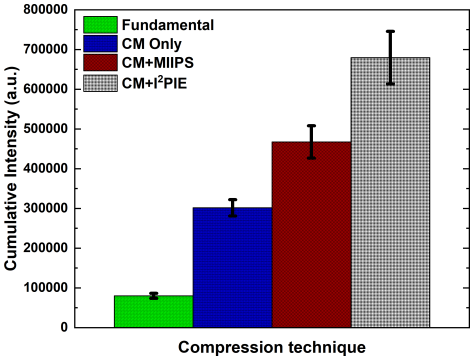

(b) SH intensities recorded for a fixed pulse energy based on compression technique

Figure 4.15: Comparison of SH spectra generated by same energy pulses in BBO for the different pulse durations. Figure 4.15a shows the SH intensities recorded for each focus position in the crystal with the integrated intensities for the entire spectral bandwidth shown in figure 4.15b. Signal recorded for the fundamental pulse in (b) has been enhanced by a factor of 2 for illustration purposes.

figure 4.15a. Second harmonic intensity recorded for the fundamental pulse which has not undergone any pulse compression is shown in green. Signals generated from the compressed SC pulses are shown in blue, red and magenta for compressions with chirped mirrors (CM-only), MIIPS and i^{2}PIE respectively. For comparison purposes, the spectra were Gaussian fitted and the peak of the Gaussian profiles were assumed to be the highest SHG intensities recorded. The SNR averaged 3.2 ± 0.5 (fundamental), 9.5 ± 0.7 (CM-only), 17.3 ± 1.4 (MIIPS) and 25.5 ± 2.1 (i^{2}PIE). During raster scanning in nonlinear imaging, the generated signal is recorded with a

photomultiplier tube (PMT) which records the integrated number of photons striking the detector for each position. The integrated responses for each technique in figure 4.15a are shown in figure 4.15b. The integrated intensities recorded in arbitrary units are $8.0 \times 10^4 \pm 6.2 \times 10^2$ (fundamental), $3.0 \times 10^5 \pm 2.1 \times 10^4$ (CM-only), $4.7 \times 10^5 \pm 4.1 \times 10^4$ (MIIPS) and $6.8 \times 10^5 \pm 6.6 \times 10^4$ (i^{2}PIE). It can be seen that as expected, there is an improvement in the integrated intensities recorded when smaller pulse durations are used. For example, comparing the signals recorded with the fundamental pulse to that of the SC source, there is a 3.8 fold increase in the signal response in the use of SC pulse with only GDD compensation by the chirped mirrors. Further compressing this SC pulse with MIIPS offers a 5.8 fold increase over the fundamental pulse. Where i^{2}PIE was employed, an 8.5 fold in signal strength was recorded. Comparison of the signals among the different techniques employing SC source are also provided in table 4.6. It should also be noted that the detection efficiency of the PMT is limited by the detection range, detector response time and noise.

Table 4.6: Comparison of SHG signal responses in BBO based on compression technique

Technique	Fundamental	CM-only	MIIPS	i^{2}PIE
Fundamental	1.0	3.8	5.8	8.5
CM-only		1.0	1.5	2.3
MIIPS			1.0	1.5
i^{2}PIE				1.0

Two photon excitation fluorescence signal response were also investigated using fluorescent micro-beads. Figure 4.16 shows the scan results obtained for the different techniques with a 125 pJ energy pulse. The low pulse energy was chosen specifically to reduce the risk of photobleaching of the fluorophores since multiple scans were needed to be conducted on the same beads. Signal responses were detected in transmission with a PMT. Figures 4.16a to 4.16d shows the TPEF responses recorded with the fundamental pulse, the CM, MIIPS and i^{2}PIE compressed pulse. For clarity purposes, the response from the fundamental has been enhanced by a factor of 2. As expected, the highest signal response was recorded with the use of i^{2}PIE followed by MIIPS and GDD-only compensated pulses with the chirped mirrors. The contrast and SNR recorded for each technique are provided in table 4.7. Comparing the contrasts recorded for MIIPS and i^{2}PIE, an average increase of 2.0 fold is observed with a corresponding $\approx$ 1.7 fold average increase in SNR.

A comparison of the average signal intensity response from line sections is shown in figure 4.17 with regions of interest highlighted. It should be noted that the image of i^{2}PIE used here is just to indicate the cross section region taken across the images for all techniques. The intensity plots represent the average response values in the selected regions. Considering the intensities at the peaks (marked with the vertical dash magenta lines in the line plots of figure 4.17) there is an approximate 2.0 fold

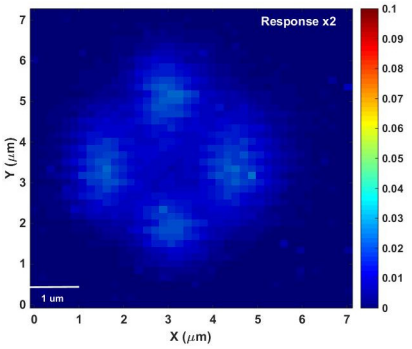

(a) TPEF image of fluorescence beads using the fundamental pulse from the laser cavity.

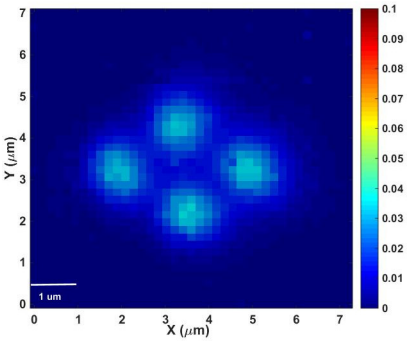

(b) TPEF image of fluorescence beads with SC pulse compressed with only chirped mirrors

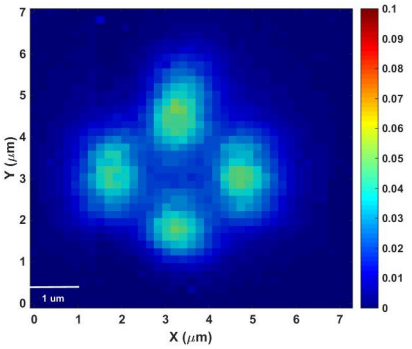

(c) TPEF image of fluorescence beads with SC pulse compressed with CM and MIIPS

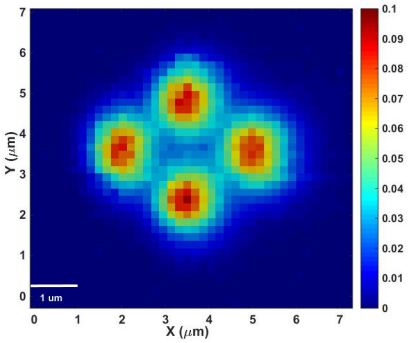

(d) TPEF image of fluorescence beads with SC pulse compressed with CM and I^{2}PIE

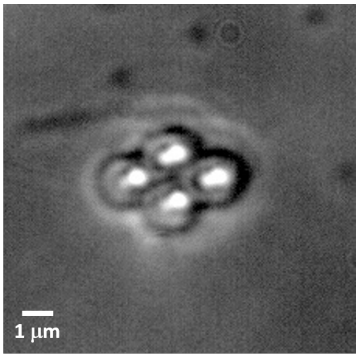

(e) Micrograph of fluorescence beads

Figure 4.16: TPEF image of fluorescence beads imaged under the four configurations: fundamental laser (a), SC with only chirped mirror (CM) compression (b), SC with CM and MIIPS compression (c) and SC with CM and I^{2}PIE compression (d). Micrograph image taken with the CMOS camera is shown in (e). All scan images taken under same conditions with pulse energy of 125 pJ with same intensity scale.

increase in the intensity signals recorded for i^{2}PIE scans over that of MIIPS and

Table 4.7: Contrast and signal-to-noise ratio measurements for TPEF in fluorescent beads

Technique	Contrast	Signal-to-noise ratio
Fundamental pulse	49.2±6.6	18.6±2.4
Chirped mirror only	112.9±5.8	41.4±2.1
MIIPS pulse	152.6±9.2	69.4±4.1
i^{2}PIE pulse	305.8±20.7	118.0±8.0

approximately 7.6 fold increase in i^{2}PIE over imaging with the fundamental pulse.

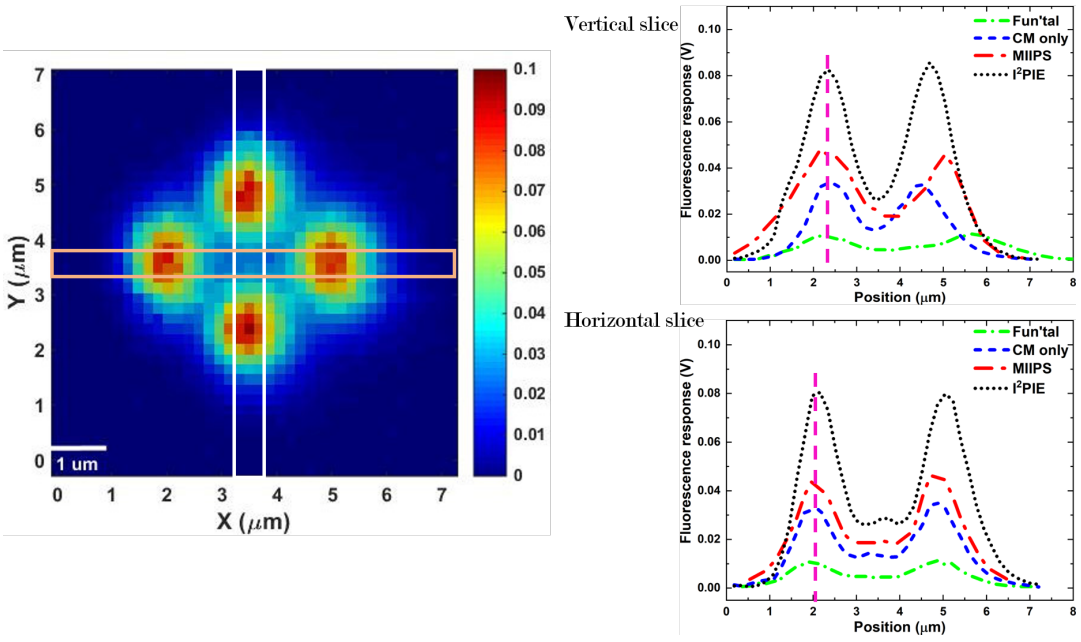

Figure 4.17: Intensity plots for fluorescence response for the different techniques. Region for vertical scan is shown in white and region for horizontal scan is shown in brown. Average intensity plots for vertical and horizontal regions are shown on top right and bottom right respectively. Magenta lines in intensity plots represent region of intensity comparison.

There is therefore an overall increase in the signal strength recorded with the use of i^{2}PIE compressed pulse over that of MIIPS and GDD-only compensated pulses. This result is attributed to the higher peak intensity generated by i^{2}PIE due to the shorter pulse duration achieved with its application in pulse compression. The high contrast also leads to a better image resolution as the beads are more distinct in the i^{2}PIE image compared to the images obtained with the other techniques.

4.6 Temporal evolution of fluorescence based on compression technique

In laser-based imaging applications with fluorophores, the fluorescence signal response decreases over time as a result of the irradiation of fluorophores with high intensity pulse. This section presents and discusses the results obtained from the investigations into how the various techniques employed in this work affect the temporal evolution of the fluorescence signals recorded.

The fluorescent microbeads were used to study the effects of each phase measurement and compression technique on the temporal evolution in fluorescence response. These beads were chosen over biological tissue due to the homogeneous distribution of fluorophores across the beads' surface compared to those contained in biological samples. The temporal evolution investigated is the photobleaching of the fluorophores [147]. Photobleaching is the destruction of fluorophores in the excited state. This photobleaching can be reversible, in that the fluorescence intensity returns to a maximum after the irradiation source is removed, or irreversible which leads to a permanent depletion of fluorescence intensity. Upon laser irradiation, these fluorophores undergo an absorption-emission cycle. The fluorescence intensity however decreases exponentially in time due to some molecules fluorescing into a reversible or irreversible states. There are numerous pathways for the energy - each pathway has an associated timescale - the irreversible processes result in fluorescence decay over time. These decays can be represented as the sum of exponential decays of the form:

$$I \propto I_o + \sum_{i=1}^{n} A_i \exp(-\frac{t}{\tau_i}) \tag{4.6.1}$$

where I_o is the intensity offset with A_i and τ_i representing the components of each timescale and the decay timescales respectively. Fitting the photobleaching process with such an exponential fit leads to the extraction of the decay time constant(s) for the process(es) involved. Assuming a single process dependent photobleaching process, equation 4.6.1 reduces to:

$$I \propto I_o + A_1 \exp(-\frac{t}{\tau_1}) \tag{4.6.2}$$

Fluorescent microbeads sonicated in methanol were spin coated onto a microscope cover slide for our investigations. Figure 4.18 shows, an example, the photobleaching curve recorded after irradiation with an i^{2}PIE compressed pulse of 150 pJ for about 1000 seconds. After 380 seconds, the laser was blocked for 280 s before allowing irradiation to continue. It is observed that fluorescence did not recover to a maximum when irradiation was resumed. This shows that the photobleaching process of the "light yellow" fluorophore is an irreversible process. Assuming a single decay pathway and fitting with equation 4.6.2, a decay constant of 61.6 s was recorded. Since the photobleaching process is irreversible, it was ensured that each subsequent measurement was taken at a different position to ensure maximum signal strength for each measurement.

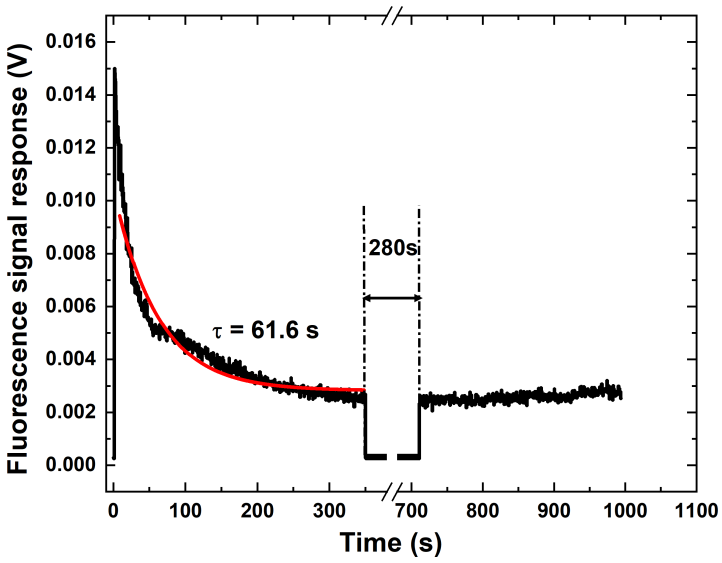

Figure 4.18: Fluorescence photobleaching process in fluorescent micro beads as a function of irradiation time. Broken lines represent the period of no irradiation.

We investigated whether the the photobleaching was a function of intensity of energy. We did this by irradiating the sample with pulses of different energy but equal intensity, as well as pulses of equal energy but different intensities.

4.6.1 Temporal evolution based on same input pulse energy

Figure 4.19 shows the fluorescence signal recorded for the CM-only, MIIPS and i^{2}PIE compressed pulses as a function of irradiation time. Irradiation was carried out with a constant pulse energy of 188 pJ (15 mW average power). Again assuming

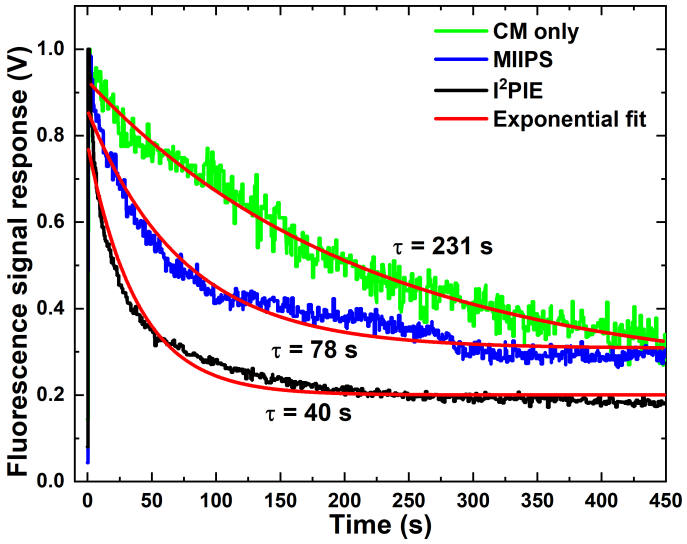

Figure 4.19: Photobleaching curves for GDD-only, MIIPS and i^{2}PIE compressed pulses at the same excitation energy of 188 pJ (15 mW average power).

a single process thus with a single exponential function, the average fit parameters extracted are summarized in table 4.8. Irradiating with the same input energy results

Table 4.8: Photobleaching parameters for irradiation with constant input pulse energy

Technique	Power (mW)	Int. (TW/cm^2)	A_1	time constant (τ_1) (s)
CM-only	15.0	0.95	0.69±0.08	231±6.0
MIIPS	15.0	1.13	0.55±0.03	78.3±5.0
i^{2}PIE	15.0	1.33	0.58±0.03	40.3±3.0

in different pulse intensities in the focal plane due to the different pulse durations achieved upon pulse compression. For fixed irradiation area (A) and pulse energy (E), the intensity (I) is inversely proportional to the pulse duration (i.e. $I = \frac{E}{A\tau}$). Thus the shorter pulse durations, the higher the intensity which leads for faster time constant. It has already been established, (from table 4.2), that compression with i^{2}PIE results in shorter pulse durations which results in higher intensities thereby resulting in a faster decay process as seen evident in figure 4.19.

4.6.2 Temporal evolution based on same input pulse intensity

The photobleaching effects for a irradiation with a pulse of constant intensity was investigated for MIIPS and i^{2}PIE techniques. An intensity of 0.9 TW/cm^2 was calculated. From the pulse durations, this translates into the use of an input power of 12 mW and 10 mW for MIIPS and i^{2}PIE techniques respectively. The photobleaching curve is as shown in figure 4.20 with the corresponding fit parameters listed in table 4.9. It is observed that within the error limits, the time constants for the two

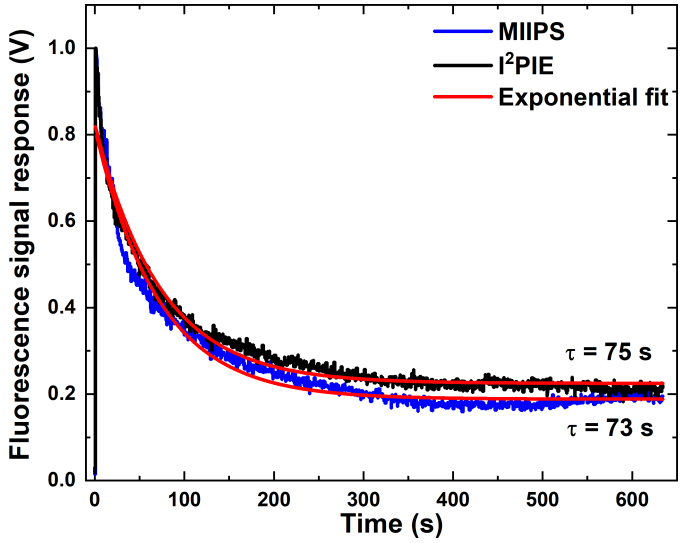

Figure 4.20: Photobleaching curves for MIIPS and i^{2}PIE compressed pulses at the same excitation intensity of 0.9 TW/cm^2 (average power of 12 mW for MIIPS and 10 mW for i^{2}PIE).

Table 4.9: Photobleaching parameters for irradiation with constant intensity

Technique	Power (mW)	Int. (TW/cm^2)	A_1	time constant (τ_1) (s)
MIIPS	12	0.9	0.57±0.01	73.3±0.9
i^{2}PIE	10	0.9	0.60±0.01	74.9±1.4

techniques are the same. The time constant (τ_i) is related to the laser intensity (I) by the power law such that $\frac{1}{\tau_i} \propto I^{n_i}$ with n_i being the required number of photon absorption processes involved in the excitation process. The constant time constant implies the photobleaching dynamics involve the same n-photon absorption process. The exact number of absorption processes involved was however not investigated as this was beyond the scope of this dissertation.

4.7 Chapter summary

This chapter has focused on investigating the unique features of the microscope constructed as part of this dissertation. The supercontinuum spectrum generated by the new polarization maintaining all-normal dispersion photonic crystal fibre has been shown to provide more stability than its non-polarization maintaining counterpart. This high spectral stability translates into a more stable temporal pulse profile which can be coherently controlled.

By utilizing the 4f shaper and SLM incorporated into the constructed setup, the features of the new i^{2}PIE phase measurement technique recently developed in our lab have been investigated. i^{2}PIE, like MIIPS, is a collinear technique where the phase measurement and correction are performed with the same setup. This therefore provides a much simplified phase measurement technique than FROG and SPIDER. Though MIIPS and i^{2}PIE require the same experimental setup, i^{2}PIE has proven to have a lot of advantages over MIIPS as a phase reconstruction technique. It has been shown, in this chapter that i^{2}PIE provides a more accurate phase measurement than MIIPS due to the sensitivity of the algorithm to the complex spectral profile of the pulse. This has been shown to ultimately lead to better phase compensation and temporal pulse compression. In employing non-interferometric collinear autocorrelation (NICA), our results have confirmed that i^{2}PIE offers better pulse compression resulting in higher peak intensities than MIIPS. i^{2}PIE has also been shown to provide better contrast than MIIPS. Irrespective of the phase measurement and compensation methods employed, our results have also confirmed that the spatial profile of the beam in the focus of the microscope objective is preserved. With many microscopy applications [41, 65, 66] relying on MIIPS to provide better image contrasts, our results confirm that this novel technique developed in-house is much better than MIIPS.

In nonlinear microscopy using crystals and fluorescence beads, i^{2}PIE has been shown to provide significant greater contrast and signal-to-noise ratios over MIIPS and GDD-only compensated pulses. The next chapter looks at the applications of these compression techniques in biophotonic applications.

Chapter 5

Biophotonic applications

5.1 Imaging applications

In this chapter, we look at the applications of the different phase measurement and pulse compression techniques in nonlinear imaging of biological tissues. Second harmonic generation (SHG) and two photon excitation fluorescence (TPEF) microscopy are demonstrated. As nonlinear microscopy permits label free imaging, investigations were carried out using both fluorophore stained samples and label-free samples. Raster scan images were recorded and for each sample, four imaging modalities were investigated. These include:

1. Imaging with the fundamental pulse directly from the laser cavity to see what conventional nonlinear imaging would offer for a specific pulse energy.
2. Imaging with supercontinuum (SC) pulse generated by coupling the laser into the novel PCF and compressed with only the chirped mirrors (CM).
3. Imaging with SC pulse further compressed with phase measured via MIIPS after pulse pre-compression with CM.
4. Imaging with SC pulse further compressed with phase measured via the novel i^{2}PIE technique after pulse pre-compression.

It is worthwhile to remember that in order to increase the signal recorded, signal responses were amplified with a lock-in amplifier and a frequency chopper with a 500 Hz frequency was used to enhance the signal-to-noise ratio (SNR) of the signal. The order of imaging acquisition is as follows: CM-only, MIIPS, i^{2}PIE and fundamental pulse. Again, as a reminder, all contrast values quoted in this chapter were calculated using equation 4.5.1 and all signal-to-noise ratios were calculated using equation 4.5.2 as defined in the previous chapter.

5.1.1 Imaging conditions

Data acquisition was performed by raster scanning across the sample in X and Y directions via a custom built Labview program (refer to appendix B.2 for user interface

of code). Integrated signal response for each scan position was recorded using a photo multiplier tuber (PMT) with signal amplification using a lock-in amplifier. The signal was modulated using an optical chopper at 500Hz and the lock-in-amplifier time constant (TC) of 8 ms was chosen. This TC offers an appreciable signal-to-noise (SNR) within the dwell time at a particular position considering the trade off between SNR and measurement time. Higher TC gives better SNR but requires a longer dwell time which can lead to damage in biological samples. Scanning was carried out with dwell time of 50 ms between successive positions. The lock-in-amplifier signals were averaged during this dwell time with the average value recorded as the response for that scan position. Raster scan movement was achieved using piezo stages with a minimum step size of 180 nm. Laser power was attenuated using neutral density filters. Appropriate band pass filters were used to block the incident radiation and transmit the generated signal, be it second harmonic generation or fluorescence.

5.2 Second harmonic generation imaging

It is a well established fact that nonlinear microscopy permits label-free imaging without the need for exogenous or introduced fluorophores. Second harmonic generation imaging was carried out on both animal tissue (porcine skin) and plant cells (guard cells). For imaging of animal tissue, a 400±10 nm bandpass filter was used to block the illumination light and transmit only the SH signals. The small transmission bandwidth ensured the detected signal was SHG dominated. Similarly for plant cells, a 360 - 580 nm bandpass was used for signal filtering.

5.2.1 Second harmonic generation in collagen

Second harmonic generation (SHG) imaging was tested using a layer of epidermal porcine tissue. Fresh porcine skin was locally sourced ensuring that the sample was preservative free in order to ensure that unknown contaminants could not contribute to the generated SHG signal. No extra purification process was carried out on the sample. A thin biopsy layer was extracted and placed in between a microscope slide and a cover glass slide for SHG imaging. A thin layer of water was added to prevent dehydration. Since it is well known that SHG from collagen in skin cells dominate the SHG response [29, 33, 35], the collagen distribution in both epidermal and dermal porcine tissue were recorded. In order to ensure strong SHG dominance in the signals recorded, a 400/10 bandpass filter transmitting the (400±10) nm spectral bandwidth was used in order to suppress any autofluorescence signals.

5.2.1.1 Second harmonic generation in epidermal porcine skin tissue

Figure 5.1 shows the second harmonic images recorded in transmission for the epidermis of porcine skin. All images were recorded with an average input power of 2 mW (which equates to a pulse energy of 25 pJ) and are plotted on the same scale for direct comparison of the signal strength. For representation purposes, the signal response recorded from the scan with the fundamental pulse and shown in figure 5.1a was enhanced by a factor of 2. An increase in signal response is evident in the use of SC pulses over the fundamental pulse. Within the SC images, the scan with

the i^{2}PIE technique (figure 5.1d) shows a response approximately 2 times greater than that of the MIIPS scan in figure 5.1c and approximately 3 times greater than the scan results obtained with only GDD compensation from the chirped mirrors (figure 5.1b). A micrograph of the portion of the skin as recorded with the CMOS monochrome camera integrated in the setup is as shown in figure 5.1e. The measured contrast and SNR are shown in table 5.1. Comparing the contrast and SNR between MIIPS and i^{2}PIE, there is approximately 2 fold increase in contrast and SNR in favour of the use of i^{2}PIE as a phase measurement technique applied in pulse compression. Table 5.2 tabulates the contrast (or SNR) enhancement factors recorded for the various modalities. The SNR values are written in parenthesis. In general, there is a better contrast (or SNR) achieved in the use of SC sources with the improvement increase from only GDD compression through MIIPS application to i^{2}PIE applications.

Table 5.1: Contrast and signal-to-noise ratio measurements for SHG in epidermal porcine skin tissue at 25 pJ input pulse energy.

Technique	Contrast	Signal-to-noise ratio
Fundamental pulse	12.3±0.7	4.6±0.2
Chirped mirror only	17.3±0.9	5.9±0.3
MIIPS pulse	69.9±16.6	18.7±4.4
i^{2}PIE pulse	135.4±16.0	31.6±3.7

Table 5.2: Contrast (SNR) enhancement factors for SHG in porcine epidermis.

Technique	Fundamental	CM-only	MIIPS	i^{2}PIE
Fundamental	1.0	1.4 (1.3)	5.7 (4.1)	11.0 (6.9)
CM-only		1.0	4.1 (3.2)	7.8 (5.4)
MIIPS			1.0	1.9 (1.7)
i^{2}PIE				1.0

5.2.1.2 Edge response approximations to contrast estimation

The edge response illustrates the system's response to a discontinuity in signals such as what typically occurs at the sharp edge of the emitting feature [148, 149]. The parameter typically used in edge response is the distance required for the edge response to rise from 10% to 90% [148]. The smaller the distance, the sharper the rise hence higher contrast. The ideal line spread function is always a step function with a signal step from 0 to maximum in a single step [149]. Considering the well defined edges in figure 5.1 it is possible to estimate which technique offers better contrast by adopting an approximation of the edge response technique.

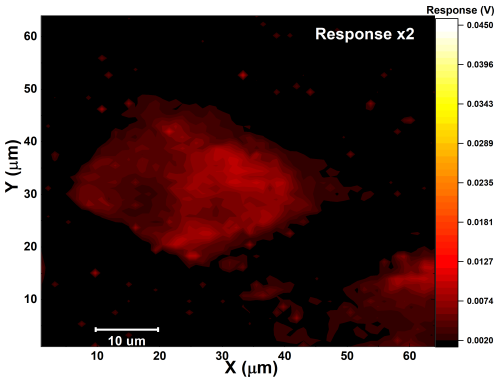

(a) Porcine SHG with fundamental pulse

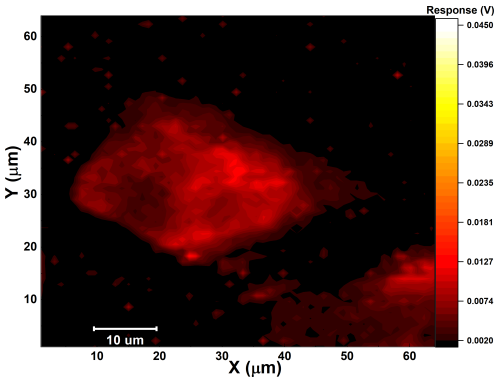

(b) Porcine SHG with only GDD compensation (CM compression)

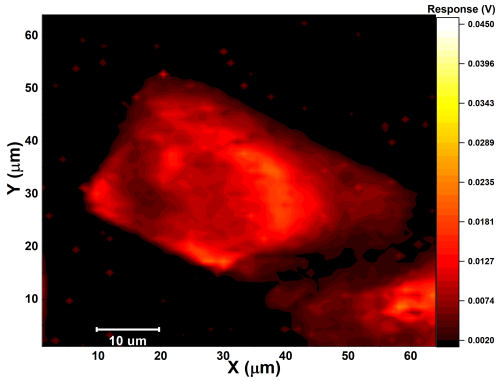

(c) Porcine SHG from CM and MIIPS compression

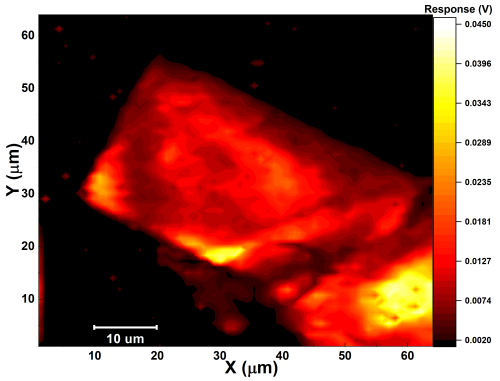

(d) Porcine SHG with CM and i^{2}PIE compression

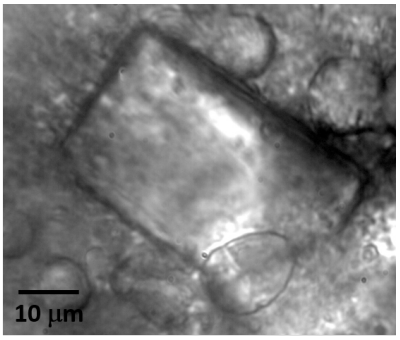

(e) Micrograph of epidermis of porcine skin tissue

Figure 5.1: SHG from the epidermis of pork skin imaged under the four configurations: (a) fundamental laser (signal enhanced by a factor of 2), SC with only chirped mirror (CM) compression (b), SC with CM and MIIPS compression (c) and SC with CM and i^{2}PIE compression (d). All images taken under same conditions with pulse energy of 25 pJ.

In order to investigate the contrast based on this technique, line scans were taken with the highlighted region of interest (ROI) in figure 5.2a. The response plots for i^{2}PIE and MIIPS techniques are plotted in figures 5.2b and 5.2c respectively. The

edge response was measured from the initial response edge as shown by the inset in 5.2b for the selected region within the broken lines. The distance between the 10% and 90% were recorded for MIIPS and i^{2}PIE compensated images within the ROI. The distances recorded averaged (2.1 $\pm$ 0.1) μm for MIIPS and (1.6 $\pm$ 0.1) μm for i^{2}PIE. A comparison of line scans for a single line within the ROI for all techniques is shown in figure 5.2d. It is observed that the steepness of the edge changes for each technique with the line scan for the image taken with the fundamental pulse providing the least contrast. These edge response readings support the fact that pulses compressed with the new i^{2}PIE technique provide a better imaging contrast than pulses compressed with MIIPS.

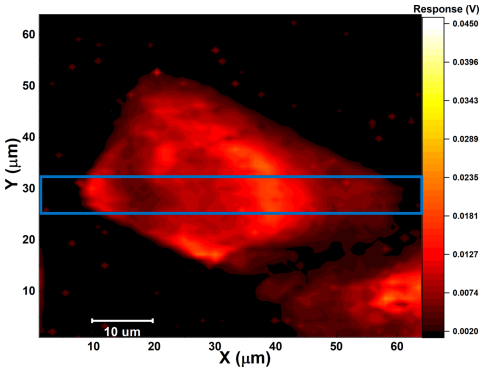

(a) Line scan regions of interest in SHG in porcine epidermis.

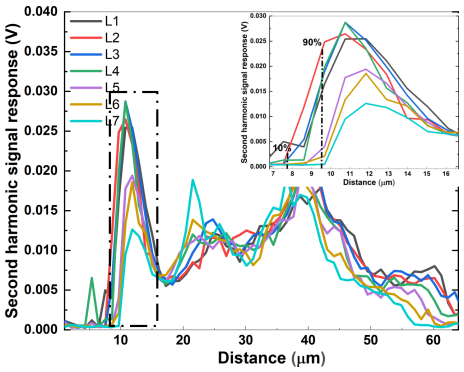

(b) SHG response plots for line scans within the ROI for i^{2}PIE.

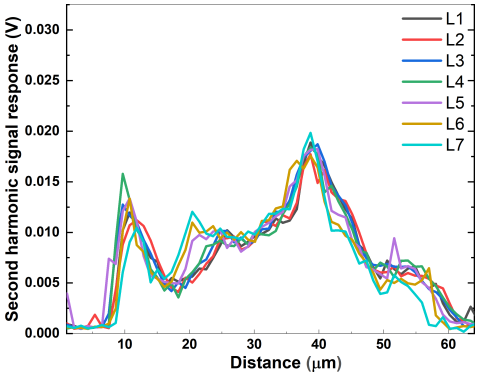

(c) SHG response plots for line scans within the ROI for MIIPS.

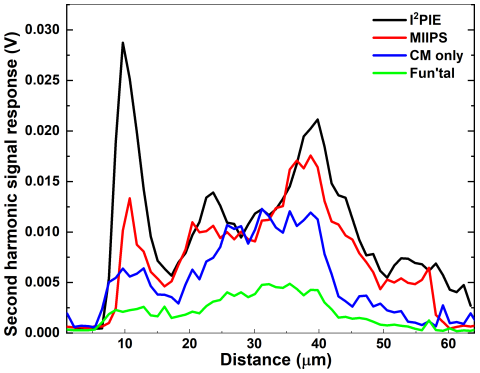

(d) Comparison of SHG response plots for line scans within the ROI for all techniques.

Figure 5.2: Line scan measurements of SHG signal response from porcine epidermis. (a) Region of interest (ROI) highlighted over the scan image obtained from MIIPS. The MIIPS image was chosen for representation purposes. (b) SHG response plots for line scans within the ROI for i^{2}PIE (Inset: Close up of response within the marked region in (b) showing the distance between the 10th and 90th percentiles). (c) SHG response plots for line scans within the ROI for MIIPS. (d) Comparison of response plots for line scans within the ROI for all techniques.

5.2.1.3 Second harmonic generation in porcine dermal skin tissue

The dermis of skin is primarily made of connective tissues consisting mostly of collagen and elastin fibres [17, 150]. These connective tissues are dominated with collagen fibre and hence a rich source of endogenous second harmonic generation. Dermal collagen fibre possess varying thickness and is crucial in determining the morphological and mechanical properties of skin [33]. These collagen fibres in a porcine dermal skin sample were imaged using second harmonic generation, which is sensitive to the fibres thickness and morphology. A biopsy of dermal tissue was extracted from the tissue just beneath the epidermis and mounted on a microscope slide. Again no extra sample preparations were performed. Figure 5.3 show the images recorded for the dermis tissue recorded for all the phase measurement/pulse compression techniques with an input pulse energy of 25 pJ. The micrograph image for the dermis is as shown in figure 5.3f. Again for illustration purposes, the signal response obtained from the scan with the fundamental pulse in figure 5.3a was enhanced by a factor of 3.

The SHG images recorded for the CM-only, MIIPS and i^{2}PIE compressed pulses are shown in figures 5.3b, 5.3c and 5.3d respectively. Similar to the plots for the epidermis, all images are plotted on the same scale for direct comparison. Considering the contrast and signal to noise ratios in table 5.3, there is an enhancement of almost 2 and 3 folds in contrast and SNR between MIIPS and i^{2}PIE respectively. Considering the line scans in figure 5.3e, which are averages of the signal responses within the blue highlighted region marked in figure 5.3d for all techniques, the higher contrast advantage of i^{2}PIE is clearly evident both in signal response as well as the steepness of the lines.

Table 5.3: Contrast and signal-to-noise ratio measurements for SHG in dermis of pork skin at 25 pJ input pulse energy.

Technique	Contrast	Signal-to-noise ratio
Fundamental pulse	33.1±2.2	8.4±0.5
Chirped mirror only	60.1±3.0	9.2±0.5
MIIPS pulse	70.1±3.5	10.6±0.5
i^{2}PIE pulse	116.3±3.1	26.0±0.7

5.2.1.4 Estimation of thickness of Collagen fibrils

Collagen fibres are made of bundles of thread-like collagen fibrils. They possess high tensile strength and are grouped into many categories based on the molecular structure and constituents. The most common type of collagen fibrils in tissue is the Type I [35] which is mostly found in the dermis of skin, tendons, bones etc. and has a diameter ranging between 2-10 μm [151].

The thickness of the collagen fibres in the porcine dermis tissue was estimated by taking advantage of the high contrast attained with the use of i^{2}PIE compressed pulses.

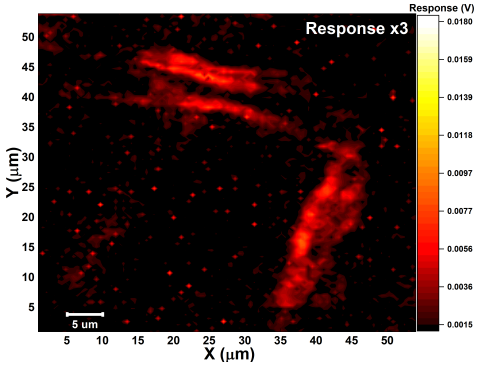

(a) SHG image using the fundamental pulse from the laser cavity.

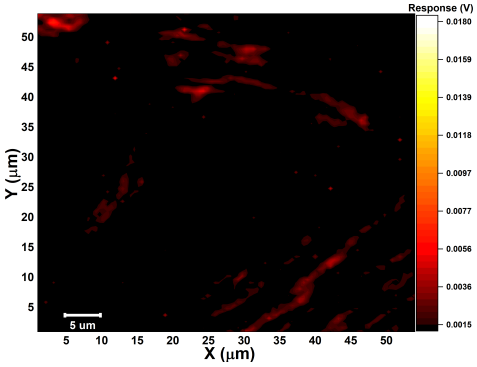

(b) SHG image with SC pulse compressed with only chirped mirrors.

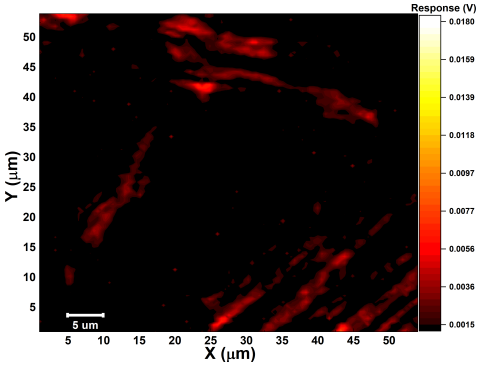

(c) SHG image with SC pulse compressed with CM and MIIPS.

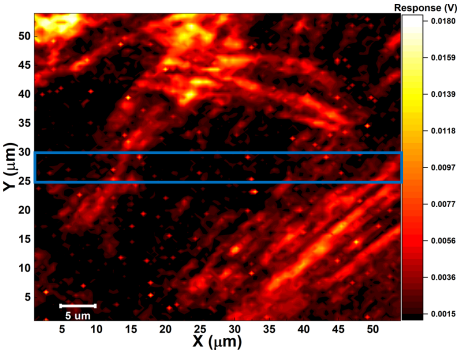

(d) SHG image with SC pulse compressed with CM and i^{2}PIE.

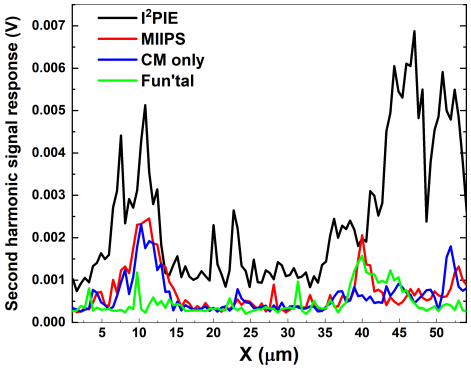

(e) Line scan profile plot of signal response along the ROI.

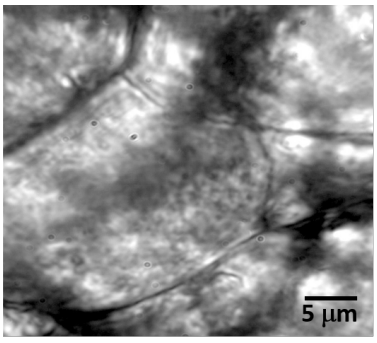

(f) Micrograph of dermis of pork skin tissue.

Figure 5.3: SHG images from dermis of porcine skin imaged under the four configurations: (a) fundamental laser (signal enhanced by a factor of 3), (b) SC with only chirped mirror (CM) compression, (c) SC with CM and MIIPS compression and (d) SC with CM and i^{2}PIE compression with ROI for line scans highlighted. All images were taken under the same conditions with a pulse energy of 25 pJ. (e) Line scan measurements of SHG signal response from dermis of porcine skin. (f) Bright field micrograph of tissue captured with the CMOS camera in the setup.

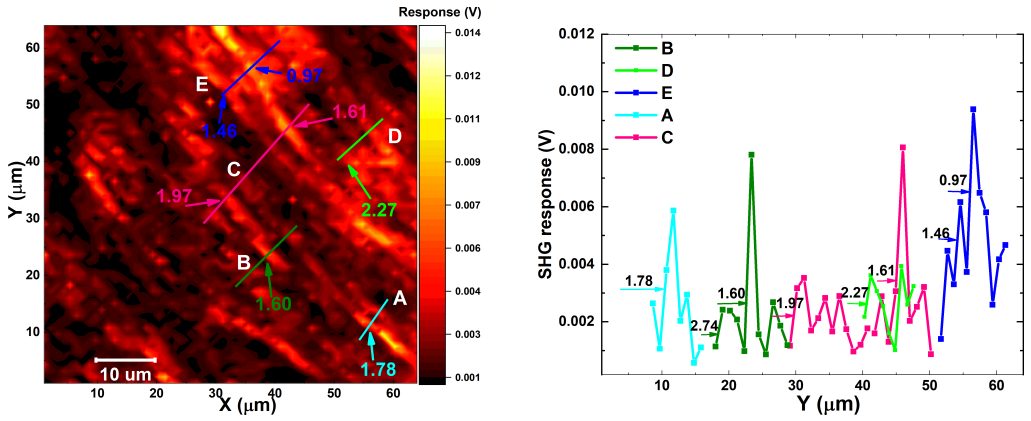

(a) SHG image of collagen with i^{2}PIE showing marked collagen

(b) Linear profiles of SHG response across selected collagen fibrils

Figure 5.4: (a) SHG scan image of collagen in dermis of porcine skin taken with i^{2}PIE showing fibres of interest. (b) Linear profiles of SHG response along the coloured lines in (a). The estimated thickness of the fibres (in μm) are indicated.

Figure 5.4a shows a SHG image recorded using an i^{2}PIE compressed pulse and with a scan step size of approximately 1 μm. Cross sectional profiles were taken across some of the fibres. The regions where these cross sectional profiles were taken are represented by lines A-E in figure 5.4a. The intensity profiles of the signal responses for the marked regions are plotted in figure 5.4b with the width of the peaks corresponding to the estimated diameters of the highlighted fibres. The average thickness of the fibres under consideration was determined to be (1.8±0.6) μm. This thickness is found to be within the lower range thickness of Type I fibres as stated by [151]. Considering the scan step size used, these measured thickness values correspond to an upper limit of what can be resolved within the chosen step sizes.

5.2.2 Second harmonic generation in plant cells

Plants possess cellulose as an essential component structural component of the cell walls [35]. The highly ordered structure of the cellulose makes them an ideal source of second harmonic generation signals and many studies have shown that SHG is strongly generated in plants cells [152–154]. The guard cells in plant stomata contains relatively well-developed chloroplasts [155] and are responsible for the opening and closing of the stomata for gaseous exchange. Examples of open and closed stomata are shown in figure 5.5. In the presence of sunlight, they open for transpiration and close in the absence of sunlight [156]. The guard cells vary in size and in our study we measured cells within the range of 30-70 μm in diameter. The chloroplasts are membrane bound organelles that are made up of other structures including starch granules and grana [157]. These starch and grana are highly crystallized structures and are therefore strong emitters of SHG [153, 157].

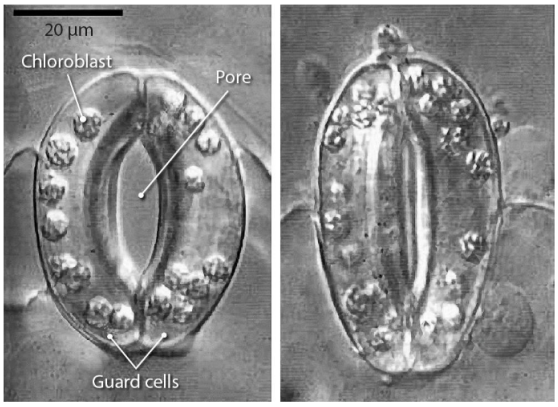

Figure 5.5: Micrograph of plant guard cell in the epidermis of leaves showing open (left) and closed (right) stomatal pore. The nature and location of the chloroplasts are also clearly highlighted. Image taken from [155].

5.2.2.1 Verification of Second harmonic generation in plant cells

Preliminary measurements were taken to confirm that it was second harmonic generation that was measured from chloroplasts upon irradiation using the fundamental pulse. For any nonlinear process, the intensity (I) of the signal response is directly proportional to the applied laser power (P) scaled to the order of the nonlinear process such that:

$$I = A + P^n \tag{5.2.1}$$

where A represents the signal offset/background noise and n is the order of the nonlinear process. Equation 5.2.1 can be rewritten in a linear form such that:

$$log(I) = log(A) + nlog(P) \tag{5.2.2}$$

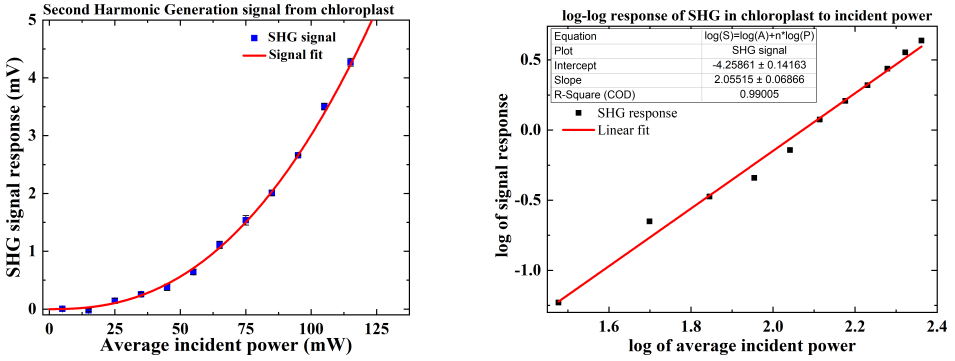

(a) Nonlinear signal response **(b)** log-log response

Figure 5.6: SHG signal generated from plant chloroplast of a potato leaf. Quadratic signal response recorded for varying average input power is shown in 5.6a. A log-log presentation showing the fit function is shown in 5.6b

Figure 5.6a shows the signal response recorded from the chloroplast as a function of irradiation power while figure 5.6b shows a log-log plot of the same data set. Fitting

figure 5.6a with equation 5.2.1 shows a quadratic response between the SHG signal response and the applied power.

This can be confirmed from the linear fit of figure 5.6b with equation 5.2.2 with a gradient of $n = 2$ corresponding to a second order nonlinear process. With the 630-800 nm fluorescence wavelength of chlorophyll [158, 159] beyond the range of the bandpass filter, this response can be attributed to a SHG response generation from the chloroplast. Plant leaves therefore served as a cheap, readily available sample to investigate in this project.

5.2.2.2 Second harmonic generation imaging in plant guard cells

To perform SHG imaging in plant cells with our constructed imaging systems, our test sample was obtained from the leaf of a sweet potato (*Ipomoea batatas*). A monolayer of the epidermis was excised and mounted between a cover slip and a microscope slide. Dehydration was reduced by placing the monolayer in a thin film of water. These guard cell samples were then imaged with SHG using pulses having been compressed with the different compressions techniques discussed, namely the chirped mirror compression, MIIPS compression and i^{2}PIE compression. Fluorescence was not considered in plant cells due to two main reasons: chloroplast absorbs in the lower wavelength region (360-410 nm) and has a red fluorescence spectrum ranging between 630 - 800 nm [158–160] which overlaps with the supercontinuum spectrum at maximum pumping power.

Figure 5.7 shows the SHG images obtained after scanning with the different compressed pulses at a higher pulse energy of 250 pJ. This higher pulse energy compared to that used on mammalian cells was chosen because plant cells are more robust than mammalian cells. The measured contrast and SNR values are listed in table 5.4 with the corresponding enhancement factors listed in table 5.5. Again, the SNR values are listed in parenthesis. It is observed that the values are relatively low compared to the readings recorded in the SHG in porcine epidermis tissues. The contrast and SNR values recorded are low because the contributions from the background regions of the cell. This background signal is probably due to the presence of other cellular structures in the cell which can contribute to SHG. The cell walls and chloroplasts however contain starch and grana which are highly crystallized and therefore lead to a production of stronger SHG responses [35, 157].

Table 5.4: Contrast and signal-to-noise ratio measurements for SHG in plant guard cells at 250 pJ input pulse energy.

Technique	Contrast	Signal-to-noise ratio
Fundamental pulse	16.4±2.8	4.7±0.8
Chirped mirror only	17.6±0.4	9.6±0.7
MIIPS pulse	20.8±0.9	12.5±0.5
i^{2}PIE pulse	29.6±2.7	16.8±1.5

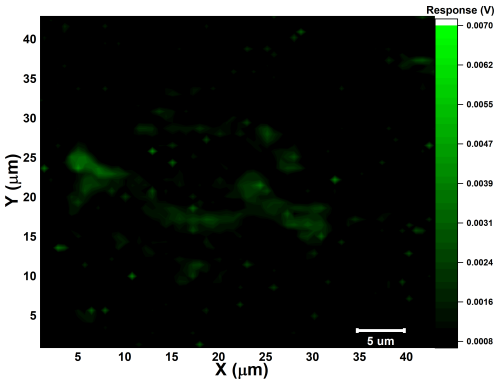

(a) SHG image using the fundamental pulse from the laser cavity.

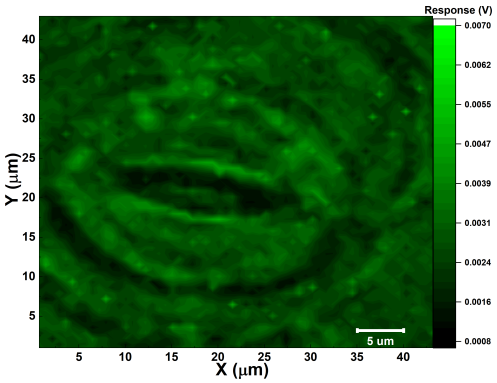

(b) SHG image with SC pulse compressed with only chirped mirrors.

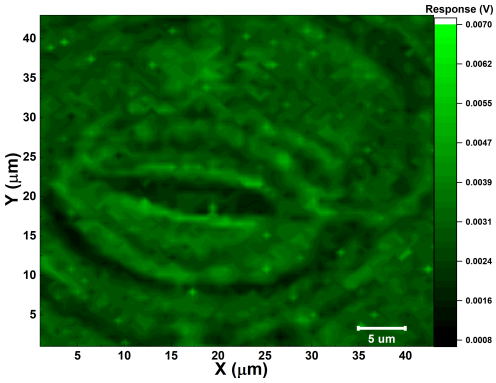

(c) SHG image with SC pulse compressed with CM and MIIPS.

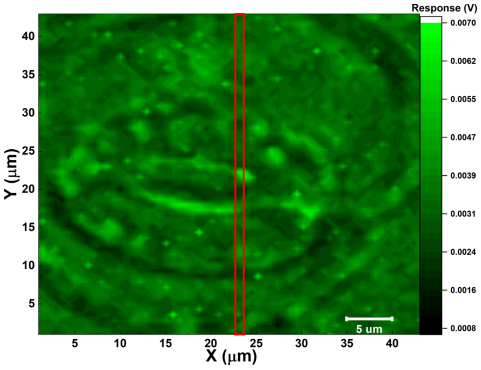

(d) SHG image with SC pulse compressed with CM and i^{2}PIE.

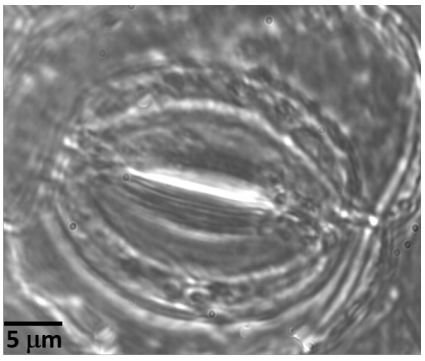

(e) Micrograph of guard cell taken with the CMOS camera.

Figure 5.7: SHG images from epidermis of leaf imaged under the four configurations: fundamental laser (a), SC with only chirped mirror (CM) compression (b), SC with CM and MIIPS compression (c) and SC with CM and i^{2}PIE compression (d). The micrograph image is shown in (e). All images taken under same conditions with pulse energy of 250 pJ (20 mW average power) with a scale bar of 5 μm.

Table 5.5: Contrast (SNR) enhancement factors for SHG in plant cells.

Technique	Fundamental	CM-only	MIIPS	i^{2}PIE
Fundamental	1.0	1.1 (2.0)	1.3 (2.6)	1.9 (3.4)
CM-only		1.0	1.2 (1.3)	1.7 (1.7)
MIIPS			1.0	1.4 (1.3)
i^{2}PIE				1.0

As expected, there is an increase in signal response when i^{2}PIE compressed pulses were used. It showed a contrast enhancement of almost 40% more than that obtained with MIIPS compressed pulses. For SNR, a 30% improvement was also recorded in favour of i^{2}PIE compressed pulses over the use of the MIIPS technique. Compared to the usage of CM-only compressed pulses and the fundamental pulse, i^{2}PIE can be seen to provide approximately 70% and 90% contrast enhancement respectively.

The line scan taken across the highlighted region in figure 5.7d is plotted in figure 5.8 showing the increase in contrast and SNR in i^{2}PIE over the other compression techniques. The higher contrast offered by the i^{2}PIE technique is made manifest in the level of details shown in figure 5.7d where the chloroplast are more visible compared to the level of details present in the images obtained with other compression techniques. The chloroplasts in figure 5.7d are visible in a manner similar to their display in figure 5.5.

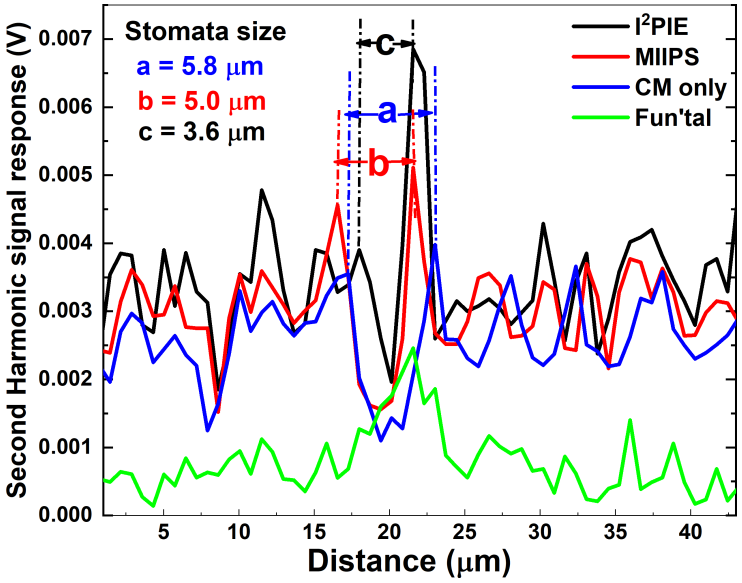

Figure 5.8: Profile of line section for signal response along the highlighted region of interest in figure 5.7d.

A key advantage of nonlinear microscopy is the ability to examine cells in their natural environment without interfering with their normal functions. This can be seen by observing the opening and closing of the guard cells, even whilst they are

being irradiated. The size of the stomata is represented in figure 5.8 by a, b and c. The size is estimated to be 5.8 μm, 5.0 μm and 3.8 μm for CM-only, MIIPS and i^{2}PIE respectively. As a reminder, the scanning order is CM-only, MIIPS before i^{2}PIE. There is therefore a decrease in the size over time. Considering that the measurements were performed in the total darkness and that the wavelength of the illuminating source lies outside the absorption spectrum of the chloroplasts one can assume that the stomata pore was closing due to the absence of sunlight. The size of the guard cell however remained the same thus eliminating the explanation that the reduction in pore size was as a result of cell shrinking. This supports the fact that there is a reduced risk of photodamage in nonlinear microscopy as cells were seen to be functioning normally throughout the investigation.

5.3 Two photon excitation fluorescence imaging

In general there are two categories of fluorescence imaging in biological samples irrespective of whether one or two photon processes are being considered. These are autofluorescence, originating from endogenous fluorophores, which is label-free and labelled or tagged fluorescence, where fluorophores are introduced into the sample. Measurements on both categories of fluorescence were taken with the system and are discussed below.

5.3.1 Autofluorescence in porcine skin

Label-free two photon excitation fluorescence (TPEF) imaging was performed on the same porcine epidermis sample used in the SHG imaging presented in section 5.2.1.1 above. Intrinsic fluorescence in type I collagen spans an emission wavelength of 300-500 nm [161] hence there is an overlap between the fluorescence and SHG emission wavelengths. Detection of TPE-autofluorescence signal was ensured by blocking SHG signals through the use of a 450/10 band pass filter (transmitting the band 450 nm $\pm$ 10 nm).

TPEF images recorded for all techniques are shown in figure 5.9. For illustrative purposes, the responses recorded with the fundamental in figure 5.9a and GDD-only compensated SC pulse (CM-only) in figure 5.9b have each been enhanced by a factor of 2. The signal response follow the same trend as that for SHG images with the highest contrast recorded for imaging with i^{2}PIE compressed pulse. TPEF fluorescence emission in epidermal skin tissue has been reported to span a broad spectral wavelength of 350 - 700 nm [29]. However, there are fluorescence contributions from different fluorophore such as NADH, keratin, melanin and porphyrins which all absorb at the same excitation wavelength and emit within the fluorescence emission window. For example, NADH, keratin, melanin and porphyrin are reported to have emission peaks at 470 nm, 500 nm, 575 nm and 618 nm respectively [29]. There is therefore a strong possibility that our recorded signals contain contributions from these other fluorophores in addition to that of the intrinsic fluorescence of collagenase I with a fluorescence emission range of 300 - 500 nm [161].

Table 5.6 lists the contrast and signal-to-noise ratios recorded for each technique with

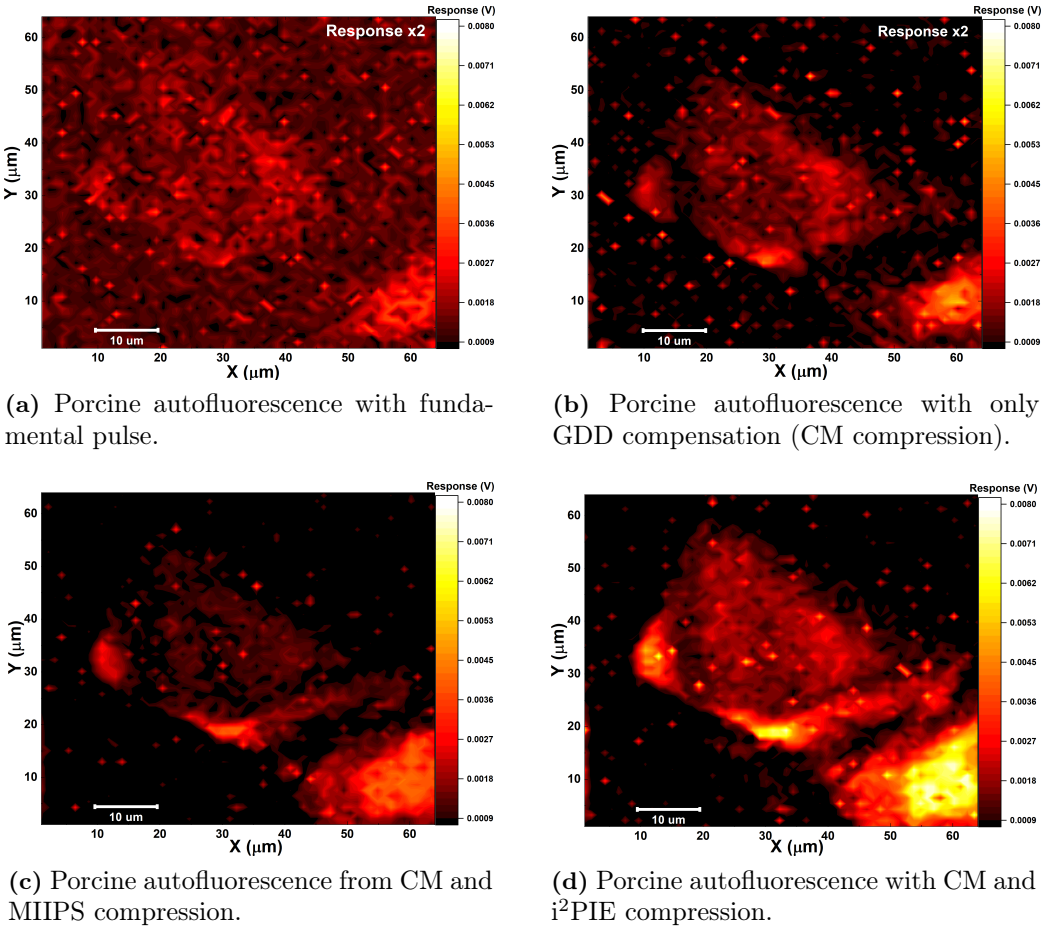

(a) Porcine autofluorescence with fundamental pulse.

(b) Porcine autofluorescence with only GDD compensation (CM compression).

(c) Porcine autofluorescence from CM and MIIPS compression.

(d) Porcine autofluorescence with CM and i^{2}PIE compression.

Figure 5.9: TPE autofluorescence from the epidermis of porcine skin imaged under the four configurations: fundamental laser (a), SC with only chirped mirror (CM) compression (b), SC with CM and MIIPS compression (c) and SC with CM and i^{2}PIE compression (d). Micrograph image is the same as that of figure 5.1e. All images taken under same conditions with pulse energy of 25 pJ.

the corresponding contrast (SNR) enhancement factors listed in table 5.7 Comparing the contrast and SNR values recorded for TPE-autofluorescence of the epidermal porcine tissue in table 5.7 to the values recorded in the SHG images of the same tissue in table 5.2, there is a stronger signal response in the SHG imaging than that of the TPEF. For example, a contrast enhancement factor of 7.8 fold was recorded when comparing the SHG signals obtained for CM-only compressed pulses with i^{2}PIE compressed pulse. For the same two techniques, the TPEF contrasts was enhanced by a factor of 2.8. The signals cannot be compared directly since they originate from two different nonlinear processes. However,the incoherence or isotropic nature in the emission of fluorescence signals contributes to low signal response in transmission detection geometry.

Table 5.6: Contrast and signal-to-noise ratio measurements for TPEF in epidermis of porcine skin at 25 pJ input pulse energy.

Technique	Contrast	Signal-to-noise ratio
Fundamental pulse	8.0±0.6	3.2±0.2
Chirped mirror only	12.1±1.4	4.1±0.4
MIIPS pulse	24.8±3.0	8.6±1.3
i^2PIE pulse	32.9±4.0	10.6±1.6

Table 5.7: Contrast (SNR) enhancement factors for TPEF in porcine epidermis.

Technique	Fundamental	CM-only	MIIPS	i^2PIE
Fundamental	1.0	1.5 (1.3)	3.1 (2.9)	4.1 (3.7)
CM-only		1.0	2.1 (2.3)	2.8 (2.8)
MIIPS			1.0	1.3 (1.2)
i^2PIE				1.0

5.3.2 Exogenous TPEF

The system's ability to detect exogenous fluorophore induced TPEF in cells was investigated using fix cultured mouse hypothalamic neuronal cell line (GT1-7 cells) obtained from the Neuro Research Group, Department of Physiological Sciences, Stellenbosch University. These cell lines are commercially available and are reported to be an excellent model system in the investigation of endocrine disruption and neurotoxicity [162]. The GT1-7 cells were patterned onto a microscope slide and stained with Hoechst dye. Hoechst is a fluorescent stain which absorbs within the ultraviolet region of the electromagnetic spectrum around 350 nm and emits with a maximum wavelength around 450 nm and is predominantly used for labelling DNA. Since the DNA is localized in the nuclei, this dye is used mostly to visualize the nucleus. It is more lipophilic due to its structure making it cross intact cell membranes readily [163]. Absorption and emission spectra are shown in figure 5.10[1] alongside the excitation pulses.

From the absorption spectrum in figure 5.10, hoechst stain has an excitation efficiency of about 8% at a two photon absorption (TPA) wavelength of 400 nm. To maximise excitation efficiency, the central wavelength of the laser was tuned from 800 nm to 780 nm which is close to the lower limit for stable mode-locking of the laser. The fundamental and SC spectra recorded when the laser was tuned is represented by their respective plots in figure 5.10. It can be observed that the SC spectrum shifts to shorter wavelengths spanning from approximately 690 - 830 nm. This ultimately also lowers TPA wavelength. With a TPA wavelength at 390 nm, an excitation efficiency of about 15% is achieved. Imaging was carried out with an input energy of 25 pJ (2 mW average power). A 360-580 nm band pass filter was used to block the incident laser light with detection performed in transmission geometry.

[1]Spectra data courtesy Fluorescence SpectraViewer from www.thermofisher.com

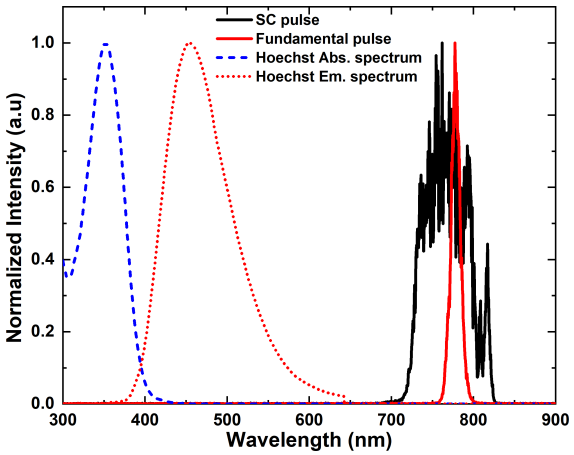

Figure 5.10: The absorption and emission spectra of Hoechst stain are shown in the blue and dotted red lines respectively (spectral data from www.thermofisher.com). The solid red and black lines respectively represent the excitation spectra for the fundamental and SC pulses used for the exogenous TPEF imaging.

Figure 5.11 displays the results obtained from the TPEF imaging. Again, response obtained for the fundamental pulse has been enhanced by a factor of 2 for illustrative purposes. As with previous reported results (for SHG and endogenous TPEF), there is an increase in signal response in the use of SC pulses with the best image achieved through the use of i^{2}PIE. The calculated contrast and signal to noise readings are tabulated in table 5.8. It can be seen that there is approximately a 2 fold increase in the contrast and SNR recorded images taken with i^{2}PIE compressed pulses than that recorded for MIIPS compressed pulses. Our results of exogenous TPEF of labelled

Table 5.8: Contrast and signal-to-noise ratio measurements for TPEF in GT1-7 Cell Line at 25 pJ input pulse energy.

Technique	Contrast	Signal-to-noise ratio
Fundamental pulse	19.2±2.4	8.2±1.0
Chirped mirror only	40.9±8.7	13.5±2.9
MIIPS pulse	44.2±3.2	15.3±1.1
i^{2}PIE pulse	83.7±9.3	30.0±3.2

cells also show better contrast and SNR recorded with the use of i^{2}PIE as a pulse compression technique compared to the other compression techniques. The obtained results imply that the excitation pulse energy can further be reduced for the i^{2}PIE technique and still generate signal responses comparable with that of MIIPS. This is very crucial especially for mammalian cells since high pulse energies can lead to photodamage.

The results obtained from the GT1-7 cell lines show a clear distinction between the stained nuclei and the background as can be observed from figure 5.11. The zero background in the exogenous TPEF highlights the advantage of labelling in

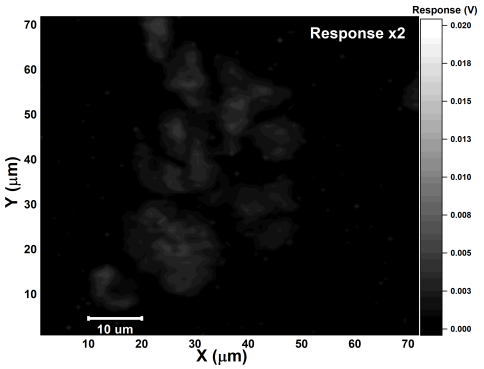

(a) TPEF image using the fundamental pulse from the laser cavity.

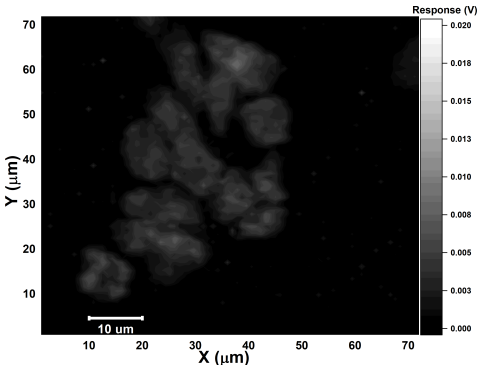

(b) TPEF image with SC pulse compressed with only chirped mirrors.

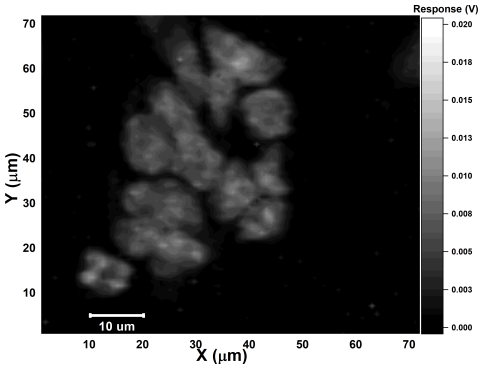

(c) TPEF image with SC pulse compressed with CM and MIIPS.

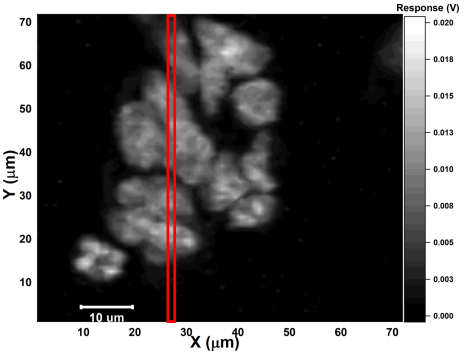

(d) TPEF image with SC pulse compressed with CM and i^{2}PIE.

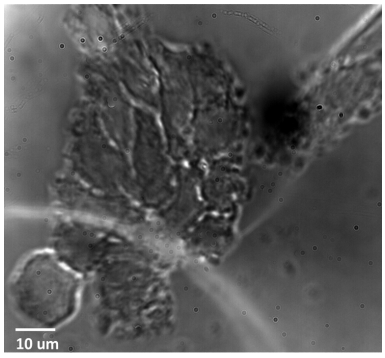

(e) Micrograph of hoechst stained cells.

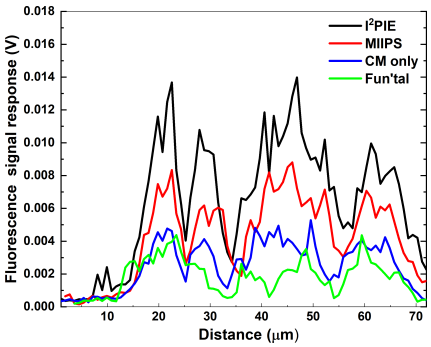

(f) Line scan profile of signal response.

Figure 5.11: TPEF images from hoechst stained cells imaged under the four configurations: fundamental laser (a), SC with only chirped mirror (CM) compression (b), SC with CM and MIIPS compression (c) and SC with CM and i^{2}PIE compression (d). All images taken under same conditions with pulse energy of 25 pJ. Micrograph of cell shown in (e) with a line scan of response across highlighted region in figure 5.11d displayed in (f). For representation purposes, the signal response for the fundamental has been amplified by a factor of 2.

microscopy as localization of fluorophores permits the generation of responses from only the regions of interest. he exogenous fluorophores can however interfere with cell morphology and functions.

5.4 Chapter summary

This chapter has been used to present and discuss the biophotonic applications of the different phase measurement/pulse compression techniques that were used in our constructed nonlinear microscope. Two main second order nonlinear imaging techniques i.e. two photon excitation fluorescence and second harmonic generation were investigated. For TPEF, both intrinsic (autofluorescence) and exogenous fluorescence were considered while label free SHG imaging was also investigated in both plant and mammalian samples.

It has been established that in all modalities considered, there was greater contrast and signal-to-noise ratios achieved with the use of i^{2}PIE when compared to pulses compressed using other phase measurement and compression techniques. Even at low pulse energies, i^{2}PIE has proven to provide higher signal responses in both endogenous and exogenous nonlinear imaging. Thus the new i^{2}PIE serves as a better phase measurement/pulse compression technique than any other existing technique for live cell imaging as the risk of photodamage is drastically reduced. It has also been shown from analysis of SHG in plant cells that the morphology and normal functioning of cells are not affected. This makes i^{2}PIE a much better coherent phase control alternative in imaging conditions that require irradiation with low energy pulses but demand higher contrast and improved signal-to-noise ratios.

Chapter 6

Summary, conclusions and future outlook

6.1 Summary and conclusions

A dedicated and versatile nonlinear optical laser scanning microscope has been successfully designed and constructed. The constructed system is based on the application of a broadband supercontinuum (SC) pulse generated from a novel experimental polarization-maintaining all-normal dispersion photonic crystal fibre (PM-PCF). The use of this SC pulse provided the opportunity to control the laser pulse in order to generate ultrashort pulses with durations shorter than the duration exiting the oscillator. These pulses provide the high intensities required to perform nonlinear microscopy with low energy pulses. A 4f shaper with a spatial light modulator integrated into the setup was used to measure the phase of the SC pulse and also used in pulse compression by applying a negative of the measured phase onto the SLM.

In measuring the spectral phase, a new technique that utilizes time domain ptychographic phase measurement was applied. This technique is known as i^{2}PIE and this work is the first ever application of this phase measurement technique, that can be used for pulse compression, to microscopy. This work explored the features and merits of this novel technique in comparison to the well established MIIPS technique which is used for the same purpose. The phase measurement process of both i^{2}PIE and MIIPS and how the two algorithms perform as pulse compression techniques were investigated. Accurate and effective pulse compression to near transform limited pulse is necessary for the generation of high intensity pulse in the plane of the object. The characteristic features of the constructed microscope were investigated using four different irradiation sources: the fundamental pulse directly from the oscillator; SC pulse that was only pre-compressed with chirped mirrors; SC pulses compressed with the phase measured with MIIPS and SC pulses compressed with the phase measured with the new i^{2}PIE technique. Finally, the influence of these four irradiation sources on contrast and signal-to-noise enhancement was investigated by performing second harmonic generation (SHG) and two photon excitation fluorescence (TPEF) microscopy with the constructed system.

The constructed microscope provides the unique opportunity to measure and correct spectral phase distortions within the same setup. The phase measurement and correction happens at the position of the object and therefore any additional phase introduced by new optics in the beam bath is accurately measured and corrected to provide near transform limited pulses. The collinear beam geometry reduces alignment challenges and therefore make the constructed system more user friendly especially for non-laser experts. The system is also inherently confocal and therefore excitation only occurs at the focus of the microscope objective thus the risks of photodamage to samples is significantly reduced.

In relation to the SC generation in the PCF, the PM-PCF has been observed to provide a higher degree of confinement when propagating along a chosen axis thus providing a more stable supercontinuum spectrum than the non-PM-PCF. This high confinement is attributed to the intentional stress induced in the fibre during fabrication which reduces transfer of power between orthogonal axes. Our results support the findings of [111] who provided the theoretical framework in support of PM-PCFs.

In our comparative analysis, we have demonstrated the key features and merits of i^{2}PIE over the standard MIIPS as a phase measurement technique that can be used for pulse compression. i^{2}PIE has been shown to provide a more accurate measure of the spectral phase of the SC pulse. It is more sensitive to the complex spectral profile of the pulse and is able to compensate for higher order dispersion which is a known limitation of the standard MIIPS, where compensation is limited to second order dispersions. The higher accuracy of the measured phase allows for better pulse compression and hence the generation of pulses with a shorter temporal duration closer to the transform limited case. These shorter pulse durations also generate higher peak intensities. With nonlinear signal responses depending on the intensity of the applied field, higher peak intensities generate higher signal responses. Our in-house developed i^{2}PIE technique has been shown to provide higher signal responses with greater contrast and signal-to-noise ratios than other measurement techniques for the same input pulse energy. In SHG in crystals, the results obtained from this dissertation suggests that pulses compressed with i^{2}PIE exhibit a more accurate phase matching between the phase of the pulse and the dipoles in the crystalline medium. This also contributes to higher signal responses. Due to the higher nonlinear signal responses from i^{2}PIE, lesser average power (pulse energy) can be used. This leads to a lesser risk of photodamage in tissue. Again, in terms of processing time, the non-iterative reconstruction nature of i^{2}PIE makes it a faster compression method than MIIPS. The ptychographic nature of i^{2}PIE also provides the added advantage of pulse amplitude reconstruction which is another limitation of the standard MIIPS algorithm.

The first ever application of i^{2}PIE as a pulse characterization technique in SHG and TPEF microscopy has been very successful and shows excellent results. In all specimen investigated (both plant cells and mammalian cells/tissues), i^{2}PIE been proven to provide higher contrast and signal-to-noise ratios at the same input pulse energy than the other pulse characterization techniques investigated. It provides higher peak intensities which generate stronger signal response. This means when compared to other techniques, i^{2}PIE can easily be used with very low energy pulses and

still provide significant results. The inherent confocality associated with nonlinear microscopy is also evident in the fact that sample morphology and physiology were not affected as can be seen from the SHG imaging of the plant guard cells where the stomata was observed to be closing over time in response to the ambient conditions in the laboratory.

Based on the results obtained in this dissertation, i^{2}PIE has been proven to be a more accurate phase measurement/pulse compression technique than the other pulse characterization techniques including the commonly used multiphoton intrapulse interference phase scan (MIIPS).

6.2 Future outlook

This dissertation has introduced a new ultrashort phase measurement technique that can be used for pulse compression. Although this work focused on applications into two photon microscopy processes, the new i^{2}PIE technique can be further explored in other microscopy spectroscopy applications. There are also avenues to further explore its phase measurement features and merits.

As a phase measurement technique, a comparative study between i^{2}PIE and the gated-MIIPS (G-MIIPS) can be explored. G-MIIPS is a modification of the standard MIIPS designed to address some of the key limitations of standard MIIPS [67]. It also offers both phase and amplitude modulation and therefore a comparative study of these two techniques can provide further details and deeper understanding into their individual features and advantages. Again, polarization-resolved spectroscopic measurements are also worth exploring to determine the polarization dependent compression efficiency.

Fluorescence signals are known to be better collected with high NA microscope objectives thus often detected in the reflection (epi) geometry. We have designed and optimized our system for epi detection and will be investigating the strength of these coherent control techniques in that detection geometry. 3D imaging will also be explored to determine the sectioning capabilities of the i^{2}PIE technique. This work focused primarily on second order nonlinear processes i.e. TPEF and SHG. Applications of i^{2}PIE in three-photon microscopy are worth exploring. To generate third harmonic generation responses in the ultraviolet region, the PCF should be pumped at wavelengths above 1 μm (1000 nm). Considering the fact that the dispersion profile of the fibre used in this work (refer to figure 2.6c in second chapter), would not permit all normal dispersion at pump wavelengths above 950 nm, and laser mode-locking challenges at wavelength above 820 nm, third order nonlinear processes such as three photon fluorescence and third harmonic generation could not be explored hence our limitations to TPEF and SHG. However, i^{2}PIE applications in three-photon microscopy can be explored with other novel PM-PCFs such as the NL-1050-NE-PM (NKT-Photonics) which are designed to offer complete all normal dispersion into the infrared wavelengths [164]. Its applications in CARS is however currently on-going in our laboratory with its application in single beam CARS being investigated.

Appendix A

Supplementary details

A.1 Time Bandwidth Product

For a Gaussian pulse, the frequency dependant electric field

$$E(\omega) = A_0 \int_{-\infty}^{+\infty} e^{-4\ln 2(\frac{t}{\tau})^2 + i(\omega_0 - \omega)t} dt \tag{A.1.1}$$

where τ is the temporal FWHM. This can be reduced to

$$E(\omega) = B_0 e^{-(\frac{\omega-\omega_0}{\Delta\omega_0})^2} \tag{A.1.2}$$

with $B_0 = A_0\tau\sqrt{(\pi/4\ln 2)}$ and $\Delta\omega_0 = 4\sqrt{\ln 2}/\tau$. Spectral FWHM ($S(\omega)$) is given by $\Delta\omega_0\sqrt{2\ln 2}$ which results in the time-bandwidth product (TB):

$$\begin{aligned} \Delta t \cdot \Delta\omega &= \frac{\tau}{\sqrt{2}} \cdot \Delta\omega_0\sqrt{2\ln 2} \\ &= \frac{\tau}{\sqrt{2}} \cdot \frac{4\sqrt{\ln 2}}{\tau}\sqrt{2\ln 2} \\ \Delta t \cdot \Delta\omega &= 4\ln 2 \end{aligned} \tag{A.1.3}$$

With $\omega = 2\pi\nu$, A.1.3 simplifies to (for a Gaussian pulse)

$$\Delta t \cdot \Delta\nu \approx 0.441 \tag{A.1.4}$$

Equation A.1.4 shows that for any Gaussian pulse, there is a fixed inverse relation between the spectral width and the temporal duration.

A.2 Spectral phases measured with MIIPS and i^{2}PIE

The graphs plotted here show supplementary spectral phases measured with MIIPS and i^{2}PIE.

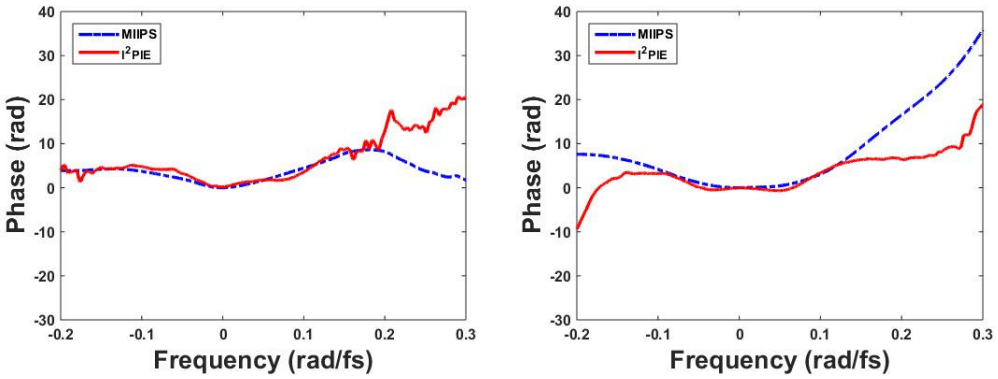

(a) supplimentary phase set 1

(b) supplimentary phase set 2

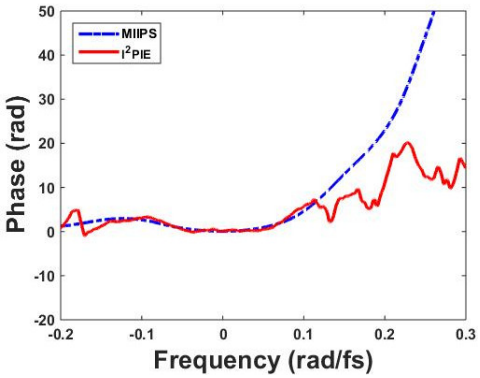

(c) supplimentary phase set 3

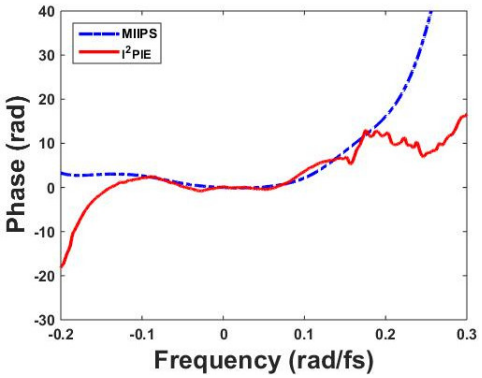

(d) supplimentary phase set 4

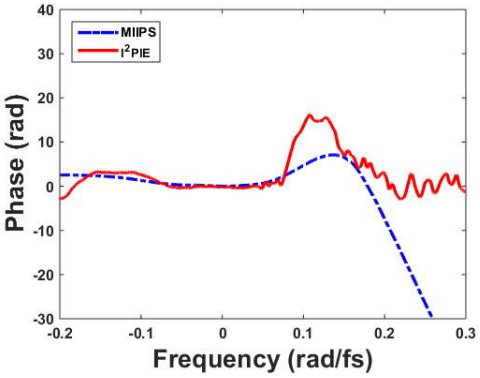

(e) supplimentary phase set 5

Figure A.1: Supplementary data for the comparison of measured spectral phase recorded with MIIPS and i^{2}PIE.

Appendix B

Labview codes

This appendix shows the user interfaces of the LabVIEW codes that were developed as part of this work. All codes were developed from scratch and not a modification of any pre-existing code.

B.1 Pulse duration calculation for the fundamental pulse

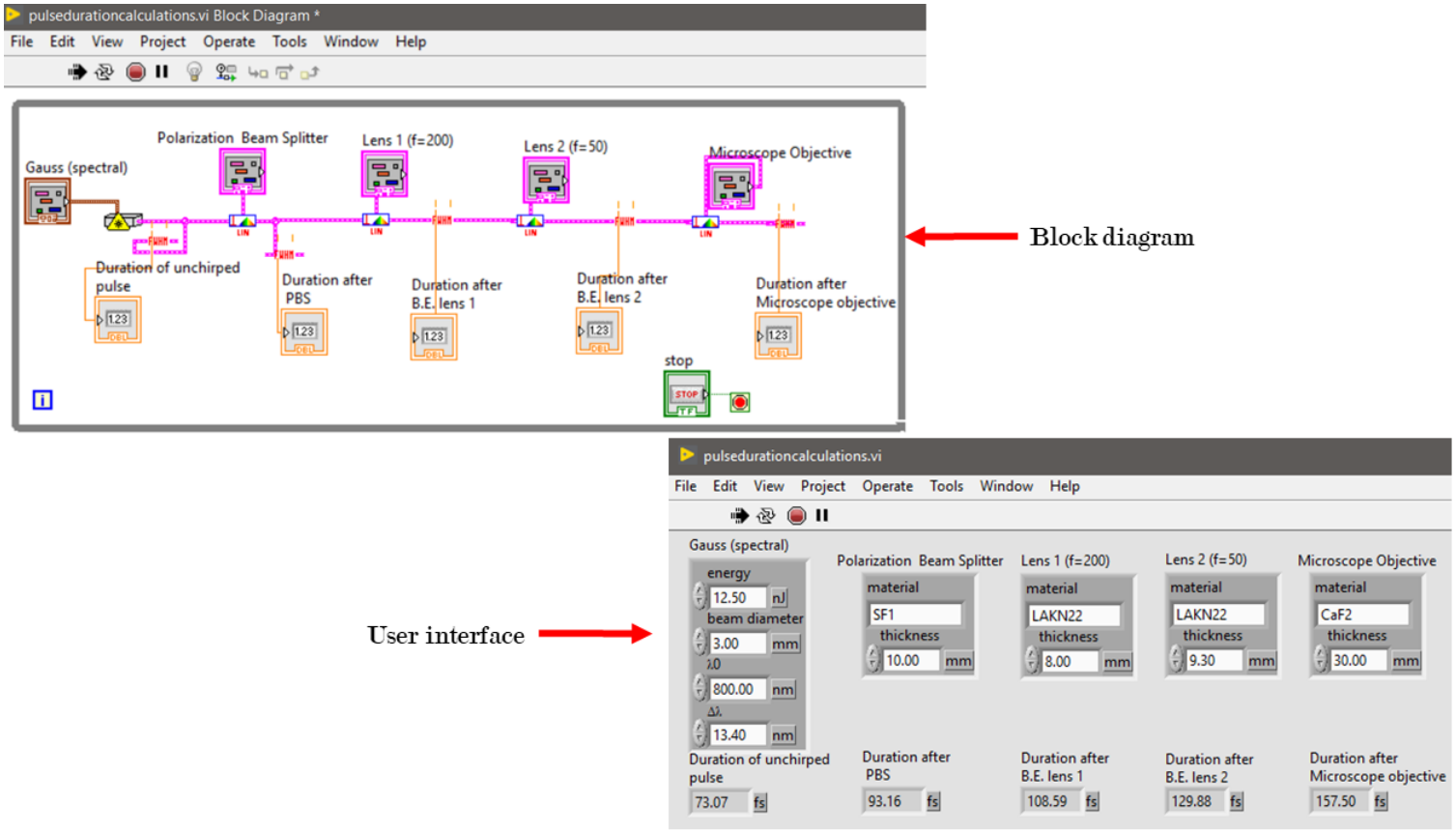

Figure B.1: Labview code and interface for estimating pulse duration of the fundamental pulse using Lab2. The block diagram is displaced on top and the user interface is displayed at the bottom.

B.2 Custom-built LabVIEW program for data acquisition

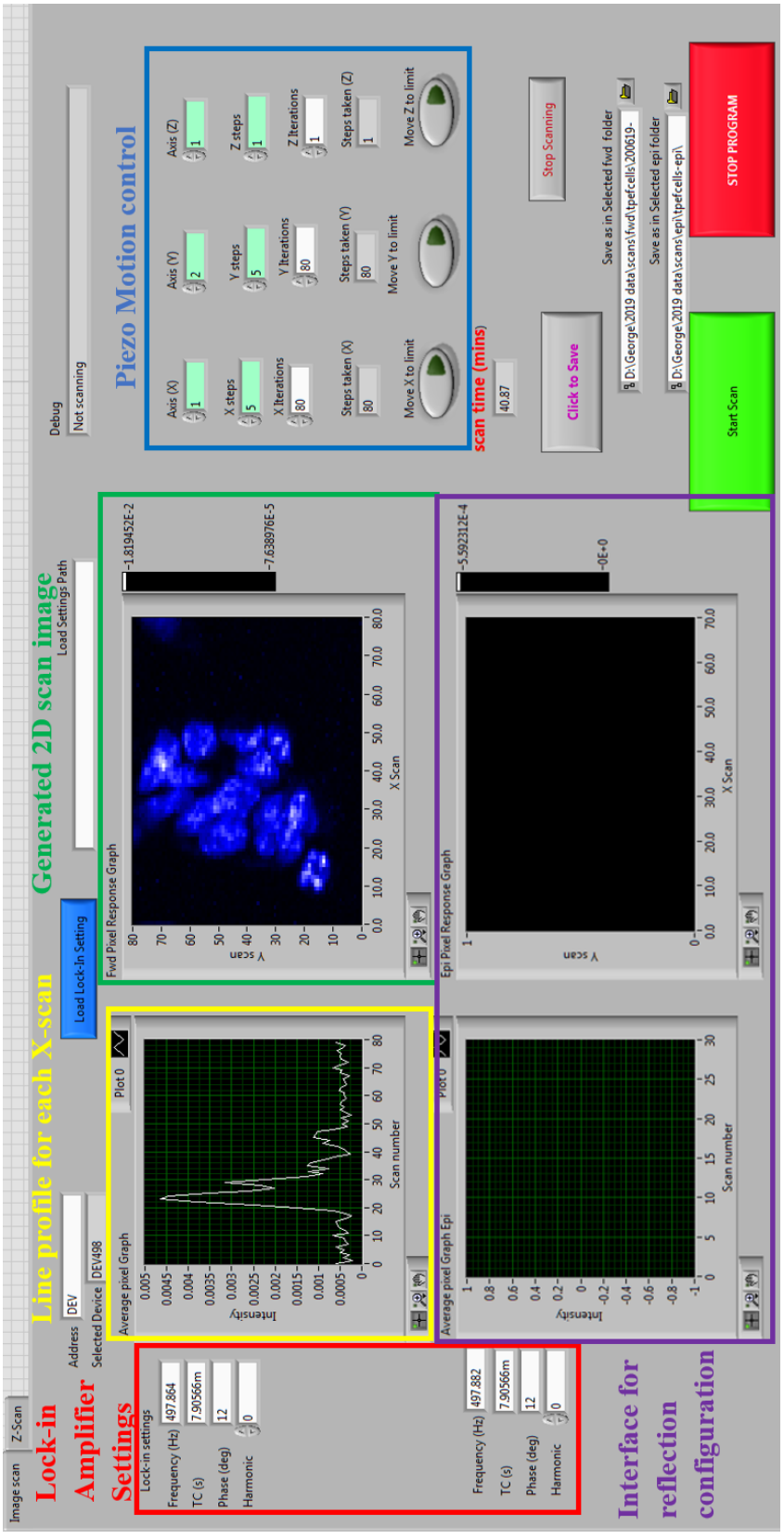

Figure B.2: User interface of custom-built Labview program for data acquisition. Highlighted are the sections for motion control, Lock-in amplifier settings and signal response displays. The upper and bottom rows display signal responses detected in transmission and reflection geometries respectively. Data was collected in transmission only.

Appendix C

Matlab codes

This appendix shows the Matlab codes that were developed as part of this work. All codes were developed from scratch and not a modification of any pre-existing code.

C.1 MIIPS analysis code

This code analyzes the second harmonic trace and the residual phase recorded by MIIPS for each iteration. ,

```
function [ output_args ] = process_miips( dirr , wc)
%%%This code analyzes the MIIPS data recorded. It analyzes
    the SH trace...
%%and retrieved phase per iteration
dirr = 'D:\ProBook data\Documents Drive C\SA PhD folder\
   Lab Data\2019 data\Year 4\data for thesis\120619\miips'
   ;    %lists all files in the MIIPS research directory

%%%%%%%Load data files from dirr given%%%%%
res_phase = dir([dirr '\residual']);  %%This is the phase
   correction per iteration
total_phase = dir([dirr '\total']); %% This is the total
   phase left on the pulse after each iteration
trace = dir([dirr '\trace']); %%This is the SH trace per
   iteration
ax = importdata([dirr '\ax.txt']); % the wavelength range
   of the blue spectrum (SHG signal)
rspec = importdata([dirr '\redspec_100nm_band_789.txt']);%
    replace with the red wavelength file of the laser
   power
lamb = importdata([dirr '\lambda.txt']); %resolution of
   the spectrometer

%%%% red spectrum
figure(2)
```

```
plot(rspec(:,2),rspec(:,1)/max(rspec(:,1)),'r','LineWidth'
    ,2);
axis([700 900 0 1])
set(gca,'Ydir','Normal','Fontsize', 12,'FontWeight','bold'
    )
set(gca,'Xdir','Normal','Fontsize', 12,'FontWeight','bold'
    )
xlabel('Wavelength (nm)', 'FontSize',20);
ylabel('Normalized intensity (a.u)', 'FontSize',20);

%%%%%Resample the blue spectrum to 2048 data points for
    miips traces
new_ax = linspace(-1024,1024,2048); %create a linear array
     starting from -1024 to 1024 with 2048 points
bf = abs(ax(1)-ax(length(ax)))/2048; %figure out spacing
    between each point for new axis
new_ax = new_ax.*bf;% new linear array with points at each
     line spacing.
wc =793; %center wavelength that is read on the R_MIIPS2
    screen
bc=wc/2;%Center wavelength for blue (don't think so)
new_ax = new_ax +bc;
delta = linspace(-2*pi,2*pi,256);

%%%%%trace prints
for i = 1:(length(trace)-2)
    figure(1)
    traces{i} = importdata([dirr '\trace\' trace(i+2).name
        ]);
    imagesc(delta,new_ax,traces{i}');
    set(gca,'Ydir','Normal','Fontsize', 12,'FontWeight','
        bold')
     set(gca,'Xdir','Normal','Fontsize', 12,'FontWeight','
         bold')
    ylabel('Wavelength (nm)','Fontsize',20)
    xlabel('\delta (rad)','Fontsize',20)
    axis([-2*pi 2*pi 330 450]);
    a=0;
%     pause;
end

%%%Make corresponding frequency axis for lamb
c = 2.998*10^8;
fc = 2*pi*c/(wc*10^-9);
fexp = 2*pi*c./(lamb*10^-9);
df = abs(fexp(1)-fexp(length(fexp)))/2048 ;
dt = pi/(2048*df);% 2* in front of pi deleted
```

```
tn = 3648;
t = dt*linspace(-tn/2,tn/2-1,tn);
f = df*linspace(-tn/2,tn/2-1,tn);

resample =interp1(rspec(:,2),rspec(:,1),lamb,'spline',0);%
   redefining the data point to make the spacing closer
resample = resample/max(resample); %normalizing the
   resampled data

ind = find(abs(resample)/max(abs(resample)) > 0.01); %
   changing resample to rspec
err=0;

%%%%Plot phase functions from file
for i = 1:(length(res_phase)-2)
   figure(3)
   rp{i} = importdata([dirr '\residual\' res_phase(i+2).
      name]);
   tp{i} = importdata([dirr '\total\' total_phase(i+2).
      name]);

   [AX1,H11, H12]=plotyy(lamb,resample,lamb,[rp{i}' tp{i
      }']); %%plotting a yy plot for the phases
   set(AX1(1),'ylim',[0 1],'FontWeight','bold')
   set(AX1(2),'ylim',[-1 5],'ytick',-1:1:5, 'FontWeight','
      bold');%%
   set(AX1(1),'xlim',[700 900])
   set(AX1(2),'xlim',[700 900])
   set(H11,'LineWidth',2);
   set(H12,'LineWidth',2);
   title(res_phase(i+2).name);
   xlabel('Wavelength (nm)','Fontsize',20)
   set(get(AX1(1),'Ylabel'),'String','Intensity (a.u.)','
      Fontsize',20);
   set(get(AX1(2),'Ylabel'),'String','Phase (rad)','
      Fontsize',20);
%  pause;
   a=0;
end

%%%%%Plotting error in phase reconstruction
figure(6);
   phase = rp{i}(ind(1):ind(length(ind)));
   nr = length(phase);
   err(i) = sum(abs(phase))/nr; %calculating the error in
      the phase reconstruction;
   plot(err,'b','LineWidth',2.5);
```

```
    axis([1 10 0 inf]);
    set(gca,'Fontsize', 13,'FontWeight','bold')
    set(gca,'Fontsize', 13,'FontWeight','bold')
    xlabel('Iteration #', 'FontSize',20);
    ylabel('Error in measured phase(a.u.)', 'FontSize',18);
a=0;
end
```

C.2 Phase analysis code

This code analyzes the spectral phase measured with MIIPS and i^{2}PIE. ,

```
clear all;
close all;
%%%Phase reading parameters
red=dlmread('redspec200519.txt'); %% loads the SC spectrum
miips=dlmread('miipsphase.txt'); %% loads the MIIPS
    retrieved phase
pty=dlmread('SA_779.00_pty2.txt'); %% loads the IIPIE
    retrieved phase
w_cal=dlmread('wl.txt'); %% loads the wavelength range
    from the calibration file

%%%Redspec data
red_y=red(:,1);%intensity axis
red_x=red(:,2); %wavelength axis

figure(1);
plot(red_x,((red_y)-min(red_y))/max(red_y),'r','LineWidth'
    ,2);
axis([650 950 0 1])
set(gca,'Ydir','Normal','Fontsize', 12,'FontWeight','bold'
    )
set(gca,'Xdir','Normal','Fontsize', 12,'FontWeight','bold'
    )
xlabel('Wavelength (nm)', 'FontSize',20);
ylabel('Normalized intensity (a.u)', 'FontSize',20);

%%%Make corresponding frequency axis
c = 2.998*10^8;
wc =779; %center wavelength that is read on the R_MIIPS2
    screen
int1 = sqrt(red_y); %amplitude of pulse
s = nrm(red_y)-7e-3;
I = find(s<0);
s(I) = 0;
```

```
i = find(int1/max(int1) > 0.02); %amplidute threshold
    determination
int2 = int1(i(1):i(length(i)));
wexp1 = red_x;
wexp2 = wexp1(i(1):i(length(i)));
fc = 2*pi*c/(wc*10^-9);
fexp = 2*pi*c./(wexp2*10^-9);

%%%Interpolation of SC pulse
tn=2^14; %number of data points
df = abs(fexp(1)-fexp(length(fexp)))/tn ;
dt = 2*pi/(tn*df);% defining time from frequency
t = dt*linspace(-tn/2,tn/2-1,tn);
f = df*linspace(-tn/2,tn/2-1,tn);
re =interp1(fexp,int1,f+fc,'spline',0);%resampling the
    data point to make the spacing closer
tp= t.*10^15;%%%converts axis to femtoseconds

% %%% Taking parameters of the SC pulse

figure(2)
plot(f.*1e-15,re,'LineWidth',2); %plotting redspec around
    the central frequency

%%%Determining autocorrelation of redspec
autocor_x=red_x/2;
blue=(abs(fftshift(ifft(fftshift(ifftshift(fft(ifftshift(
    sqrt(y)))).^2)))).^2);
nrm_blue=blue/max(blue);
figure(4)
plot(autocor_x,nrm_blue);
axis([300 500 0 1])
set(gca,'Ydir','Normal','Fontsize',12,'FontWeight','bold')
set(gca,'Xdir','Normal','Fontsize',12,'FontWeight','bold')
xlabel('Wavelength (nm)','Fontsize', 18,'FontWeight','bold
    ')
ylabel('Correlation Intensity (a.u.)','FontSize', 18,'
    FontWeight','bold');
title('Autocorrelation of Supercontinuum pulse','Fontsize'
    , 12,'FontWeight','bold')
% %

%%% ANALYZING MIIPS DATA
miips_y=miips(:,2);%intensity axis
miips_x=miips(:,1); %wavelength axis
f_miips = 2*pi*c./(miips_x*10^-9);
```

```
%%%Interpolation of MIIPS phase
df_mp = abs(f_miips(1)-f_miips(length(f_miips)))/tn ;
dt_mp = 2*pi/(tn*df_mp);% defining time from frequency
t_mp = dt*linspace(-tn/2,tn/2-1,tn);
F_mp = df_mp*linspace(-tn/2,tn/2-1,tn);
tp_mp= t_mp.*10^15;%%%converts axis to femtoseconds
re_mp =interp1(f_miips,miips_y,F_mp+fc,'spline',0);%
   resampling the data point to make the spacing closer

figure(3)
plot(F_mp,re_mp); %Plotting the MIIPS phase about the
   central frequency


%%%  ANALYZING IIPIE DATA
f_pty = 2*pi*c./(w_cal*10^-9);
Pty_x=f_pty;
Pty_y=pty;

%%%Interpolation of IIPIE phase
df_pty = abs(Pty_x(1)-Pty_x(length(Pty_x)))/tn ;
dt_pty = 2*pi/(tn*df_pty);% defining time from frequency
t_pty = dt*linspace(-tn/2,tn/2-1,tn);
F_pty = df_pty*linspace(-tn/2,tn/2-1,tn);
tp_pty= t_pty.*10^15;%%%converts axis to femtoseconds
re_pty =interp1(f_pty,pty,F_pty+fc,'spline',0);%resampling
    the data point to make the spacing closer
figure(4)
plot(F_pty,re_pty);

%%%Plotting the MIIPS and IIPIE phases over the SC
   spectrum
%%%MIIPS
figure(5)
[AX1,H11,H12]=plotyy(f.*1e-15,re/max(re),F_mp.*1e-15,re_mp
   );
 set(AX1(1),'ylim',[0 1],'ycolor','k','Fontsize', 12,'
    FontWeight','bold')
 set(AX1(2),'ylim',[-20 80], 'ytick',-20:10:80,'ycolor','b
    ','Fontsize', 12,'FontWeight','bold');
 set(AX1(1),'xlim',[-0.4 0.4],'FontWeight','bold')% axis
    in fs
 set(AX1(2),'xlim',[-0.4 0.4],'FontWeight','bold')
 set(H11,'LineWidth',3,'color','k');
 set(H12,'LineWidth',3,'color','b');
xlabel('Frequency (rad/fs)','Fontsize',18,'FontWeight','
   bold')
```

```
set(get(AX1(1),'Ylabel'),'String','Normalized intensity (a
    .u.)','Fontsize',18,'FontWeight','bold');
set(get(AX1(2),'Ylabel'),'String','MIIPS Phase (rad)','
    Fontsize',18,'FontWeight','bold');

%%%IIPIE
figure(6)
[AX2,H11, H12]=plotyy(f.*1e-15,re/max(re),F_pty.*1e-15,
    re_pty);
set(AX2(1),'ylim',[0 1],'ycolor','k','Fontsize', 20,'
    FontWeight','bold')
 set(AX2(2),'ylim',[-60 0], 'ytick',-60:10:0,'ycolor','r',
     'Fontsize', 20 ,'FontWeight','bold');
 set(AX2(1),'xlim',[-0.4 0.4],'FontWeight','bold')
 set(AX2(2),'xlim',[-0.4 0.4],'FontWeight','bold')
 set(H11,'LineWidth',3,'color','k');
 set(H12,'LineWidth',3,'color','r');
xlabel('Frequency (rad/fs)','Fontsize',24,'FontWeight','
    bold')
set(get(AX2(1),'Ylabel'),'String','Normalized intensity (a
    .u.)','Fontsize',24,'FontWeight','bold');
set(get(AX2(2),'Ylabel'),'String','I^2PIE Phase (rad)','
    Fontsize',24,'FontWeight','bold');

%%%Constant and linear phase shift parameters
figure(7)
A=0; %constant phase shift term (MIIPS)
B=-10; % linear phase shift in fs(MIIPS)
C=B*F_mp/1e15; %Amount of linear phase to add in order to
    rotate the phase about a central point

D=0; %onstant phase shift term (IIPIE)
G=17; % linear phase shift in fs (IIPIE)
H=G*F_pty/1e15; %Amount of linear phase to add in order to
     rotate the phase about a central point

%%%Updating phases with relevant constant and linear phase
     shifts
re_mp_up= re_mp+A+C; %updated miips phase
re_pty_up=re_pty+D+H; %updated pty phase

%%%Creating a YY plot of the phases
[AX3,H11,H12]=plotyy(F_mp.*1e-15,re_mp_up,F_pty.*1e-15,
    re_pty_up);
set(AX3(1),'ylim',[-40 30], 'ytick',-40:10:30,'ycolor','b'
    ,'Fontsize', 12,'FontWeight','bold');
```

```
set(AX3(2),'ylim',[0 60], 'ytick',0:10:60,'ycolor','r','
   Fontsize', 12,'FontWeight','bold');
set(AX3(1),'xlim',[-0.4 0.4],'FontWeight','bold')
set(AX3(2),'xlim',[-0.4 0.4],'FontWeight','bold')
set(H11,'LineWidth',2,'color','b');
set(H12,'LineWidth',2,'color','r');
xlabel('Frequency (rad/fs)','Fontsize',14,'FontWeight','
   bold')
set(get(AX3(1),'Ylabel'),'String','MIIPS Phase (rad)','
   Fontsize',14,'FontWeight','bold');
set(get(AX3(2),'Ylabel'),'String','IIPIE Phase (rad)','
   Fontsize',14,'FontWeight','bold');
legend('MIIPS','I^2PIE','Location','northwest');

%%%Plotting MIIPS and IIPIE phases on the same scale
re_pty_shift=re_pty;
figure(8)
plot(F_mp.*1e-15,re_mp+C,'-.b','LineWidth',2.5);
hold on;
plot(F_pty.*1e-15,re_pty_up-37,'r','LineWidth',2.5);
hold off;
axis([-0.2 0.3 -30 40])
set(gca,'Ydir','Normal','Fontsize', 20,'FontWeight','bold'
   )
set(gca,'Xdir','Normal','Fontsize', 20,'FontWeight','bold'
   )
ylabel('Phase (rad)','Fontsize',25)
xlabel('Frequency (rad/fs)','Fontsize',25)
legend('MIIPS','I^2PIE','Location','northwest');
```

C.3 NICA analysis code

This code analyzes the non-interferometric collinear autocorrelation (NICA) spectrogram for pulse duration measurements. ,

```
clear all
close all
clc

%%%INPUT DETAILS GATHERED
trace=dlmread('SG_789.00_pty2.txt'); %loads NICA trace
   from measurement
b_wave=dlmread('blue_wavelength_range.txt'); %load blue
   wavelength range
b_freq=dlmread('blue_freq_axis.txt');%load blue frequency
   range
```

```
red=dlmread('redspec_100nm_band_789.txt'); %load the red
   spectrum(supercontinuum source)
wc =789; %center wavelength of the SC
y=red(:,1);%intensity axis
x=red(:,2); %wavelength axis
trace=trace'; % transpose axis

%%%INPUT THE SCANNING PARAMETERS
win=2000;%window size in (fs)
s=401;%number of steps

%%%
uts=win/s; %defines what a single step corresponds in time
T=-(s/2):1:(s/2)-1; %defining time axis
ts=T*uts;
figure (1);imagesc(trace);colormap('jet');colorbar
set(gca,'Ydir','Normal')
set(gca,'Xdir','Normal')

%Replotting figure 1 with correct axis
figure (2);imagesc(ts',x,trace);colormap('jet');colorbar %
    Use only for spectrogram for IIPIE reconstruction
set(gca,'Ydir','Normal','Fontsize', 12,'FontWeight','bold'
   )
set(gca,'Xdir','Normal','Fontsize', 12,'FontWeight','bold'
   )
axis([-100 100 360 440]);
set(gca,'XLim',[-100 100])
set(gca,'XTick',(-100:25:100))
set(gca,'YLim',[360 440]);
set(gca,'YTick',(360:20:440))
xlabel('Time (fs)','Fontsize', 18,'FontWeight','bold')
ylabel('Wavelength(nm)','FontSize', 18,'FontWeight','bold'
   );
% title('Int. Col. Autocorr. trace- IIPIE compensation','
   Fontsize', 10,'FontWeight','bold')
%%%

% Finding the interference fringes at any point in time in
    wavelength
figure(3)
P=1; % define the time (step position for desired fringe,
   0 for no time delay)
fringe=(trace(:,P));%(trace(row range,column range))
nrm_fringe=fringe/max(fringe); %normalization
plot(x,nrm_fringe);% plotting fringe in wavelength
set(gca,'Ydir','Normal')
```

```
set(gca,'Xdir','Normal')
axis([300 500 0 1]); %axis range
xlabel('wavelength (nm)','Fontsize', 18,'FontWeight','bold
   ')% for wavelength plot
ylabel('Normalized Intensity (a.u.)','FontSize', 18,'
   FontWeight','bold');
% title('Pulse train at t=100fs (IIPIE)','Fontsize', 12,'
   FontWeight','bold')

%%%Finding the pulse duration
%Finding the sum of the the frequencies
Z_tr=sum(trace(1:3648,:));%defining omega axis
z=Z_tr/max(Z_tr); %Normalization of summed Intensities
figure(5)
plot(ts,z,'b','LineWidth',2)
axis([-150 150 0 inf]);
set(gca,'Ydir','Normal')
set(gca,'Xdir','Normal')
xlabel('Duration (fs)','Fontsize', 18,'FontWeight','bold')
ylabel('Normalized Intensity (a.u.)','FontSize', 18,'
   FontWeight','bold');
%title('Autocorrelation of pulse duration','Fontsize',
   12,'FontWeight','bold')

%%%plotting a horizontal slice
%%%PLOTTING THE SUPERCONTINUUM SPECTRUM
y=red(:,1);%intensity axis
x=red(:,2); %wavelength axis
figure(6)% red spectrum
plot(x,y,'r','LineWidth',2);
axis([650 900 0 inf])
xlabel('wavelength (nm)','Fontsize', 18,'FontWeight','bold
   ')
ylabel('Normalized Intensity (a.u.)','FontSize', 18,'
   FontWeight','bold');
title(' SC autocorrelation pulse','Fontsize', 12,'
   FontWeight','bold')

Int_max=max(red(:,1)); %maximum intensity
Int_norm=y/Int_max; %normalized Intensity
Z=mean(std(y(1000:1450))); %mean of standard deviation of
   background noise
Int_base=5*Z; %Gives the minimum intensity to consider as
   a signal
%
%
% %%%Make corresponding frequency axis
```

```
 c = 2.998*10^8;
 bc=wc/2;%Center wavelength for blue (don't think so)
 fc = 2*pi*c/(wc*10^-9);
 fexp = 2*pi*c./(x*10^-9);

 tn=3648;
 df = abs(fexp(1)-fexp(length(fexp)))/tn ;
 dt = 2*pi/(tn*df);% defining time from frequency
 t = dt*linspace(-tn/2,tn/2-1,tn);
 f = df*linspace(-tn/2,tn/2-1,tn);
 tp= t.*10^15;%%%converts axis to femtoseconds

figure(7)
plot(fexp,Int_norm,'r','LineWidth',2);
axis([2e15 3e15 0 inf])
xlabel('Angular freq (rad.Hz)','Fontsize', 18,'FontWeight'
   ,'bold')
ylabel('Normalized Intensity (a.u.)','FontSize', 18,'
   FontWeight','bold');
title('SC pulse in spectral domain','Fontsize', 12,'
   FontWeight','bold')
%
%
ff=fftshift(fft(y)); %Use when you do not want to consider
    the resampled points
YY=abs(ff);
yy=YY/max(YY);% normalizing intensity
figure(8)
plot(tp,yy,'b','LineWidth',2);
axis([-200 200 0 inf]);
xlabel('time(fs)','Fontsize', 18,'FontWeight','bold')
ylabel('Normalized Intensity (a.u.)','FontSize', 18,'
   FontWeight','bold');
title('Transform limited pulse of SC pulse','Fontsize',
   12,'FontWeight','bold')
%
%%%Determining autocorrelation of redspec
blue=(abs(fftshift(fft(fftshift(fftshift(ifft(fftshift(y))
   ).^2)))).^2);
nrm_blue=blue/max(blue);
figure(9)
x_ac=x/2;
plot(x_ac,nrm_blue);
axis([300 500 0 1])
set(gca,'Ydir','Normal','Fontsize',12,'FontWeight','bold')
set(gca,'Xdir','Normal','Fontsize',12,'FontWeight','bold')
```

```
xlabel('Wavelength (nm)','Fontsize', 18,'FontWeight','bold
    ')
ylabel('Correlation Intensity (a.u.)','FontSize', 18,'
    FontWeight','bold');
title('Autocorrelation of Supercontinuum pulse','Fontsize'
    , 12,'FontWeight','bold')
%

% %%%Overlap of measured and calculated autocorrelations.
figure(10)
plot(x,nrm_fringe,'LineWidth',2);
hold on
plot(x_ac,nrm_blue,'LineWidth',2);
hold off
axis([300 500 0 1])
set(gca,'Ydir','Normal','Fontsize',12,'FontWeight','bold')
set(gca,'Xdir','Normal','Fontsize',12,'FontWeight','bold')
xlabel('Wavelength (nm)','Fontsize', 18,'FontWeight','bold
    ')
ylabel('Normalized Intensity (a.u.)','FontSize', 18,'
    FontWeight','bold');
title('Measured autocorrelation vrs SC autocorrelation','
    Fontsize', 12,'FontWeight','bold')
legend('Measured','Calculated','Location','northwest');
```

List of References

[1] Chen, H., Rogalski, M.M. and Anker, J.N.: Advances in functional X-ray imaging techniques and contrast agents. *Physical Chemistry Chemical Physics*, vol. 14, no. 39, pp. 13469–13486, 2012.

[2] Kathiravan, S.: A Review of Magnetic Resonance Imaging Techniques. *The Smart Computing Review*, vol. 3, no. 5, pp. 358–366, 2013.

[3] Sprawls, P.: *Magnetic Resonance Imaging: Principles, Methods and Techniques*, vol. 24. Medical Physics Publishing Corporation, Madison, Wisconsin, 2000.

[4] Ginat, D.T. and Gupta, R.: Advances in Computed Tomography Imaging Technology. *Annual Review of Biomedical Engineering*, vol. 16, no. 1, pp. 431–453, 2014.

[5] Iftimia, N., Brugge, W.R. and Hammer, D.X.: *Advances in Optical Imaging for Clinical Medicine*. John Wiley & Sons, Inc, 2011.

[6] Olsen, J., Holmes, J. and Jemec, G.B.E.: Advances in optical coherence tomography in dermatology-a review. *Journal of Biomedical Optics*, vol. 23, no. 04, pp. 040901–10, 2018.

[7] Arranz, A. and Ripoll, J.: Advances in optical imaging for pharmacological studies. *Frontiers in Pharmacology*, vol. 6, no. SEP, pp. 1–7, 2015.

[8] Liu, J., Saw, C.L.L., Olivo, M., Sudhaharan, T., Ahmed, S., Heng, P.W.S. and Wohland, T.: Study of interaction of hypericin and its pharmaceutical preparation by fluorescence techniques. *Journal of Biomedical Optics*, vol. 14, no. 1, p. 014003, 2009.

[9] Liang, H., Peric, B., Hughes, M., Podoleanu, A., Spring, M. and Saunders, D.: Optical coherence tomography for art conservation and archaeology. *O3A: Optics for Arts, Architecture, and Archaeology*, vol. 6618, p. 661805, 2007.

[10] Maiman, T.H.: *The Laser Inventor: Memoirs of Theodore H. Maiman*. 1st edn. Springer, 2018.

[11] Stemmer, A., Beck, M. and Fiolka, R.: Widefield fluorescence microscopy with extended resolution. *Histochemistry and Cell Biology*, vol. 130, no. 5, pp. 807–817, 2008.

[12] Hofer, M., Soeller, C., Brasselet, S. and Bertolotti, J.: Wide field fluorescence epimicroscopy behind a scattering medium enabled by speckle correlations. *Optics Express*, vol. 26, no. 8, p. 9866, 2018.

[13] Sanderson, M.J., Smith, I., Parker, I. and Bootman, M.D.: Flourescence Microscopy. *Cold Spring Harb Protocol*, vol. 2014, no. 10, p. 36, 2016.

[14] Kasha, M.: Characterization of Electronic Transitions in Complex Molecules. *Discussions of the Faraday Society*, vol. 9, pp. 14–19, 1950.

[15] Perry, S.W., Burke, R.M. and Brown, E.B.: Two-photon and second harmonic microscopy in clinical and translational cancer research. *Annals of Biomedical Engineering*, vol. 40, no. 2, pp. 277–291, 2012.

[16] Semwogerere, D. and Weeks, E.R.: Confocal microscopy. In: *Encyclopedia of Biomaterials and Biomedical Engineering*. Taylor & Francis, 2005.

[17] Masters, B.R. and So, P.T.C.: Confocal microscopy and multi-photon excitation microscopy of human skin in vivo. *Optics Express*, vol. 8, no. 1, pp. 2–10, 2001.

[18] Minsky M.: Memoir on Inventing the Confocal Scanning Microscope. *Scanning*, vol. 10, no. 1 988, pp. 128–138, 1988.

[19] Lefort, C.: A review of biomedical multiphoton microscopy and its laser sources. *Journal of Physics D: Applied Physics*, vol. 50, no. 42, p. 423001, 2017.

[20] Satsoura, D., Leber, B., Andrews, D.W. and Fradin, C.: Circumvention of fluorophore photobleaching in fluorescence fluctuation experiments: A beam scanning approach. *ChemPhysChem*, vol. 8, no. 6, pp. 834–848, 2007.

[21] Mayer, M.G.: Über Elementarakte mit zwei Quantensprüngen. *Annalen der Physik*, vol. 401, no. 3, pp. 273–294, 1931.

[22] Masters, B.R. and So, P.T.C.: English Translations of and Translator's Notes on Maria Göppert-Mayer's Theory of Two-Quantum Processes. In: *Handbook of Biological Nonlinear Optical Microscopy*, pp. 42–84. Oxford University, 2008. ISBN 9780195162608.

[23] Franken, P.A., Hill, A.E., Peters, C.W. and Weinreich, G.: Generation of optical harmonics. *Physical Review Letters*, vol. 7, no. 4, pp. 118–119, 1961.

[24] Sarder, P., Yazdanfar, S., Akers, W.J., Tang, R., Sudlow, G.P., Egbulefu, C. and Achilefu, S.: All-near-infrared multiphoton microscopy interrogates intact tissues at deeper imaging depths than conventional single- and two-photon near-infrared excitation microscopes. *Journal of Biomedical Optics*, vol. 18, no. 10, p. 106012, 2013.

[25] Theer, P., Kuhn, B., Keusters, D. and Denk, W.: Two-photon Microscopy and Imaging. In: Meyers, R.A. (ed.), *Encyclopedia of Molecular Cell Biology and Molecular Medicine*, vol. 15, pp. 61–88. Wiley-VCH Verlag GmbH & Co, 2006.

[26] So, P., Dong, C.Y., Masters, B.R. and Berland, K.M.: Two-photon Excitation Fluorescence microscopy. *Annual Review of Biomedical Engineering*, vol. 2, no. 1, pp. 399–429, 2000.

[27] Adur, J., Carvalho, H.F., Cesar, C.L. and Casco, V.H.: Nonlinear Microscopy Techniques: Principles and Biomedical Applications. In: *Microscopy and Analysis*, chap. 6, pp. 121–149. IntechOpen, 2016.

[28] König, K.: Multiphoton microscopy in life sciences. *Journal of Microscopy*, vol. 200, no. 2, pp. 83–104, 2000.

[29] Chen, J., Zhuo, S., Luo, T., Jiang, X. and Zhao, J.: Spectral characteristics of autofluorescence and second harmonic generation from ex vivo human skin induced by femtosecond laser and visible lasers. *Scanning*, vol. 28, no. 6, pp. 319–326, 2006.

[30] Botchway, S.W., Reynolds, P., Parker, A.W. and O'Neill, P.: Use of near infrared femtosecond lasers as sub-micron radiation microbeam for cell DNA damage and repair studies. *Mutation Research - Reviews in Mutation Research*, vol. 704, no. 1-3, pp. 38–44, 2010.

[31] Li, R., Wang, X., Zhou, Y., Zong, H., Chen, M. and Sun, M.: Advances in nonlinear optical microscopy for biophotonics. *J. Nanophoton*, vol. 12, no. 3, p. 033007, 2018.

[32] Varone, A., Xylas, J., Quinn, K.P., Pouli, D., Sridharan, G., McLaughlin-Drubin, M.E., Alonzo, C., Lee, K., Münger, K. and Georgakoudi, I.: Endogenous two-photon fluorescence imaging elucidates metabolic changes related to enhanced glycolysis and glutamine consumption in precancerous epithelial tissues. *Cancer Research*, vol. 74, no. 11, pp. 3067–3075, 2014.

[33] Yasui, T., Takahashi, Y., Ito, M., Fukushima, S. and Araki, T.: Ex vivo and in vivo second-harmonic-generation imaging of dermal collagen fiber in skin: Comparison of imaging characteristics between mode-locked Cr:forsterite and Ti:Sapphire lasers. *Applied Optics*, vol. 48, no. 10, pp. 88–95, 2009.

[34] Reshak, A.H.: High second harmonic generation signal from muscles and fascia pig's muscles using the two-photon laser scanning microscope. *Journal of Microscopy*, vol. 234, no. 3, pp. 280–286, 2009.

[35] Cox, G.: Biological applications of second harmonic imaging. *Biophysical Reviews*, vol. 3, no. 3, pp. 131–141, 2011.

[36] Guesmi, K., Abdeladim, L., Tozer, S., Mahou, P., Kumamoto, T., Jurkus, K., Rigaud, P., Loulier, K., Dray, N., Georges, P., Hanna, M., Livet, J., Supatto, W., Beaurepaire, E. and Druon, F.: Dual-color deep-tissue three-photon microscopy with a multiband infrared laser. *Light: Science and Applications*, vol. 7, no. 12, pp. 1–9, 2018.

[37] Rowlands, C.J., Park, D., Bruns, O.T., Piatkevich, K.D., Fukumura, D., Jain, R.K., Bawendi, M.G., Boyden, E.S. and So, P.T.: Wide-field three-photon excitation in biological samples. *Light: Science and Applications*, vol. 6, no. 5, pp. e16255–9, 2017.

[38] Weigelin, B., Bakker, G.J. and Friedl, P.: Third harmonic generation microscopy of cells and tissue organization. *Journal of Cell Science*, vol. 129, no. 2, pp. 245–255, 2016.

[39] Masihzadeh, O., Lei, T.C., Domingue, S.R., Kahook, M.Y., Bartels, R.A. and Ammar, D.A.: Third harmonic generation microscopy of a mouse retina. *Molecular Vision*, vol. 21, no. May, pp. 538–547, 2015.

[40] Chu, S.W., Tai, S.P., Ho, C.L., Lin, C.H. and Sun, C.K.: High-resolution simultaneous three-photon fluorescence and third-harmonic-generation microscopy. *Microscopy Research and Technique*, vol. 66, no. 4, pp. 193–197, 2005.

[41] Saytashev, I., Glenn, R., Murashova, G.A., Osseiran, S., Spence, D., Evans, C.L. and Dantus, M.: Multiphoton excited hemoglobin fluorescence and third harmonic generation for non-invasive microscopy of stored blood. *Biomedical Optics Express*, vol. 7, no. 9, p. 3449, 2016.

[42] Krafft, C., Dietzek, B., Schmitt, M. and Popp, J.: Raman and coherent anti-Stokes Raman scattering microspectroscopy for biomedical applications. *Journal of Biomedical Optics*, vol. 17, no. 4, p. 040801, 2012.

[43] Rodriguez, L.G., Lockett, S.J. and Holtom, G.R.: Coherent Anti-Stokes Raman Scattering Microscopy: A Biological Review. *Cytometry Part A*, vol. 69A, pp. 779–791, 2006.

[44] Katz, O., Levitt, J.M., Grinvald, E. and Silberberg, Y.: Single-beam coherent Raman spectroscopy and microscopy via spectral notch shaping. *Optics Express*, vol. 18, no. 22, p. 22693, 2010.

[45] Roy, S., Wrzesinski, P., Pestov, D., Gunaratne, T., Dantus, M. and Gord, J.R.: Single-beam coherent anti-Stokes Raman scattering spectroscopy of N 2 using a shaped 7 fs laser pulse. *Applied Physics Letters*, vol. 95, no. 7, p. 74102, 2009.

[46] Tada, K. and Karasawa, N.: Single-beam coherent anti-stokes raman scattering spectroscopy using both pump and soliton stokes pulses from a photonic crystal fiber. *Applied Physics Express*, vol. 4, no. 9, p. 092701, 2011.

[47] Tu, H. and Boppart, S.A.: Coherent anti-Stokes Raman scattering microscopy: Overcoming technical barriers for clinical translation. *Journal of Biophotonics*, vol. 7, no. 1-2, pp. 9–22, 2014.

[48] Cheng, J.-X.: Coherent Anti-Stokes Raman Scattering. *Applied Spectroscopy*, vol. 61, no. 9, pp. 197A–208A, 2007.

[49] Hu, F., Shi, L. and Min, W.: Biological imaging of chemical bonds by stimulated Raman scattering microscopy. *Nature Methods*, vol. 16, no. 9, pp. 830–842, 2019.

[50] Ehmke, T., Knebl, A. and Heisterkamp, A.: Four-wave mixing microscopy: a high potential nonlinear imaging method. *Multiphoton Microscopy in the Biomedical Sciences XV*, vol. 9329, p. 932912, 2015.

[51] Abbe, E.: Beiträge zur Theorie des Mikroskops und der mikroskopischen Wahrnehmung. *Arch. Mikr. Anat.*, vol. 9, pp. 413–468, 1873.

[52] Lord Rayleigh, F.: XXXI. Investigations in optics, with special reference to the spectroscope. *The London, Edinburgh, and Dublin Philosophical Magazine and Journal of Science*, vol. 8, no. 49, pp. 261–274, 1879.

[53] Squier, J. and Müller, M.: High resolution nonlinear microscopy: A review of sources and methods for achieving optimal imaging. *Review of Scientific Instruments*, vol. 72, no. 7, pp. 2855–2867, 2001.

[54] Huang, B., Bates, M. and Zhuang, X.: Super-Resolution Fluorescence Microscopy. *Annual Review ofBiochemistry*, vol. 78, pp. 993–1016, 2009.

[55] Cox, G. and Sheppard, C.J.: Practical Limits of Resolution in Confocal and Non-Linear Microscopy. *Microscopy Research and Technique*, vol. 63, no. 1, pp. 18–22, 2004.

[56] Pelli, D.G. and Bex, P.: Measuring contrast sensitivity. *Vision Research*, vol. 90, pp. 10–14, 2013.

[57] Saytashev, I.: *Nonlinear optical microscopy of highly pigmented tissues*. PhD, Michigan State University, 2016.

[58] Dudley, J.M., Genty, G. and Coen, S.: Supercontinuum generation in photonic crystal fiber. *Reviews of Modern Physics*, vol. 78, no. 4, pp. 1135–1184, 2006.

[59] Liu, Y., Tu, H., Benalcazar, W.A., Chaney, E.J. and Boppart, S.A.: Multimodal nonlinear microscopy by shaping a fiber supercontinuum from 900 to 1160nm. *IEEE Journal on Selected Topics in Quantum Electronics*, vol. 18, no. 3, pp. 1209–1214, 2012.

[60] Tu, H. and Boppart, S.A.: Coherent fiber supercontinuum for biophotonics. *Laser and Photonics Reviews*, vol. 7, no. 5, pp. 628–645, 2013.

[61] Dunsby, C. and French, P.M.: Biophotonics applications of supercontinuum generation. In: Dudley, J. and Taylor, J. (eds.), *Supercontinuum Generation in Optical Fibers*, vol. 9780521514, chap. 15, pp. 349–372. Cambridge University Press, Cambridge, 2010.

[62] Lozovoy, V.V., Pastirk, I., Walowicz, K.A. and Dantus, M.: Multiphoton intrapulse interference. II. Control of two- and three-photon laser induced fluorescence with shaped pulses. *Journal of Chemical Physics*, vol. 118, no. 7, pp. 3187–3196, 2003.

[63] Lozovoy, V.V., Pastirk, I. and Dantus, M.: Multiphoton intrapulse interference. IV. Ultrashort laser pulse spectral phase characterization and compensation. *Optics Letters*, vol. 29, no. 7, p. 775, 2004.

[64] Comin, A., Ciesielski, R., Coca-López, N. and Hartschuh, A.: Phase retrieval of ultrashort laser pulses using a MIIPS algorithm. *Optics Express*, vol. 24, no. 3, pp. 2505–2512, 2016.

[65] Nie, B., Saytashev, I., Chong, A., Liu, H., Arkhipov, S.N., Wise, F.W. and Dantus, M.: Multimodal microscopy with sub-30 fs Yb fiber laser oscillator. *Biomedical Optics Express*, vol. 3, no. 7, p. 1750, 2012.

[66] Xi, P., Andegeko, Y., Weisel, L.R., Lozovoy, V.V. and Dantus, M.: Greater signal, increased depth, and less photobleaching in two-photon microscopy with 10 fs pulses. *Optics Communications*, vol. 281, no. 7, pp. 1841–1849, 2008.

[67] Comin, A., Ciesielski, R., Piredda, G., Donkers, K. and Hartschuh, A.: Compression of ultrashort laser pulses via gated multiphoton intrapulse interference phase scans. *Journal of the Optical Society of America B*, vol. 31, no. 5, p. 1118, 2014.

[68] Comin, A., Rhodes, M., Ciesielski, R., Trebino, R. and Hartschuh, A.: Pulse Characterization in Ultrafast Microscopy: a Comparison of FROG, MIIPS and G-MIIPS. In: *CLEO: 2015*, p. SW1H.5. OSA, Washington, D.C., 2015.

[69] Spangenberg, D., Neethling, P., Rohwer, E. and Feurer, T.: Time-domain ptychography. *Physical Review A*, vol. 91, no. 2, p. 021803, 2015.

[70] Spangenberg, D.-M., Rohwer, E., Brügmann, M. and Feurer, T.: Extending time-domain ptychography to generalized phase-only transfer functions. *arXiv e-print1904.08849*, , no. 3, pp. 1–5, 2019.

[71] Salas Redondo, C., Kleine, P., Roszeitis, K., Achenbach, T., Kroll, M., Thomschke, M. and Reineke, S.: Interplay of Fluorescence and Phosphorescence in Organic Biluminescent Emitters. *Journal of Physical Chemistry C*, vol. 121, no. 27, pp. 14946–14953, 2017.

[72] So, P.T.C. and Dong, C.Y.: *Fluorescence Spectrophotometry*. Macmillan Publishers Ltd, Nature Publishing Group., 2002.

[73] Träger, F.: Handbook of Lasers and Optics. 2nd edn, chap. 5, pp. 157–248. Springer, 2012.

[74] Murti, Y. and Vijayan, C.: Nonlinear Wave Mixing Processes. In: *Essentials of Nonlinear Optics*, 1st edn, chap. 5, pp. 77–100. John Wiley & Sons, 2014.

[75] Ciriolo, A.G., Negro, M., Devetta, M., Cinquanta, E., Faccialà, D., Pusala, A., Silvestri, S.D., Stagira, S. and Vozzi, C.: Optical Parametric Amplification Techniques for the Generation of High-Energy Few-Optical-Cycles IR Pulses for Strong Field Applications. *Appl sci*, vol. 7, p. 265, 2017.

[76] Kessel, A.: *Generation and parametric amplification of few-cycle light pulses at relativistic intensities*. PhD, LMU München, 2017.

[77] Garmire, E.: Overview of Nonlinear Optics. In: *Nonlinear Optics*, chap. 1. IntechOpen, 2012.

[78] Boyd, R.: *Nonlinear Optics*. 3rd edn. Elsevier, 2008. ISBN 9780123694706.

[79] Stolen, R.H. and Lin, C.: Self-phase-modulation in silica optical fibers. *Physical Review A*, vol. 17, no. 4, pp. 1448–1453, 1978.

[80] Alfano, R.R.: Generation of Ultrashort and Coherent Supercontinuum Light Pulses in All-Normal Dispersion Fibers. In: *The Supercontinuum Laser Source*, 3rd edn, pp. 247–280. Springer, 2016.

[81] Heidt, A.M.: *Novel coherent supercontinuum light sources based on all-normal dispersion fibers Dissertation*. PhD, Stellenbosch University, 2011.

[82] Corkum, P. and Davis, R.L.: Attosecond pulses at last Neurofibromin progress on the fly. *Nature*, vol. 403, no. FEBRUARY, pp. 845–846, 2000.

[83] Feng, L. and Li, Y.: High-intensity isolated attosecond X-ray pulse generation by using low-intensity ultraviolet-mid-infrared laser beam. *European Physical Journal D*, vol. 72, no. 167, pp. 1–9, 2018.

[84] Wikmark, H., Guo, C., Vogelsang, J., Smorenburg, P.W., Coudert-Alteirac, H., Lahl, J., Peschel, J., Rudawski, P., Dacasa, H., Carlström, S., MacLot, S., Gaarde, M.B., Johnsson, P., Arnold, C.L. and L'Huillier, A.: Spatiotemporal coupling of attosecond pulses. *Proceedings of the National Academy of Sciences of the United States of America*, vol. 116, no. 11, pp. 4779–4787, 2019.

[85] Reid, G.D. and Wynne, K.: *Ultrafast Laser Technology and Spectroscopy*. John Wiley & Sons, Ltd, 2006.

[86] Pires, H., Baudisch, M., Sanchez, D., Hemmer, M. and Biegert, J.: Ultrashort pulse generation in the mid-IR. *Progress in Quantum Electronics*, vol. 43, pp. 1–30, 2015.

[87] Aizawa, T. and Inohara, T.: Pico- and Femtosecond Laser Micromachining for Surface Texturing. In: *Micromachining*, pp. 1–28. IntechOpen, 2019.

[88] Webster, A.: Useful mathematical formulas for transform limited pulses pulses of light [Online]. Available at: http://falsecolour.com/aw/pulses/pulses.pdf, [Date accessed: 21-07-2019], 2012.

[89] Koike, Y. and Asai, M.: The future of plastic optical fiber. *NPG Asia Materials*, vol. 1, no. 1, pp. 22–28, 2009.

[90] Zubia, J. and Arrue, J.: Plastic optical fibers: An introduction to their technological processes and applications. *Optical Fiber Technology*, vol. 7, no. 2, pp. 101–140, 2001.

[91] Schuster, K., Unger, S., Aichele, C., Lindner, F., Grimm, S., Litzkendorf, D., Kobelke, J., Bierlich, J., Wondraczek, K. and Bartelt, H.: Material and technology trends in fiber optics. *Advanced Optical Technologies*, vol. 3, no. 4, pp. 447–468, 2014.

[92] Pilz, S., Najafi, H., Ryser, M. and Romano, V.: Granulated silica method for the fiber preform production. *Fibers*, vol. 5, no. 24, pp. 1–19, 2017.

[93] Dubietis, A., Couairon, A. and Genty, G.: Supercontinuum generation: introduction. *Journal of the Optical Society of America B*, vol. 36, no. 2, pp. SG1–SG3, 2019.

[94] Alfano R.R. and Shapiro S.L.: Emission in the Region 4000 To 7000a Via Four-Photon Coupling in Glass. *Physical Review Letters*, vol. 24, no. 11, pp. 584–588, 1970.

[95] Hartung, A., Heidt, A.M. and Bartelt, H.: Design of all-normal dispersion microstructured optical fiers for pulse-preserving supercontinuum generation. *Optics express*, vol. 19, no. 8, pp. 7742–7749, 2011.

[96] Zhang, Y., Husko, C., Lefrancois, S., Rey, I.H., Krauss, T.F., Schr, J. and Eggleton, B.J.: Cross-phase modulation-induced spectral broadening in silicon waveguides. *Optics Express*, vol. 24, no. 1, pp. 443–451, 2016.

[97] Hartung, A., Heidt, A.M. and Bartelt, H.: Pulse-preserving broadband visible supercontinuum generation in all-normal dispersion tapered suspended-core optical fibers. *Optics express*, vol. 19, no. 13, pp. 12275–83, 2011.

[98] Demmler, S., Rothhardt, J., Heidt, A.M., Hartung, A., Rohwer, E.G., Bartelt, H., Limpert, J. and Tünnermann, A.: Generation of high quality, 1.3 cycle pulses by active phase control of an octave spanning supercontinuum. *Optics Express*, vol. 19, no. 21, p. 20151, 2011.

[99] Heidt, A.M., Hartung, A., Bosman, G.W., Krok, P., Rohwer, E.G., Schwoerer, H. and Bartelt, H.: Coherent octave spanning near-infrared and visible supercontinuum generation in all-normal dispersion photonic crystal fibers. *Optics express*, vol. 19, no. 4, pp. 3775–3787, 2011.

[100] Heidt, A.M., Feehan, J.S., Price, J.H.V. and Feurer, T.: Limits of coherent supercontinuum generation in normal dispersion fibers. *Journal of the Optical Society of America B*, vol. 34, no. 4, pp. 764–775, 2017.

[101] Heidt, A.M.: Tailoring flat-top supercontinuum generation in all-normal dispersion photonic crystal fibers at 1080 nm. *Journal of the Optical Society of America B*, vol. 27, no. 3, pp. 550–559, 2010.

[102] Heidt, A.M.: Pulse preserving flat-top supercontinuum generation in all-normal dispersion photonic crystal fibers. *Journal of the Optical Society of America B*, vol. 27, no. 3, p. 550, 2010. ISSN 0740-3224.

[103] Heidt, A.M., Rothhardt, J., Hartung, A., Bartelt, H., Rohwer, E.G., Limpert, J. and Tünnermann, A.: High quality sub-two cycle pulses from compression of supercontinuum generated in all-normal dispersion photonic crystal fiber. *Optics express*, vol. 19, no. 15, pp. 13873–9, 2011.

[104] Sukhoivanov, I.A., Iakushev, S.O., Shulika, O.V., Andradelucio, J.A., Díez, A. and Andrés, M.: Supercontinuum generation at 800 nm in all-normal dispersion photonic crystal fiber. *Optics express*, vol. 22, no. 24, pp. 30234–30250, 2014.

[105] Sharma, M., Borgohain, N. and Konar, S.: Index Guiding Photonic Crystal Fibers With Large. *Journal of Lightwave Technology*, vol. 31, no. 21, pp. 3339–3344, 2013.

[106] Poletti, F., Petrovich, M.N. and Richardson, D.J.: Hollow-core photonic bandgap fibers : technology and applications. *Nanophotonics*, vol. 2, no. 5-6, pp. 315–340, 2013.

[107] Jin, W., Ju, J., Ho, H.L., Hoo, Y.L. and Zhang, A.: Photonic crystal fibers, devices, and applications. *Front. Optoelectron*, vol. 6, no. 1, pp. 3–24, 2013.

[108] Photonics, N.: Nl-1050-neg-1 nonlinear photonic crystal fiber [Online]. Available at: http://ainnotech.com/ainnotech/pdf/04/1_3/6NKT_NL-1050-NEG-1_Nonlinear%20Photonic%20Crystal%20Fiber.pdf, [Date accessed: 04-04-2019].

[109] Zhang, C., Zhang, Z., Xu, X. and Cai, W.: Thermally optimized polarization-maintaining photonic crystal fiber and its FOG application. *Sensors (Switzerland)*, vol. 18, no. 2, pp. 1–10, 2018.

[110] Romagnoli, P., Biazoli, C.R., Franco, M.A.R., Cordeiro, C.M.B. and de Matos, C.J.S.: Integrated polarizers based on tapered highly birefringent photonic crystal fibers. *Optics Express*, vol. 22, no. 15, p. 17769, 2014.

[111] Tu, H., Liu, Y., Liu, X., Turchinovich, D., Lægsgaard, J. and Boppart, S.A.: Nonlinear polarization dynamics in a weakly birefringent all-normal dispersion photonic crystal fiber: toward a practical coherent fiber supercontinuum laser. *Optics express*, vol. 20, no. 2, pp. 1113–1128, feb 2012.

[112] Mak, K.F., Travers, J.C., Joly, N.Y., Abdolvand, A. and Russell, P.S.J.: Two techniques for temporal pulse compression in gas-filled hollow-core kagomé photonic crystal fiber. *Optics Letters*, vol. 38, no. 18, p. 3592, 2013.

[113] Wilcox, D.E. and Ogilvie, J.P.: Comparison of pulse compression methods using only a pulse shaper. *Journal of the Optical Society of America B*, vol. 31, no. 7, p. 1544, 2014.

[114] Linden, S., Kuhl, J. and Giessen, H.: Amplitude and phase characterization of weak blue ultrashort pulses by downconversion. *Optics Letters*, vol. 24, no. 8, p. 569, 1999.

[115] Trebino, R.: *Frequency-Resolved Optical Gating: The Measurement of Ultrashort Laser Pulses*. 1st edn. Kluwer Academic Publishers, Boston, 2000.

[116] Trebino, R., DeLong, K.W., Fittinghoff, D.N., Sweetser, J.N., Krumbügel, M.A., Richman, B.A. and Kane, D.J.: Measuring ultrashort laser pulses in the time-frequency domain using frequency-resolved optical gating. *Review of Scientific Instruments*, vol. 68, no. 9, pp. 3277–3295, 1997.

[117] Iaconis, C. and Walmsley, I.A.: Spectral phase interferometry for direct electric-field reconstruction of ultrashort optical pulses. *Optics Letters*, vol. 23, no. 10, p. 792, may 1998.

[118] Bosman, G.W.: *Ultrashort Optical Pulse Characterization*. MSc Thesis, University of Stellenbosch, 2008.

[119] DeLong, K.W., Trebino, R., Hunter, J. and White, W.E.: Frequency-resolved optical gating with the use of second-harmonic generation. *Journal of the Optical Society of America B*, vol. 11, no. 11, pp. 2206–2215, 1994.

[120] Stibenz, G. and Steinmeyer, G.: Interferometric frequency-resolved optical gating. *Opt. Express*, vol. 13, no. 7, pp. 2617–2626, 2005.

[121] Galler, A. and Feurer, T.: Pulse shaper assisted short laser pulse characterization. *Applied Physics B: Lasers and Optics*, vol. 90, no. 3-4, pp. 427–430, 2008.

[122] Hyyti, J., Escoto, E. and Steinmeyer, G.: Pulse retrieval algorithm for interferometric frequency-resolved optical gating based on differential evolution. *Review of Scientific Instruments*, vol. 88, no. 10, p. 103102, 2017.

[123] Tu, H., Liu, Y., Turchinovich, D. and Boppart, S.A.: Compression of fiber supercontinuum pulses to the Fourier-limit in a high-numerical-aperture focus. *Optics Letters*, vol. 36, no. 12, p. 2315, 2011.

[124] Xu, B., Gunn, J.M., Cruz, J.M.D., Lozovoy, V.V. and Dantus, M.: Quantitative investigation of the multiphoton intrapulse interference phase scan method for simultaneous phase measurement and compensation of femtosecond laser pulses. *Journal of the Optical Society of America B*, vol. 23, no. 4, pp. 750–759, 2006.

[125] Rodenburg, J.M.: Ptychography and related diffractive imaging methods. *Advances in Imaging and Electron Physics*, vol. 150, no. 07, pp. 87–184, 2008.

[126] Spangenberg, D.-M.: *Time Domain Ptychography*. PhD thesis, Stellenbosch University, 2015.

[127] Faulkner, H.M. and Rodenburg, J.M.: Error tolerance of an iterative phase retrieval algorithm for moveable illumination microscopy. *Ultramicroscopy*, vol. 103, no. 2, pp. 153–164, 2005.

[128] Maiden, A.M. and Rodenburg, J.M.: An improved ptychographical phase retrieval algorithm for diffractive imaging. *Ultramicroscopy*, vol. 109, no. 10, pp. 1256–1262, 2009.

[129] Spangenberg, D., Rohwer, E., Brügmann, M.H. and Feurer, T.: Ptychographic ultrafast pulse reconstruction. *Optics Letters*, vol. 40, no. 6, pp. 1002–1005, 2015.

[130] Spectra-Physics: Tsunami-mode-locked ti:sapphire laser-user's manual [Online]. Available at: http://physics.ucsd.edu/neurophysics/courses/physics{_}173{_}273/232A{_}Rev{_}D{_}Tsunami{_}User{_}Manual.pdf, [Date accessed:11-10-2019], 2002.

[131] Weiner, A.M.: Femtosecond pulse shaping using spatial light modulators. *Review of Scientific Instruments*, vol. 71, no. 5, pp. 1929–1960, 2000.

[132] Weiner, A.M.: Ultrafast optical pulse shaping : A tutorial review. *Optics Communications*, vol. 284, no. 15, pp. 3669–3692, 2011.

[133] Szipöcs, R., Spielmann, C., Krausz, F. and Ferencz, K.: Chirped multilayer coatings for broadband dispersion control in femtosecond lasers. *Optics Letters*, vol. 19, no. 3, pp. 201–203, 1994.

[134] Matuschek, N., Kärtner, F.X. and Keller, U.: Analytical Design of Double-Chirped Mirrors with Custom-Tailored Dispersion Characteristics. *IEEE Journal of Quantum Electronics*, vol. 35, no. 2, pp. 129–137, 1999.

[135] Präkelt, A., Wollenhaupt, M., Assion, A., Horn, C., Sarpe-Tudoran, C., Winter, M. and Baumert, T.: Compact, robust, and flexible setup for femtosecond pulse shaping. *Review of Scientific Instruments*, vol. 74, no. 11, pp. 4950–4953, 2003.

[136] Brixner, T. and Gerber, G.: Femtosecond polarization pulse shaping. *Optics letters*, vol. 26, no. 8, pp. 557–9, 2001.

[137] Viljoen, R.: *Supercontinuum pulse characterisation and compression.* MSc Thesis, University of Stellenbosh, 2017.

[138] Neethling, P.: *Determining non-linear optical properties using the Z-scan technique.* MSc Dissertation, University of Stellenbosch, 2005.

[139] Jabbar, A.S., Abbas, S.I. and Al-zubaidy, M.H.: Studying the Linear and Nonlinear Optical Properties by Using Z-Scan Technique for CdS Thin Films Prepared by CBD Technique. *Applied Physics Research*, vol. 10, no. 3, pp. 7–13, 2018.

[140] Milonni, P.W. and Eberly, J.H.: *Laser physics.* 1st edn. John Wiley & Sons, Inc, 2010.

[141] Buah-Bassuah, P.K., Von Bergmann, H.M., Tatchie, E.T. and Steenkamp, C.M.: A portable fibre-probe ultraviolet light emitting diode (LED)-induced fluorescence detection system. *Measurement Science and Technology*, vol. 19, no. 2, p. 025601, 2008.

[142] Ndebeka, W.I.: *Charge carrier effects in free standing Si membranes investigated by linear and second harmonic optical techniques.* PhD, Stellenbosch University, 2016.

[143] Accanto, N., Nieder, J.B., Piatkowski, L., Castro-Lopez, M., Pastorelli, F., Brinks, D. and Van Hulst, N.F.: Phase control of femtosecond pulses on the nanoscale using second harmonic nanoparticles. *Light: Science and Applications*, vol. 3, no. October 2013, pp. 1–7, 2014.

[144] Schmidt, B., Hacker, M., Stobrawa, G. and Feurer, T.: LAB2-A virtual femtosecond laser lab.
Available at: http://www.lab2.de

[145] Diels, J.C. and Rudolph, W.: Fundamentals. In: *Ultrashort Laser Pulse Phenomena*, 2nd edn, chap. 1, pp. 1–58. Elsevier, 2006.

[146] Hahn, D.: Calcium Fluoride and Barium Fluoride Crystals in Optics: Multispectral optical materials for a wide spectrum of applications. *Optik & Photonik*, vol. 9, no. 4, pp. 45–48, 2014.

[147] Wüstner, D., Christensen, T., Solanko, L.M. and Sage, D.: Photobleaching kinetics and time-integrated emission of fluorescent probes in cellular membranes. *Molecules*, vol. 19, no. 8, pp. 11096–11130, 2014.

[148] Smith, S.W.: Special Imaging Techniques. In: *The Scientist and Engineer's Guide to Digital Signal Processing*, 2nd edn, chap. 25, pp. 423–450. California Technical Publishing, San Diego, CA, 1999.

[149] Lashansky, S.N., Mansbach, S., Berger, M.J., Karasik, T. and Bin-Nun, M.: Edge response revisited. *Proc. SPIE 6941, Infrared Imaging Systems: Design, Analysis, Modeling, and Testing XIX*, vol. 6941, no. 1, pp. 69410Z–1–9, 2008.

[150] Nafisi, S. and Maibach, H.I.: *Skin penetration of nanoparticles.* Elsevier Inc., 2018. ISBN 9780323400169.

[151] Stecco, C., Hammer, W., Vleeming, A. and Caro, R.D.: Connective Tissues 1. In: *Functional Atlas of the Human Fascial System*, chap. 1 Connecti, pp. 1–20. Elsevier, 2015.

[152] Chu, S.-W., Chen, I.-H., Liu, T.-M., Chen, P.C., Sun, C.-K. and Lin, B.-L.: Multimodal nonlinear spectral microscopy based on a femtosecond Cr:forsterite laser. *Optics Letters*, vol. 26, no. 23, p. 1909, 2001.

[153] Reshak, A.H.: Second harmonic generation from thick leaves using the two-photon laser scanning microscope. *Micron*, vol. 40, no. 4, pp. 455–462, 2009.

[154] Reshak, A.H. and Sheue, C.R.: Second harmonic generation imaging of the deep shade plant Selaginella erythropus using multifunctional two-photon laser scanning microscopy. *Journal of Microscopy*, vol. 248, no. 3, pp. 234–244, 2012.

[155] Scavo, A.J., Sidhom, M., Rangel, F.J., Miaule, A., Emuka, C., Poomchongko, N., Ali, S., Rappel, W.-J. and Schroeder, J.I.: Possible impacts of rising CO2 on crop water use efficiency and food security. *California Agriculture*, vol. 72, no. 3, pp. 155–158, 2018.

[156] Daszkowska-Golec, A. and Szarejko, I.: Open or Close the Gate-Stomata Action Under the Control of Phytohormones in Drought Stress Conditions. *Frontiers in Plant Science*, vol. 4, no. May, pp. 1–16, 2013.

[157] Chen, M.Y., Zhuo, G.Y., Chen, K.C., Wu, P.C., Hsieh, T.Y., Liu, T.M. and Chu, S.W.: Multiphoton imaging to identify grana, stroma thylakoid, and starch inside an intact leaf. *BMC Plant Biology*, vol. 14, no. 1, 2014.

[158] Cerovic, Z.G., Ounis, A., Cartelat, A., Latouche, G., Goulas, Y., Meyer, S. and Moya, I.: The use of chlorophyll fluorescence excitation spectra for the non-destructive in situ assessment of UV-absorbing compounds in leaves. *Plant, Cell and Environment*, vol. 25, no. 12, pp. 1663–1676, 2002.

[159] Pedrós, R., Moya, I., Goulas, Y. and Jacquemoud, S.: Chlorophyll fluorescence emission spectrum inside a leaf. *Photochemical and Photobiological Sciences*, vol. 7, no. 4, pp. 498–502, 2008.

[160] Roshchina, V.V.: Vital Autofluorescence: Application to the Study of Plant Living Cells. *International Journal of Spectroscopy*, vol. 2012, pp. 1–14, 2012.

[161] Shen, Y., Zhu, D., Lu, W., Liu, B., Li, Y. and Cao, S.: The characteristics of intrinsic fluorescence of type I collagen influenced by collagenase I. *Applied Sciences (Switzerland)*, vol. 8, no. 10, pp. 1–10, 2018.

[162] Mizuno, D., Konoha-Mizuno, K., Mori, M., Yamazaki, K., Haneda, T., Koyama, H. and Kawahara, M.: An in Vitro System Comprising Immortalized Hypothalamic Neuronal Cells (GT1-7 Cells) for Evaluation of the Neuroendocrine Effects of Essential Oils. *Evidence-based Complementary and Alternative Medicine*, vol. 2015, pp. 1–7, 2015.

[163] Bucevičius, J., Lukinavičius, G. and Gerasimaite, R.: The Use of Hoechst Dyes for DNA Staining and beyond. *Chemosensors*, vol. 6, no. 2, p. 18, 2018.

[164] Genier, E., Bowen, P., Sylvestre, T., Moselund, P.M., Bang, O. and Dudley, J.M.: Amplitude noise and coherence degradation of femtosecond supercontinuum generation in all-normal-dispersion fibers. *J. Opt. Soc. Am. B*, vol. 36, no. 2, pp. A161–A167, 2019.